

Bismuth Nanowire and Antidot Array Studies Motivated by Thermoelectricity

by

Oded Rabin

M.Sc. Chemistry
Weizmann Institute of Science, 1998

B.A. Chemistry
Technion - Israel Institute of Technology, 1996

Submitted to the Department of Chemistry
in partial fulfillment of the requirements for the degree of

Doctor of Philosophy

at the

MASSACHUSETTS INSTITUTE OF TECHNOLOGY

June 2004

© Massachusetts Institute of Technology 2004. All rights reserved.

Author^c.....

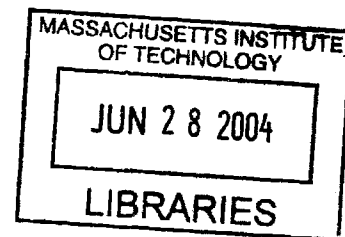
Department of Chemistry
March 18, 2004

Certified by^{ca}.....

Mildred S. Dresselhaus
Institute Professor of Electrical Engineering and Physics
Thesis Supervisor

Accepted by^c.....

Robert W. Field
Chairman, Departmental Committee on Graduate Students



ARCHIVES

This doctoral thesis has been examined by a committee of the Department of Chemistry as follows:

Prof. Sylvia T. Ceyer
Chairman

Prof. Mildred S. Dresselhaus
Thesis Supervisor

Prof. Mounji G. Bawendi
y

Bismuth Nanowire and Antidot Array Studies Motivated by Thermoelectricity

by

Oded Rabin

Submitted to the Department of Chemistry
on March 18, 2004, in partial fulfillment of the
requirements for the degree of
Doctor of Philosophy

Abstract

Porous anodic alumina (PAA) films were utilized to template the fabrication of nanostructures of bismuth, antimony and bismuth-antimony alloys. The cylindrical template pores were used to synthesize nanowires by electrochemical methods. The porous surface of the template was used as a substrate for the e-beam deposition of antidot array thin films. Electrical transport measurements in bismuth nanowire arrays embedded in the templates were demonstrated to be highly sensitive to structural imperfections. Thin film studies compared the weak anti-localization effect in bismuth films with antidot array morphology versus continuous films. It is shown that the antidot array makes the weak anti-localization effect more pronounced in magnetoresistance measurements, and allows for a more detailed study of carrier scattering mechanisms in thin films.

A new process is presented for the fabrication of PAA templates on rigid substrates. The substrate provides mechanical support for the generation of crack-free PAA films over areas of tens of cm^2 , while electrically-conducting substrates can serve as back-electrodes for the electrochemical growth of nanowires and for their electrical characterization. Various processing challenges were solved, including the deposition of thick aluminum films, the control over the adhesion between the layers of the structure, and the removal of the alumina barrier-layer at the interface between the porous film and the substrate. The use of the substrate to achieve non-planar and patterned PAA films is demonstrated.

A model is constructed to calculate the thermoelectric figure-of-merit Z of bismuth-antimony alloy nanowires as a function of diameter, composition, and carrier density. In this model, the band structure of the alloy in bulk form is modified by the quantization of \mathbf{k} -space in the two dimensions perpendicular to the nanowire main-axis. Boltzmann's transport equations are solved with this one-dimensional band structure. The model predicts an enhancement in Z in alloy nanowires compared to the alloys in bulk form and to bismuth nanowires. The enhancement, which was found to be non-monotonic in diameter-composition space, was related to shifts in the populations and energies of the different carrier pockets.

Thesis Supervisor: Mildred S. Dresselhaus
Title: Institute Professor of Electrical Engineering and Physics

Acknowledgments

It is of the nature of scientific research that projects are not carried out single-handedly by an individual researcher, and that new ideas are often a culmination of interactions between individuals within a research society or across disciplines. The work described in this thesis is marked with the influence and participation of many colleagues and friends, whose scientific interest and helping hands made it possible for me to achieve these accomplishments during my graduate studies at M.I.T. These individuals I wish to acknowledge and thank at this opportunity:

My thesis supervisor, Prof. Millic Dresselhaus, whose enthusiasm for science and education is limitless and contagious. I am grateful for the opportunity to take part of the exciting research activities of her group, and explore the previously unfamiliar fields of thermoelectrics and nanotechnology. I have particularly appreciated the freedom I was granted to develop my research plans in various directions. As a result, I was able to acquire a multitude of skills, become familiar with a variety of (seemingly unrelated) topics, and learned to be critical and inventive with respect to my work. I believe this to be one of the greatest advantages of being a graduate student in this group and in this institute. In such a nurturing environment to grow professionally, I can only lament that finances become a restricting factor. I have also learned to appreciate the kind personality of Prof. Dresselhaus in overseeing and addressing students and postdocs, never acting in a derogatory manner despite her status as an internationally renowned scientist and her admirable personal accomplishments, and investing large portions of her time - wherever on the globe she might be - to promote their careers and alleviate the difficulties they face. In many ways, her attitude brings meaning to the term “MGM family”. I am glad to have joined the “MGM family”.

Prof. Gang Chen and Prof. Tayo Akinwande have been very kind in contributing their time, advice, equipment and financial support. Their participation gave a big push to the experimental aspects of this thesis, allowing me to explore directions which were not traditional to the Dresselhaus group. My father Samuel Rabin was amazing in providing equipment and engineering advice from 8850 km away.

Dr. Gene Dresselhaus, our care-taker during the time of Millie's assignment at the Department of Energy and during her travels, has been very constructive in solving daily problems, being critical of our written and oral presentations, and putting smiles on our faces. So was Mrs. Laura Doughty with her infinite attention and concern to our needs inside and outside the laboratory, and in introducing us to her world of music.

Prof. Sylvia Ceyer, the chair of my thesis committee, and Prof. Mounji Bawendi, who dedicatedly followed my progress, and offered their advice in academic, research and mentoring issues.

Dr. Yu-Ming Lin, Paul Herz have made a significant contributions to the execution of the work presented here. Yu-Ming was a remarkable teacher, and taught me most of what I know about the fabrication of anodic alumina and nanowires, thermoelectricity, and electrical characterization. I seem to have failed to come up with a solid-state related question that he could not answer. Paul was the driving force behind the silicon-supported nanoporous templates project. His expertise in microfabrication and the many hours he spent in the clean-room led to the fastest progress and the most beautiful demonstrations we achieved in this project. Thanks to him, I became motivated to get acquainted with microtechnology and nanotechnology forums at M.I.T. Dr. Kornelius Nielsch, Dr. De-Kui Qing and Ramkumar Krishnan have been very helpful in electrochemistry discussions and by sharing samples.

It has been a pleasure to work with the members of the Dresselhaus' research group. The interactions between the group members have always been an example of good spirit and friendship between coworkers. I have received tremendous support from them, and I hope I have made my own contribution to them, as friends and fellow scientists. The Thermoelectrics Subgroup - Dr. Takaaki Koga, Dr. Steve Cronin, Dr. Marcie Black, and Dr. Yu-Ming Lin - has been a greatly inspiring and fun group, which truly combined individuals from very diverse backgrounds into an inventive team. Dr. Sandra Brown, Dr. Alexandra Marucci, Dr. Paula Corio, Dr. Hao Xin, Dr. Ado Jorio, Dr. Noriko Yoshizawa, Dr. Antonio Souza Filho, Grace Chou, Georgii Samsonidze, and in particular my office-mates Dr. Herb Zeiger, Dr.

Ruowen Fu and Ming Tang - each illuminated my period in the group in his special way. I have great respect to Yu-Ming and Georgii who worked additional shifts as system administrators.

Several thermoelectrics-aficionados have collaborated in this work and provided insightful advice: The thermoelectrics group at the Jet Propulsion Labs, the Stacey group at U.C. Berkeley, Prof. Elena Rogacheva, Prof. Riichiro Saito, Dr. Joseph Heremans, Prof. Salah Aeiyaeh, Dr. Jagadeesh Moodera, Prof. J.-P. Issi, and the Chen group at M.I.T. (in particular, Diana Borca-Tasciuc, Chris Dames and Dr. De-Kui Qing).

Special thanks goes to the staff of the Center of Material Science and Engineering, which provide me with a great environment and a multitude of tools for carrying out my research. Dr. Fang-Cheng Chou, Mr. Tim McClure and Mr. Mike Frongillo were formidable in the assistance they provided. Kurt Broderick from the Microsystems Technology Laboratories was very helpful while working in the clean room.

My eclectic Physical Chemistry class, quantum@mit, was a source of many joyful times and many interesting debates. Ricardo Rajsbaum and I shared many “serious conversions” of incomparable importance. Nicolas Aplin-court and Anna Leos-Urbel were, in addition, extremely supportive during the hardships of my initial period in the U.S.

My parents have been extremely supportive throughout, and endured unrepentantly the hardships of living apart for their son for such a long period of time. The attention and guidance they have provided for my personal growth are invaluable. My successes are their achievements.

Contents

1	Introduction	25
1.1	Nanoscience	25
1.2	Templated Synthesis of Nanostructures	26
1.3	Thermoelectric Phenomena	28
1.4	Thesis Outline	32
2	Theoretical Modeling of the Thermoelectric Properties of Bismuth-Antimony Nanowires	35
2.1	Introduction	35
2.2	The Crystal Structure and the Electronic Band Structure of Bismuth-Antimony Alloys	38
2.3	Solution of the Schrödinger Equation for a $\text{Bi}_{1-x}\text{Sb}_x$ Nanowire: Infinite Cylindrical Well Boundary Conditions and Anisotropic Mass Tensors	42
2.4	Modeling the One-Dimensional Dispersion Relation of $\text{Bi}_{1-x}\text{Sb}_x$ Alloy Nanowires	46
2.5	The Electronic Phase Diagram of $\text{Bi}_{1-x}\text{Sb}_x$ Alloy Nanowires	51
2.6	The Calculated Thermoelectric Properties of $\text{Bi}_{1-x}\text{Sb}_x$ Nanowires	56
2.7	Limitations of the Model	63
2.8	Experimental Verification of the Model	65
2.9	Summary	66
3	Modified Porous Anodic Alumina Templates	67
3.1	Background	67

3.1.1	The Structure of Porous Anodic Alumina	68
3.1.2	The Preparation of Porous Anodic Alumina Templates	69
3.2	Motivation	72
3.3	Growth of Porous Anodic Alumina Templates on Rigid Substrates from Evaporated Aluminum Films	73
3.3.1	Influence of Aluminum Evaporation Methods, Annealing, and Polishing on Porous Anodic Alumina Formation on Silicon Wafers	74
3.3.2	The Anodization Process on a Silicon Substrate	80
3.3.3	Growth of PAA Films on an Optically Transparent Substrate	86
3.4	The Effect of Thin Film Coatings on the Growth of Silicon Wafer- Supported Porous Anodic Alumina Films	86
3.4.1	Anodization Time–Current Transients	88
3.4.2	Adhesion Properties	91
3.4.3	Barrier Layer Morphology	92
3.5	Fabrication of Nanowire Arrays in Silicon Wafer-Supported PAA films: Overcoming the Barrier Layer Challenge	95
3.6	Patterned Porous Anodic Alumina Films	102
3.7	Other Modifications: Porous Anodic Alumina Films on Patterned Alu- minum Supports	104
3.8	Summary and Future Directions	106
4	Bismuth, Antimony, and Bismuth-Antimony Nanowire Arrays: Electrochemical Synthesis, Structural Characterization and Electrical Properties	109
4.1	Background	109
4.2	Electrochemical Deposition in Porous Anodic Alumina Templates – General Comments	111
4.3	Electrochemical Deposition of Bismuth Nanowires in Porous Anodic Alumina Templates	115

4.4	Electrochemical Deposition of Antimony Nanowires in Porous Anodic Alumina Templates	117
4.5	Material Characterization of the Electrochemically-Deposited Nanowire Arrays	120
4.6	Improving the Crystallinity of the Electrochemically-Deposited Bismuth Nanowire Arrays	126
4.7	Electrical Characterization of the Electrodeposited Nanowire Arrays	130
4.8	Summary and Future Work	142
5	Enhancement of Weak Anti-Localization Effects in Nanostructured Bismuth Thin Films	143
5.1	Introduction	143
5.1.1	Weak Localization	143
5.1.2	Weak Anti-Localization	145
5.1.3	Motivation	146
5.2	Sample Fabrication and Structural Characterization	148
5.3	Electrical Characterization	154
5.3.1	Temperature Dependence of the Magnetoresistance of the Films	154
5.3.2	Low-Temperature ($0.45 \leq T \leq 4.2$ K) Magnetoresistance Measurements with the ^3He Setup	159
5.3.3	Low-Temperature ($2 \text{ K} \leq T \leq 30 \text{ K}$) Magnetoresistance Measurements with the MPMS Magnetometer Setup	163
5.4	Weak Anti-Localization and Electron-Electron Interaction Effects in the Conductivity of Bismuth Thin Films	177
5.5	Analysis of the Magnetoconductance	181
5.6	Summary	185

List of Figures

1-1	Scheme of the structural features of a porous anodic alumina film on an aluminum substrate, showing the triangular array of pores on the surface of the oxide and the high aspect-ratio cylindrical channels cutting through the oxide layer.	27
1-2	The structural relationship between the porous anodic alumina template and the antidot array (left) or the nanowires (right) templated by it.	28
1-3	Schematic diagrams for simple cooling and energy conversion devices using thermoelectric materials.	29
1-4	The electronic density-of-states functions $g(E)$ characteristic of bulk (3-D), quantum-well (2-D), quantum-wire (1-D), and quantum-dot (0-D) semiconductors.	31
2-1	Experimental results for the ZT of state-of-the-art thermoelectric materials as a function of temperature of operation.	36
2-2	Ball-and-stick representation of the rhombohedral (A7) crystal structure, and the Cartesian coordinate nomenclature.	39
2-3	The Brillouin zone of the rhombohedral crystal structure. The relevant high symmetry points are marked and the Fermi surfaces are drawn as ellipsoids.	41
2-4	A schematic of the electronic band structure near the Fermi energy in $\text{Bi}_{1-x}\text{Sb}_x$ alloys as a function of composition.	41

2-5	Schematic diagram of a one-dimensional subband structure of a carrier pocket in k-space (a) for a parabolic dispersion relation (constant effective mass), and (b) including non-parabolic effects, such as in the case of the L-point pockets of bismuth.	44
2-6	Calculated density-of-states profile of a bismuth nanowire and bulk bismuth as a function of energy.	50
2-7	Phase diagram of the electronic band structure of $\text{Bi}_{1-x}\text{Sb}_x$ nanowires. The locations of the T-, the L- and the H-points in the Brillouin zone are shown in the inset.	54
2-8	Contour plot of the direct bandgap energy at the L-point of $\text{Bi}_{1-x}\text{Sb}_x$ nanowires as a function of nanowire diameter and composition. Values shown are in <i>meVs</i>	55
2-9	<i>ZT</i> versus Fermi energy position in a Bi and a $\text{Bi}_{0.8}\text{Sb}_{0.2}$ nanowire of diameter of 40 nm.	58
2-10	Contour plot of the optimal <i>ZT</i> values for <i>p</i> -type $\text{Bi}_{1-x}\text{Sb}_x$ nanowires vs. wire diameter and antimony concentration.	59
2-11	Contour plot of the optimal <i>ZT</i> values for <i>n</i> -type $\text{Bi}_{1-x}\text{Sb}_x$ nanowires vs. wire diameter and antimony concentration.	60
2-12	Contour plot of the percentage of holes populating the L-point subbands in optimal <i>ZT</i> -optimized <i>p</i> -type $\text{Bi}_{1-x}\text{Sb}_x$ nanowires vs. wire diameter and antimony concentration.	64
3-1	Schematic representation of the structure of a conventional porous anodic alumina film (vertical cross section and top surface).	69
3-2	SEM image of the top surface of a PAA film with an ideal pore ordering structure (pore diameter = 55 nm; center-to-center pore separation = 100 nm).	70

3-3	Main processing steps in a typical preparation of PAA films on aluminum sheets. The drawings represent the cross section structure of the film at different preparation stages. From top to bottom: Polished Al sheet, PAA film on Al sheet, free-standing PAA film, and through-channel PAA film.	71
3-4	SEM images of anodic films on as-deposited PVD aluminum and thermally evaporated aluminum, showing poor pore ordering and large defects at grain boundaries.	75
3-5	SEM image of the top surface of an as-deposited PVD aluminum film.	75
3-6	SEM image of the top surface of an as-deposited e-beam evaporated aluminum film.	76
3-7	SEM image of the top surface of an as-deposited thermally evaporated aluminum film.	76
3-8	SEM image of the vertical cross section of a PAA film formed by the anodization of an as-deposited 10 micron thick PVD aluminum layer on a silicon substrate.	78
3-9	SEM image of the top surface of a PAA film formed on a thermally evaporated aluminum film that was electrochemically polished before anodization.	79
3-10	Top surface, bottom surface and cross section view of a good quality PAA film formed on a silicon wafer by the thermal evaporation of a thick film of aluminum, electrochemical polishing, and a double anodization process.	81
3-11	SEM image of the inverted barrier layer at the interface between PAA and silicon generated by the complete anodization of the film on the wafer.	83
3-12	Schematic representation of the mechanism of barrier layer inversion at the PAA-silicon interface.	83
3-13	Photograph of a PAA film delaminated from the supporting silicon wafer.	84

3-14	AFM micrographs of the surfaces of a PAA film that detached from the silicon substrate on which it was anodized, and SEM micrographs of the same surfaces.	85
3-15	Comparison between the UV-Vis-Near-IR transmission spectra of a PAA-glass bilayer slide and the transmission spectra of a bare glass slide.	87
3-16	Time-current transients from anodization processes with different interface layers materials.	90
3-17	Cross section SEM images of the barrier layer region from PAA films on different interface layers materials. (I) silicon oxide, (II) titanium, (III) <i>n</i> -type silicon, and (IV) platinum.	93
3-18	(a) Cross section SEM micrograph (back-scattering mode) of bismuth nanowire arrays grown on a Pt-coated silicon wafer. (b) Top view of gold nanowires grown on a Pt-coated silicon substrate after dissolution of the PAA template.	97
3-19	Cross section SEM micrograph of the interface between the PAA film and the titanium/titanium-oxide layer after anodization on a Ti-coated silicon wafer, pore widening, and electrochemical barrier layer removal processes.	99
3-20	Cross section SEM micrograph of a damaged PAA film on a Pt-coated silicon wafer following an anodization and a prolonged electrochemical barrier layer removal process.	100
3-21	Cross section SEM micrograph of bismuth telluride nanowires grown in a barrier layer-depleted PAA template on a Ti-coated wafer.	101
3-22	SEM image of a bismuth-filled PAA film obtained by the pressure injection technique.	101
3-23	Patterned lines of PAA on a Ti-coated, SiO ₂ -patterned wafer.	103
3-24	Schematic representation of the use of conducting and insulating pads on the substrate to electrodeposit nanowire arrays of different compositions on the same PAA template.	104

3-25	Photographs of PAA films on aluminum sheets that were subjected to a selective-area CuCl_2 etch.	106
4-1	General setup for the electroplating of nanowires in PAA films with a detailed drawing of the cross section of the working electrode.	113
4-2	Schematics and photograph of the components of the custom-designed electroplating setup.	114
4-3	Dissolution rate of porous anodic alumina films as a function of pH in HCl and NaOH solutions.	116
4-4	Cyclic voltammograms of bismuth electrolytes.	117
4-5	The bismuth-antimony binary alloy phase diagram.	118
4-6	Cyclic voltammograms of DMSO-based bismuth, antimony, and bismuth-antimony electrolytes.	120
4-7	SEM image (back-scattering imaging mode) of a cross section of a bismuth nanowire-filled PAA template obtained by polishing the sample surface perpendicular to the nanowire growth direction.	121
4-8	SEM images (back-scattering imaging mode) showing cross sections of antimony nanowire-filled and bismuth-antimony alloy nanowire-filled PAA templates obtained by film cleavage.	122
4-9	XRD pattern, TEM image, and electron diffraction patterns from arrays of as-deposited polycrystalline bismuth nanowires.	125
4-10	XRD pattern from bismuth 200-nm diameter nanowire arrays: a) as-deposited polycrystalline nanowires, b) same sample after thermal treatment at 300°C , and c) as-deposited crystallographically-oriented nanowires.	128
4-11	Temperature dependence of the normalized resistance $R(T)/R(300\text{ K})$ for bismuth nanowire arrays of various wire diameters prepared by the vapor deposition method.	132

4-12	Temperature dependence of the normalized resistance $R(T)/R(300\text{ K})$ for bismuth nanowire arrays of various wire diameters prepared by electrochemical deposition.	133
4-13	Temperature dependence of the normalized resistance $R(T)/R(300\text{ K})$ for bismuth nanowire arrays of various wire diameters prepared by electrochemical deposition.	135
4-14	Magnetoresistance of bismuth nanowire arrays of various wire diameters prepared by electrochemical deposition measured at 4 K.	136
4-15	Comparison of the temperature dependence of the normalized resistance $R(T)/R(300\text{ K})$ for electrodeposited bismuth nanowire arrays 200-nm in diameter with different microstructures.	138
4-16	Calculated temperature dependence of the normalized resistance $R(T)/R(300\text{ K})$ for bismuth nanowires varying the contribution of the boundary scattering with fixed extrinsic carrier concentration.	140
4-17	Calculated temperature dependence of the normalized resistance $R(T)/R(300\text{ K})$ for bismuth nanowires with large boundary scattering varying the extrinsic carrier concentration.	141
5-1	Magnetoresistance curves of a thin magnesium film as a function of temperature.	145
5-2	Magnetoresistance curves at various temperatures of a gold-doped thin magnesium film.	146
5-3	Magnetoresistance curves at various temperatures of a 6-nm thick gold film grown on glass.	147
5-4	SEM image of the bismuth-coated glass slide. The inset shows a low-magnification image of the polycrystalline bismuth film.	150
5-5	SEM image of the bismuth-coated Whatman filter. The inset shows a low-magnification image of the polycrystalline bismuth film.	150

5-6	SEM image of the bismuth-coated silicon wafer patterned with an array of inverted pyramids. The inset shows the surface before the evaporation of bismuth.	151
5-7	SEM image of the bismuth-coated barrier-layer surface of a Whatman filter. The inset shows a low-magnification image of the polycrystalline film.	151
5-8	Schematic representation of the morphology of a polycrystalline continuous film and a polycrystalline antidot array film.	152
5-9	Diffraction patterns from 33-nm thick bismuth thin films deposited on a glass cover slide, a Whatman filter (porous anodic alumina), and a silicon wafer patterned with an array of inverted pyramids.	153
5-10	Temperature dependence of the resistance, normalized to the resistance at 30 K, of 33-nm thick bismuth films on various substrates.	155
5-11	Temperature dependence of the resistance of a 6-nm thick continuous gold film on a glass substrate ($2\text{ K} < T < 30\text{ K}$). The inset shows data for temperatures up to 270 K.	156
5-12	Temperature dependence of the resistance, normalized to the resistance at 30 K, of a 33-nm thick bismuth film on a Whatman filter, at various magnetic field strengths.	157
5-13	Temperature dependence of the resistance, normalized to the resistance at 30 K, of a 33-nm thick bismuth film on a glass cover slide, at various magnetic field strengths.	158
5-14	Transverse magnetoresistance of a 33-nm thick antidot array bismuth film on a Whatman filter substrate at various operating temperatures.	160
5-15	Transverse magnetoresistance of a 33-nm thick continuous bismuth film on a glass substrate at two operating temperatures. The vertical dashed line corresponds to the field strength at which the magnetic length is equal to the nominal film thickness. The inset is a magnification of the low-field region.	161

5-16	Longitudinal magnetoresistance and transverse magnetoresistance of a 33-nm thick continuous bismuth film on a glass substrate.	163
5-17	Transverse magnetoresistance of a 33-nm thick antidot array bismuth film on a Whatman filter substrate at various operating temperatures.	164
5-18	Transverse magnetoresistance of a 33-nm thick antidot array bismuth film on a silicon substrate at various operating temperatures.	165
5-19	Transverse magnetoresistance of a 33-nm thick continuous bismuth film on a glass substrate at various operating temperatures.	166
5-20	Log-log plot of the temperature dependence of the fitted scattering field values H_i , H_0 , and H_{so} and of the value of fitting parameter A for the magnetoresistance data from a Whatman supported antidot array thin bismuth film. The dashed line is the best fit of the temperature dependence of the values for H_i to a power law T^p	169
5-21	Log-log plot of the temperature dependence of the fitted scattering field values H_i , H_0 , and H_{so} and of the value of fitting parameter A for the magnetoresistance data from an antidot array thin bismuth film on a patterned silicon substrate. The dashed lines are fits of the temperature dependence of the values for H_i to a power law T^p	170
5-22	Log-log plot of the temperature dependence of the fitted scattering field values H_i , H_0 , and H_{so} and of the value of fitting parameter A for the magnetoresistance data from a glass supported continuous thin bismuth film. The dashed line is the best fit of the temperature dependence of the values for H_i to a power law T^p	171
5-23	Temperature dependence of the sheet conductivity, normalized to the sheet conductivity at 30 K, of 33-nm thick bismuth films on various substrates.	178
5-24	Temperature dependence of the sheet conductivity of a 33-nm thick bismuth film on a Whatman filter, at various magnetic field strengths.	179
5-25	Temperature dependence of the sheet conductivity of a 33-nm thick bismuth film on a glass cover slide, at various magnetic field strengths.	180

5-26	Field dependence of the sheet conductivity of 33-nm thick bismuth films on various substrates, at various operating temperatures between 2–30 K.	183
5-27	Sheet conductivity changes (with respect to the zero-field conductivity) as a function of magnetic field of 33-nm thick bismuth films on various substrates, at various operating temperatures between 2–30 K, zooming in the low field region, where the conductivity is dominated by weak anti-localization effects.	184

List of Tables

2.1	Crystal parameters for the unit cell of bismuth and antimony.	38
2.2	The effective mass tensor components for bulk $\text{Bi}_{1-x}\text{Sb}_x$ alloys at $T \leq 77\text{ K}$	48
5.1	Transport parameters obtained from the analysis of the magnetoresistance measurements of 33-nm bismuth films in terms of the weak anti-localization effect.	176

Chapter 1

Introduction

1.1 Nanoscience

Nanoscience, the study of physical phenomena in objects with nanoscale dimensions, is one of the fastest growing areas of scientific research in recent years. The impetus for the expansion of the field originates from the development of new synthetic methods that produce nanostructures with tight control over their size and composition, and from the development and commercialization of analytical tools for the characterization, imaging, and manipulation of nanostructures.[1]

From an applications standpoint, nanostructures allow for the miniaturization of devices, at times substantially increasing their sensitivity. Thus, nanotechnologies are predicted to transform the IC and data-storage industries, where high densities of data-processing and memory units are sought for. Nanostructures can also be incorporated into other materials in high density to create composites with improved or specially tailored properties. In particular, nanoparticles and carbon nanotubes are routinely added to polymers, coatings, and pastes (even sunscreen!) to modify their electrical, optical, or rheological properties.

From a scientific standpoint, nanostructures show a variety of novel effects. Their characteristic sizes can be smaller than critical lengths, such as the exciton diameter, the de-Broglie wavelength, or the carrier mean free path. This leads to the observation of mesoscopic phenomena, such as size-dependent tuning of physical properties,

quantized behavior, and ballistic transport. Another reason for the modification of material properties in nanostructures is the increase in the surface-to-volume ratio. The high proportion of atoms at the surface can lead to structural rearrangements and to an increased sensitivity to the environment. Nanoscience researchers, therefore, do not merely seek to reduce the size of the system of interest, but are motivated by the differences distinguishing the nature of a microscopic system from that of its corresponding macroscopic counterpart.

1.2 Templated Synthesis of Nanostructures

The synthesis of nanostructures is a challenging area, since reproducible and economical synthetic strategies are necessary. The synthesis of quantum wells (two-dimensional nanostructures) via epitaxial growth on crystal surfaces and the synthesis of quantum dots (zero-dimensional quasi-spherical nanostructures) via ligand-mediated solution crystallization have been established. Synthetic routes to quantum wires (one-dimensional nanostructures) and structures with more elaborate shapes are less developed and less understood. One approach, that has a clear cost advantage, is the use of self-assembly. In self-assembly systems, competing interactions between the system's units lead to their collective arrangement into well-defined, predictable structures. The interaction forces are encoded in the physico-chemical structure of the units. The disadvantage of this approach is that only a few material systems can be manipulated in this way, and each forms only one or a few structural motifs. However, self-assembled structures can be utilized as molds or scaffolds for the synthesis of prescribed nanostructures from many other materials. This process is called "templating".

In this work, porous anodic alumina films were used for the templating of nanostructures. Porous anodic alumina films are formed during the anodic oxidation of aluminum sheets. The pores of these films run as channels of cylindrical cross-section across the thickness of the film. Under controlled conditions, the pores self-assemble into a close-packed triangular array of channels possessing similar diameters and

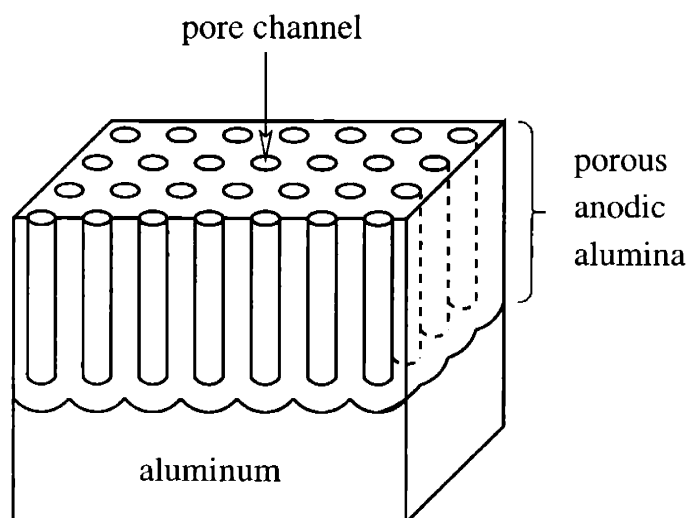


Figure 1-1: Scheme of the structural features of a porous anodic alumina film on an aluminum substrate, showing the triangular array of pores on the surface of the oxide and the high aspect-ratio cylindrical channels cutting through the oxide layer.

lengths. The pore diameters can be globally tuned between 7 and 200 nm, and the channel lengths can be selected in the range of 0.2 to 100 microns. Figure 1-1 shows the structural features of a porous anodic alumina film.

In this thesis, porous anodic alumina films served as templates for nanowire synthesis and for antidot array film preparation. Nanowires were formed by filling the volume of the pores with a continuous block of the material of interest. The nanowire diameters and lengths were identical to the channel diameters and lengths, respectively. Antidot array films were formed by the evaporation of the film material on the porous surface of the porous anodic alumina films. This process resulted in a continuous thin film interspersed with nanopores in a lattice identical to that of the channels in the alumina template. The diameter of the pores of the film was slightly smaller than that of the pores of the template, while the thickness of the film is controlled during the film evaporation. Figure 1-2 relates the structure of the nanowires, and of the antidot array films, to the structure of the porous anodic alumina templates.

The nanostructures formed by templating with porous anodic alumina were used to further elucidate the effect of dimensionality and nanostructuring on material prop-

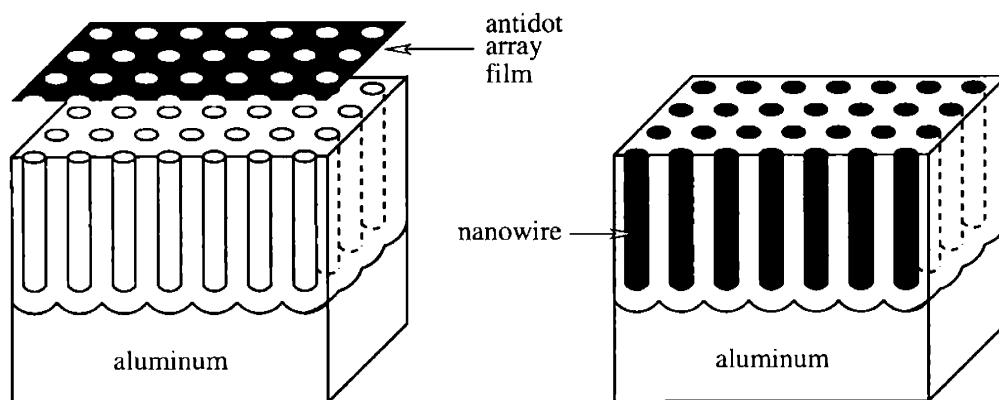


Figure 1-2: The structural relationship between the porous anodic alumina template and the antidot array (left) or the nanowires (right) templated by it.

erties; in particular, on electrical and thermal transport.

1.3 Thermoelectric Phenomena

The thermoelectric phenomena describe coupled electrical and thermal transport through a physical system. In the early nineteenth century, it was shown that an electric potential ΔV is produced by holding a temperature difference ΔT between two junctions of dissimilar materials in an open circuit (the Seebeck effect), and that heat can be absorbed or generated in a junction between two materials at a rate Q , when electrical current I passed through the junction between them (the Peltier effect). The quotients

$$S_{ab} = -\Delta V/\Delta T \quad (1.1)$$

and

$$\pi_{ab} = Q/I \quad (1.2)$$

are characteristic of the material couple (a-b) making the junction, and are called the Seebeck coefficient S_{ab} and the Peltier coefficient π_{ab} , respectively, honoring the discoverers of the above-mentioned thermoelectric phenomena.[2] In the geometries

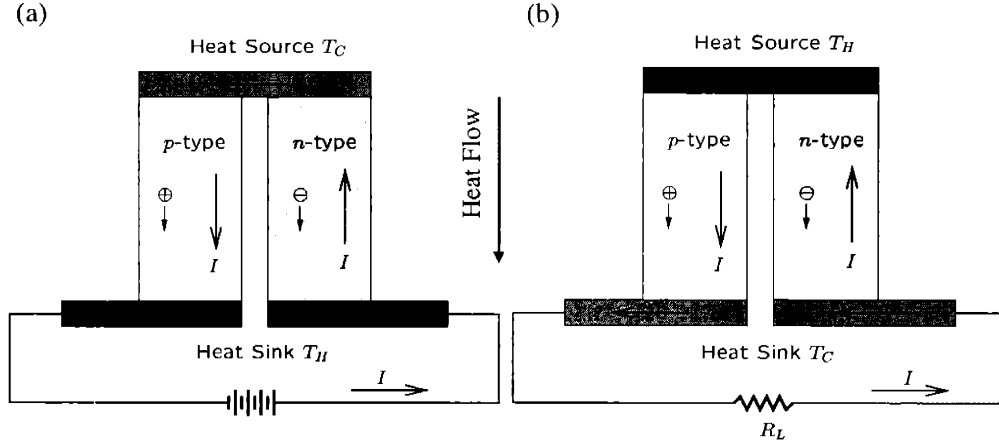


Figure 1-3: Schematic diagrams for simple (a) cooling and (b) energy conversion devices using thermoelectric materials.

shown in Fig. 1-3, these thermoelectric effects can be utilized to generate electrical power from a heat source, or as an electrical solid-state cooling device (thermoelectric refrigeration). Note that the heat flow and the temperature gradient are parallel in the cooling device, and are anti-parallel in the power generator.

The efficiency of a thermoelectric power generator η^{power} and the coefficient-of-performance of a thermoelectric refrigerator Φ^{cool} are defined as

$$\eta^{power} = W/Q \quad \text{and} \quad \Phi^{cool} = Q/W \quad , \quad (1.3)$$

where Q is the rate of heat flow from the heat source, and W is the power obtained from the generator or consumed by the refrigerator. The power consumed by the thermoelectric refrigerator consists of the power dissipated by the resistance of the device (I^2r) and the power used to balance the Seebeck potential due to the temperature difference across the device ($S_{ab} * \Delta T * I$). The power generated by a thermoelectric power generator consists of the power associated with the Seebeck voltage alone. The heat flow from the heat source

$$Q = S_{ab} * T_{source} * I - \frac{1}{2}I^2r \pm \kappa * \Delta T \quad (1.4)$$

comprises of the Peltier heat flow, the heat flow due to half of the power dissipated by Joule heating, and the heat flow due to the thermal conductivity and the temperature

gradient across the device (positive sign for the power generator and negative for the cooling device). By optimizing the geometry of the device, the current, and the external load[3, 4], the performance quotients of Eq. 1.3 are found to reach a maximum of

$$\eta_{max}^{power} = \left\{ \frac{T_M (\sqrt{1 + \mathbf{Z}T_M} + 1)}{\Delta T (\sqrt{1 + \mathbf{Z}T_M} - 1)} + \frac{1}{2} \right\}^{-1} \quad (1.5)$$

and

$$\Phi_{max}^{cool} = \frac{T_M (\sqrt{1 + \mathbf{Z}T_M} - 1)}{\Delta T (\sqrt{1 + \mathbf{Z}T_M} + 1)} - \frac{1}{2} \quad , \quad (1.6)$$

where ΔT is the temperature difference between the hot-end junction and the cold-end junction $T_H - T_C$, and T_M is the average temperature $(T_H + T_C)/2$. Here \mathbf{Z} is defined as

$$\mathbf{Z} = \frac{S_{ab}^2}{\{\sqrt{\kappa_a \rho_a} + \sqrt{\kappa_b \rho_b}\}^2} \quad . \quad (1.7)$$

In the above equation, S_{ab} is the Seebeck coefficient of the couple, κ_i is the thermal conductivity of material 'i', and ρ_i is the electrical resistivity of material 'i'. By definition, \mathbf{Z} solely depends on the materials properties of the thermoelectric couple. The expressions for the maxima of the performance quotients in Eqs. 1.5–1.6 are monotonically increasing functions in \mathbf{Z} . Thus, \mathbf{Z} is called the thermoelectric figure-of-merit of the device. Often, it is more convenient to refer to the properties of a single material than to the properties of a couple. The thermoelectric figure-of-merit of a single material Z is similarly defined as

$$Z = \frac{S_a^2}{\rho_a \kappa_a} \quad , \quad (1.8)$$

derived from the expression for \mathbf{Z} for a couple consisting of the material of interest and a superconductor as material 'b' ($\rho_{superconductor} = 0 \Omega\text{-cm}$, $S_a \equiv S_{ab, b=superconductor}$, also resulting in the relation $S_{xy} = S_x - S_y$). Equations 1.7–1.8 indicate that \mathbf{Z} is the highest for devices with material couples with one junction-component (a.k.a. leg) with $S_a > 0$ (a p -type leg) and another junction-component with $S_b < 0$ (an n -type leg), as suggested in Fig. 1-3. The expressions also indicate that good thermoelectric

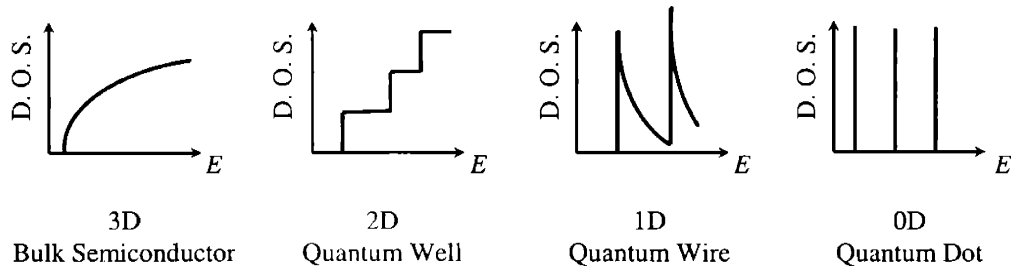


Figure 1-4: The electronic density-of-states functions $g(E)$ characteristic of bulk (3-D), quantum-well (2-D), quantum-wire (1-D), and quantum-dot (0-D) semiconductors.

materials have large $|S|$, low ρ , and low κ . In conventional macroscopic material systems, however, a decrease in ρ (for example, by doping a semiconductor) is accompanied by an increase in κ and a decrease in $|S|$. Thus, only a limited improvement in Z has been achieved by traditional materials optimization.[5]

Nanostructured materials hold, in some cases, a promise for improving the value of Z compared to macroscopic, homogeneous materials. In nanostructured materials, the electronic energy is modified (the representative evolution of the electronic density-of-states with dimensionality is shown in Fig. 1-4), leading to quantum size effects in the electrical (and optical) properties. Heat transport is also modified by the heterogeneous nature of nanostructured materials. Nanoscale engineering can, thus, provide an approach for circumventing the limiting relations between ρ , S , and κ , and provide additional control parameters (i.e. size, dimensionality, geometry) to optimize the thermoelectric properties of a structure. These ideas[6] prompted theoretical and experimental efforts, which have begun to yield positive results in the form of high Z values for semiconductor superlattices and other nanostructured systems.[7–9]

1.4 Thesis Outline

Previous work[10–14], both theoretical and experimental, has brought bismuth nanowires to the center-stage of nanoscale thermoelectrics research. Bismuth nanowires were shown to display interesting phenomena, such as a diameter-induced semimetal-to-semiconductor transition[15] and negative longitudinal magnetoresistance[15]. As nanostructures with large quantum confinement but with a continuous path for transport of charge carriers, bismuth nanowires are also predicted to have high Z values.[16] Further improvements in the modeling, the material science, and the synthesis of nanowires are still necessary for the development of good thermoelectric nanowires. Some of these aspects are addressed in this thesis.

In chapter 2, a theoretical model for the calculation of the thermoelectric properties of bismuth-antimony (Bi-Sb) alloy nanowires is developed and implemented. It will be shown that Bi-Sb alloys can be more favorable than bismuth as a low-dimensional thermoelectric material, and that composition could be used as an additional parameter to manipulate the electronic band structure of nanowires and to optimize their properties.

In chapter 3, a novel approach for the synthesis of nanowires and nanowire-based devices is presented. The chapter details modifications made to the fabrication of porous anodic alumina films, producing films on rigid substrates, thus obtaining films with superior mechanical properties and more complex structure. The use of the modified films as templates for nanowire growth and device fabrication is demonstrated.

In chapter 4, an electrochemical approach for the synthesis of bismuth, antimony and Bi-Sb alloy nanowire arrays is developed. Conditions for the electrodeposition of single crystal bismuth nanowires in porous anodic alumina are explored. This synthetic route to nanowires complements the previously used pressure-injection and gas-phase impregnation techniques. Comparison is made between the structural and physical properties of the nanowire arrays that were obtained by the different methods. Structural defects are shown to be strongly manifested in the electrical characteristics of the bismuth nanowire arrays.

In chapter 5, the fabrication of antidot array films by templating with porous anodic alumina templates is introduced. The electrical properties of these nanostructured films are investigated and compared to those for continuous films. For the first time, the influence of antidot nanostructures on the magnetoresistance due to the weak anti-localization effect is investigated. A detailed analysis is carried out to obtain the characteristic scattering times of the electrons in the films. From this analysis, the effect of the nanoscale structure is revealed.

At the end of each chapter, a summary is provided, along with a brief discussion of remaining unresolved questions relevant to the work that was presented in that chapter.

Chapter 2

Theoretical Modeling of the Thermoelectric Properties of Bismuth-Antimony Nanowires

2.1 Introduction

The thermoelectric figure of merit of a material, Z , is given by the product of the electrical conductivity σ , the square of the Seebeck coefficient S and the inverse of the thermal conductivity κ (Eq. 2.1).[3, 17] Each of these quantities is a complex function of electronic and material properties, such as doping density, density of states, scattering time constants, heat capacity, etc. Since there is a large number of control parameters, the parameter-space is too large to explore experimentally, and even then, only very crude empirical relations could be extracted by trial-and-error explorations. Thus, it is imperative to develop robust models, that will guide experimental efforts by predicting the range in the parameter-space which would lead to the best thermoelectric performance of the material. Such models can also provide informative numerical solutions for the dependence of Z on the various parameters. In addition, it is beneficial to develop a model that will be adaptable to various material systems and that will consider all the significant physical phenomena related to the quantities

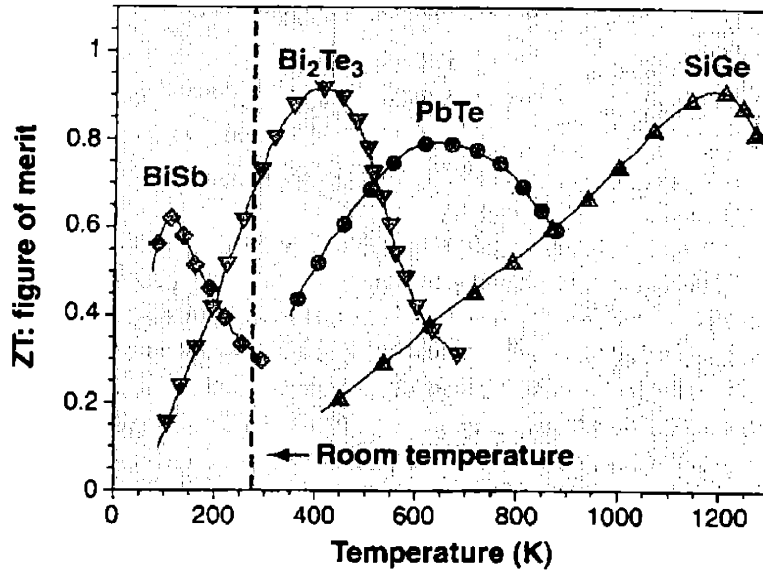


Figure 2-1: Experimental results for the ZT of state-of-the-art thermoelectric materials as a function of temperature of operation.[18]

to be modeled. Yet, at the same time, the model should be simple enough to provide insightful results and relationships (and not merely lists of numbers) and should have a low computational cost. For example, models for Z in 3-dimensional semiconductors have been established, providing guidelines for the fabrication of efficient bulk thermoelectric (TE) materials.[17]

$$Z = \frac{S^2 \sigma}{\kappa}, \quad ZT = Z * T \quad . \quad (2.1)$$

This chapter presents the model developed to calculate the dimensionless thermoelectric figure of merit, $ZT = Z * T$, of isolated nanowires of cylindrical shape. The model is based on the effective mass approximation[19], which simplifies the calculations by considering only the electronic states in the Brillouin zone near the conduction- and valence-band extrema (a.k.a. the electron and hole pockets). In semiconductors and semimetals, these states dominate the transport. The exact details of the electronic dispersion relation $E(\mathbf{k})$ are ignored, and a parabolic band structure is assumed near the energy minima/maxima. This allows us to describe the

carrier pocket by only one quantity: the carrier effective mass tensor.

The model is demonstrated here in relation to the calculation of the ZT of $\text{Bi}_{1-x}\text{Sb}_x$ nanowires. As shown in Fig.2-1[18], Bi-Sb alloys are of particular interest for thermoelectricity in the 70–100 K temperature range, where bulk Bi-Sb alloys are the material of choice due to their relatively high $ZT \approx 0.5$. The figure also indicates one of the limitations in using bulk TE materials: For several decades, the highest ZT values obtained experimentally have an upper bound of $ZT \sim 1$. Further increase of ZT is limited by constraining physical relations between σ , S , and κ , such as the Wiedemann-Franz law.[20, 21] Low-dimensional structures, in which the constraining relations between σ , S and κ are altered, can offer a way to improve the ZT compared to bulk materials. Thus, it is of practical interest to model the transport properties of $\text{Bi}_{1-x}\text{Sb}_x$ nanowires and to determine whether they will be advantageous for thermoelectric applications.

The calculations involve the following steps, which will be described in detail in this chapter:

1. The wire diameter, the alloy composition, and the temperature of the investigation are chosen. The wire longitudinal axis orientation is defined in terms of the crystallographic axes of the Bi-Sb alloy system.
2. The electron- and hole-pocket mass tensors are determined from bulk values.
3. For each carrier pocket, a two-dimensional Schrödinger equation is constructed and numerically solved to obtain a set of eigen-energies, corresponding to the subband edge energies.
4. The carrier density is chosen.
5. The electrical conductivity (σ), the Seebeck coefficient (S) and the electronic-contribution to the thermal conductivity are calculated based on the expressions derived from the Boltzmann transport equations, considering the collective contribution of the subbands.

Table 2.1: Crystal parameters for the unit cell of bismuth and antimony.

	rhombohedral cell[24]		hexagonal cell[25]	
	t (Å)	α	a (Å)	c (Å)
antimony	4.5066	57°6'	4.307	11.273
bismuth	4.7459	57°14'	4.547	11.8616

6. The lattice contribution to the thermal conductivity is estimated, considering the bulk thermal conductivity and diameter-dependent surface-scattering.
7. The Z is calculated in accordance with equation 2.1, and $ZT = Z * T$.

These steps can be repeated to obtain the dependence of ZT on composition, crystallographic orientation, temperature, and carrier concentration, and eventually the conditions are optimized to maximize ZT .

2.2 The Crystal Structure and the Electronic Band Structure of Bismuth-Antimony Alloys

Bismuth, antimony, and their alloys crystallize in rhombohedral structures (space group $R\bar{3}m$)[22] with two atoms per unit cell, as shown in Fig. 2-2. This structure can be described also as two inter-penetrating fcc sub-lattices displaced from each other along the trigonal axis, and distorted by stretching along the same axis. The unit cell dimensions are given in table 2.1. The structure defines a Cartesian coordinate system, with the z -axis along the C_3 symmetry axis (the trigonal axis), the x -axis along one of the C_2 axes (the binary axis), and the y -axis perpendicular to the previous two (the bisectrix axis). Due to the 3-fold symmetry of the distortion axis, it is also common to describe the crystal as a hexagonal lattice, with c along the trigonal axis, and a along the binary axes.

The lattice parameters of the $\text{Bi}_{1-x}\text{Sb}_x$ alloys change monotonically with composition[26, 27]. However, in terms of the hexagonal cell, only a changes linearly with

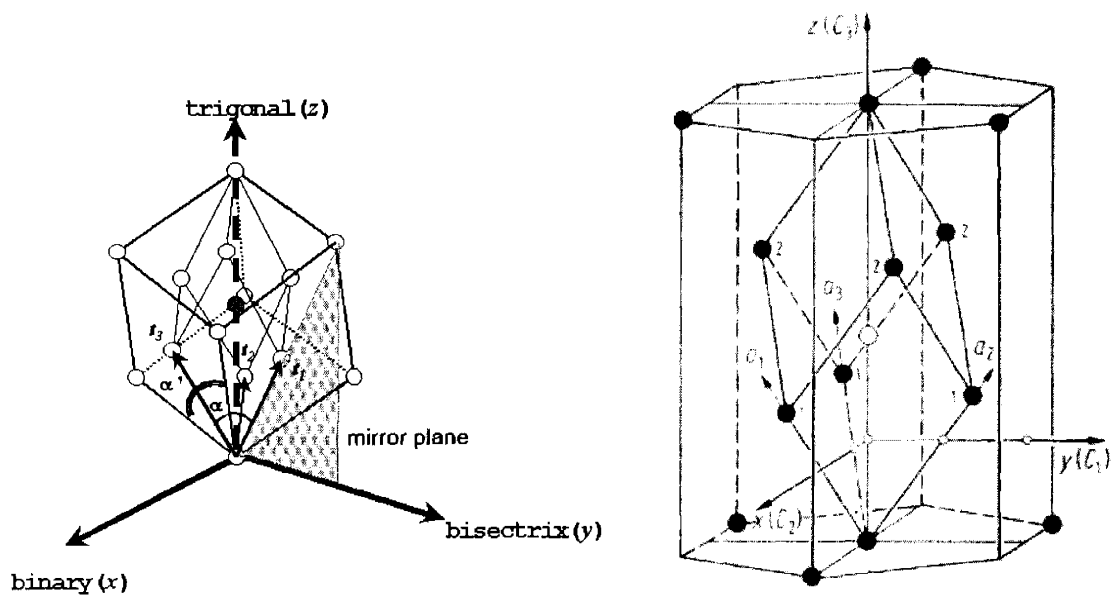


Figure 2-2: Ball-and-stick representation of the rhombohedral (A7) crystal structure, and the Cartesian coordinate nomenclature. Left: The rhombohedral unit cell, with the unit cell vectors denoted as (t_1, t_2, t_3) , in the context of the fcc lattice representation. Right: The rhombohedral unit cell, with the unit cell vectors denoted as (a_1, a_2, a_3) , in the context of the hexagonal representation.[23]

composition (Vegard's law), while the change of c deviates from the Vegard's law prediction.

The Brillouin zone of Bi-Sb alloys is depicted in Fig. 2-3. As a result of the trigonal distortion (stretch) of the unit cell in real space, the Brillouin zone in crystal momentum space is compressed along k_z , removing the 4-fold degeneracy of the L-point, and generating an energy splitting between the T-point (located at the intersection between the Brillouin zone edge and the k_z axis) and the 3 degenerate L-points (at the center of the other hexagonal faces of the Brillouin zone).[28] In the $\text{Bi}_{1-x}\text{Sb}_x$ alloy system, the conduction band extrema (a.k.a. the electron pockets) are at the L-points, while the valence band extrema (a.k.a. the hole pockets) can be located at the L-points, the T-point, the H-points, or several of the above, depending on the alloy composition.[27, 29] Fig. 2-4 illustrates how the composition of the $\text{Bi}_{1-x}\text{Sb}_x$ alloy affects the band structure[30]: For $0 \leq x \leq 0.07$ there is an energy overlap between the T-point valence band pocket and the conduction band, and the material is a semimetal resembling pure Bi. For $x \geq 0.22$ there is an overlap between the H-point valence band pockets and the conduction band, and the material is a semimetal resembling pure Sb. In the interesting composition range $0.07 \leq x \leq 0.22$, there is an energy gap between the conduction band extrema and the valence band extrema (which shift locations with composition) and the material is a narrow-gap semiconductor.

Numerous experiments were carried out to map the energy gap or the energy overlap of $\text{Bi}_{1-x}\text{Sb}_x$ alloys, mostly in the Bi-rich regime.[27, 29, 30, 34–40] A compilation of these data led us to propose the following empirical relations between the composition (x) and the relative energies of the L-, T- and H-point extrema:

$$E_{T,h}(x) = 45.5 - 551.6 * x \quad (2.2)$$

$$E_{H,h}(x) = -101.36 + 525.8 * x \quad (2.3)$$

$$E_{L,e}(x) = \begin{cases} |484.4 * (x - 0.042)^2 - 155.75 * (x - 0.042)| & (x \leq 0.17) \\ 12.0 + 45.8 * x & (x \geq 0.17) \end{cases} \quad (2.4)$$

$$E_{L,h}(x) = -E_{L,e}(x) \quad , \quad (2.5)$$

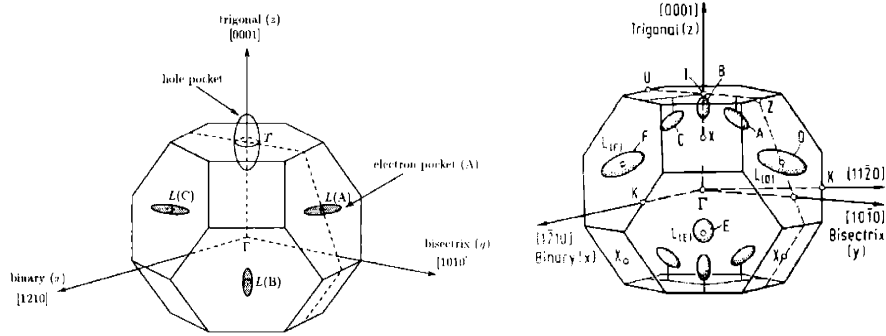


Figure 2-3: The Brillouin zone of the rhombohedral crystal structure. The relevant high symmetry points are marked and the Fermi surfaces are drawn as ellipsoids. The zone at the left depicts the L -point electron pockets and the T -point hole pocket in bulk bismuth.[31, 32] The zone at the right depicts the L -point electron pockets (marked D-F) and the H -point pockets (marked A-C and unmarked) in bulk antimony.[33]

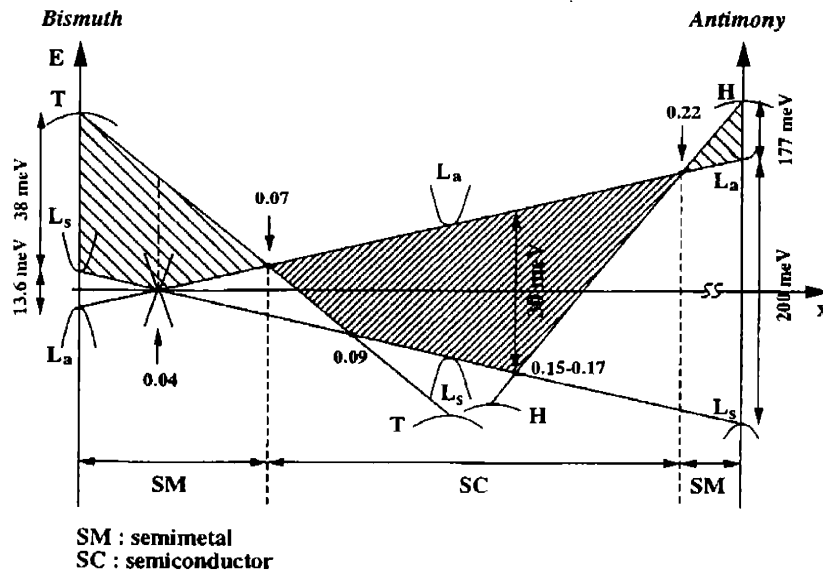


Figure 2-4: A schematic of the electronic band structure near the Fermi energy in $\text{Bi}_{1-x}\text{Sb}_x$ alloys as a function of composition.[30]

where the energies are given with respect to the L-point mid-gap energy, and the subscripts (h) and (e) correspond to hole and electron pockets, respectively.

Bismuth-antimony alloys have been studied extensively as potential thermoelectric materials, since relatively large ZT values can be obtained in the 70–100 K temperature range[39, 41], as shown in Fig. 2-1. Improvement on these results could be achieved by the fabrication of nanostructures out of these materials. It has been proposed that the ZT of thin films and nanowires can reach higher values than that of macroscopic samples of the same material, due to the modification of the carrier density-of-states profile and the enhancement of surface effects in one- or two-dimensional systems.[10, 42] In particular, enhancement in ZT was predicted in bismuth nanowires, due to the additional effect of a quantum-confinement induced semimetal-to-semiconductor transition.[16, 43] Since the ZT in bulk bismuth samples can be improved by alloying with antimony, and the bismuth-antimony alloy system has a very rich and more interesting electronic band-structure (see Fig. 2-4), it is of great interest to study the effect of quantum confinement in nanowire systems of bismuth-antimony alloys, and to understand the effect of the nanowire diameter and composition on its transport properties.

In the next two sections, a method for modeling the changes in the band structure of $\text{Bi}_{1-x}\text{Sb}_x$ alloys as a result of quantum confinement, imposed by the nanowire structure, will be developed.

2.3 Solution of the Schrödinger Equation for a $\text{Bi}_{1-x}\text{Sb}_x$ Nanowire: Infinite Cylindrical Well Boundary Conditions and Anisotropic Mass Tensors

For illustration purposes, a simplified version of the problem will be presented first. Consider a particle confined in a cylindrical volume by a potential of the form:

$$V(r, \theta, z) = \begin{cases} 0 & (r \leq r_0) \\ \infty & (r > r_0) \end{cases} . \quad (2.6)$$

Since the wavefunction of the particle is restricted in directions normal to the cylinder axis by the boundary condition

$$\Psi(r > r_0, \phi, z) = 0 \quad , \quad (2.7)$$

the confinement causes the energies associated with the transverse motion of the particle to be quantized, and the lowest energy level is approximated by

$$\Delta E = \varepsilon_{00} \approx \frac{\pi^2 \hbar^2}{m_t^* r_0^2} \quad , \quad (2.8)$$

where m_t^* is the transverse effective mass of the particle. Since the potential is uniform along the wire axis, the particle motion is free along the longitudinal direction and will be characterized by a one-dimensional dispersion relation

$$E_{nm}(k_l) = \varepsilon_{nm} + \frac{\hbar^2 k_l^2}{2m_l^*} \quad , \quad (2.9)$$

where ε_{nm} represents the quantized (transverse) energy labeled by two quantum numbers (n, m) , while k_l is the wavenumber of the particle wavefunction traveling along the wire axis, and m_l^* is the longitudinal effective mass of the particle. Thus, this simple model shows that a two-dimensional confinement of the wavefunction of a particle results in the formation of one-dimensional subbands in k -space (see Fig. 2-5). The energy displacement of each subband, $E_{nm}(0) = \varepsilon_{nm}$, is a manifestation of the quantization of the transverse motion, and therefore a function of the transverse effective mass and the cross-section geometry of the confining volume. The k_l -dependence of each subband is a function of the effective mass along the non-confined dimension.

In the case of $\text{Bi}_{1-x}\text{Sb}_x$ nanowires, the particle is replaced by an electron wavepacket in the nanowire, and the potential V is replaced by the potential of the lattice and the other electrons, which is periodic within the nanowire and infinite outside of the nanowire (i.e. the insulating environment). The effective mass theorem[19] can be used to simplify the treatment of the real system into a tractable problem, similar

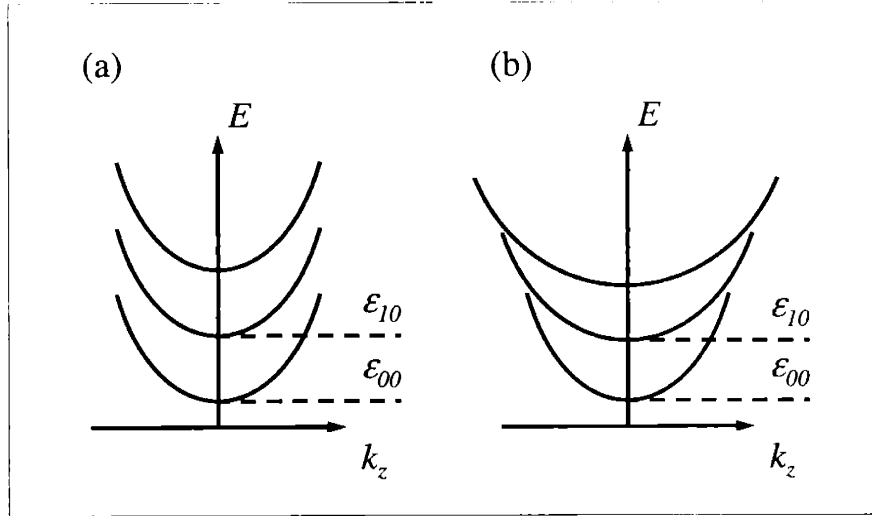


Figure 2-5: Schematic diagram of a one-dimensional subband structure of a carrier pocket in k -space (a) for a parabolic dispersion relation (constant effective mass), and (b) including non-parabolic effects, such as in the case of the L-point pockets of bismuth (see Sect. 2.4). ϵ_{00} and ϵ_{10} denote the two lowest transverse quantization energies.

to the one mentioned above: Given the band structure of the material of interest, the dispersion relation near energy extremum points in the Brillouin zone (carrier pockets) can be expanded as

$$E(\mathbf{k}) = E_0 + \frac{\hbar^2}{2} (\mathbf{k} - \mathbf{k}_0) \cdot \boldsymbol{\alpha}_0 \cdot (\mathbf{k} - \mathbf{k}_0) \quad , \quad (2.10)$$

where $\hbar\mathbf{k}_0$ and E_0 are the band edge crystal-momentum and energy, respectively, and $\boldsymbol{\alpha}_0$ is the inverse of the effective mass tensor, \mathbf{M} ,

$$\boldsymbol{\alpha}_0^{-1} = \mathbf{M} \equiv \begin{pmatrix} m_{11} & m_{12} & m_{13} \\ m_{21} & m_{22} & m_{23} \\ m_{31} & m_{32} & m_{33} \end{pmatrix} \quad . \quad (2.11)$$

The subscripts of the tensor components (1,2,3) correspond to the Cartesian axes of the rhombohedral $\text{Bi}_{1-x}\text{Sb}_x$ crystal (x, y, z) as described in Sect. 2.2, or to the Cartesian coordinate system associated with the nanowire transverse (x', y') and longitudinal (z') dimensions. When the distinction between the coordinate systems is important, it will be clearly stated in the text to follow.

The effective mass theorem states that the envelope function of an electron wave-packet centered at k_0 , $\Psi_{k_0}(\mathbf{r})$, observes the Schrödinger equation obtained by replacing \mathbf{k} in Eq. 2.10 with $(k_0 - i\nabla)$,

$$E\Psi_{k_0}(\mathbf{r}) = -\frac{\hbar^2}{2}\nabla \cdot \boldsymbol{\alpha}_0 \cdot \nabla\Psi_{k_0}(\mathbf{r}) \quad , \quad (2.12)$$

with the boundary conditions

$$\Psi_{k_0}(r > \frac{d_W}{2}) = 0 \quad , \quad (2.13)$$

where d_W is the nanowire diameter. For simplicity, I will neglect the subscripts in the following discussion.

The physical interpretation of the effective mass tensor \mathbf{M} (and its inverse $\boldsymbol{\alpha}$) requires it to be symmetric, that is $m_{ij} = m_{ji}$ and $\alpha_{ij} = \alpha_{ji}$. Furthermore, since the nanowire system has cylindrical symmetry, all the physical quantities are invariant under rotation about the wire axis z' . Therefore, using the nanowire coordinate system, with an appropriate rotation about the z' axis, we can always make the matrix elements $\alpha_{12} = \alpha_{21} = 0$. Physically, the effect of this particular rotation is equivalent to choosing a proper set of x' and y' axes so that the ellipse, obtained by projecting Fermi surface ellipsoid onto the x' - y' plane, will have its major axis parallel to the x' or y' axes. With $\alpha_{12} = \alpha_{21} = 0$, the Schrödinger equation can be rewritten as

$$-\frac{\hbar^2}{2} \left(\alpha_{11} \frac{\partial^2 \Psi}{\partial x'^2} + \alpha_{22} \frac{\partial^2 \Psi}{\partial y'^2} + 2\alpha_{13} \frac{\partial^2 \Psi}{\partial x' \partial z'} + 2\alpha_{23} \frac{\partial^2 \Psi}{\partial y' \partial z'} + \alpha_{33} \frac{\partial^2 \Psi}{\partial z'^2} \right) = E\Psi \quad . \quad (2.14)$$

A solution of Eq. 2.14 has the general form:

$$\Psi = u(x', y') \exp(ik_{x'}x') \exp(ik_{y'}y') \cdot \exp(ik_{z'}z') \quad . \quad (2.15)$$

Substituting Eq. (2.15) into Eq. (2.14), we can decouple the terms involving derivatives of $u(x', y')$ from terms containing $k_{z'}$ by setting

$$k_{x'} = -(\alpha_{13}/\alpha_{11})k_{z'} \quad \text{and} \quad k_{y'} = -(\alpha_{23}/\alpha_{11})k_{z'} \quad , \quad (2.16)$$

which simplifies Eq. 2.14 into a second-order differential equation in two variables

$$-\frac{\hbar^2}{2} \left(\alpha_{11} \frac{\partial^2}{\partial x'^2} + \alpha_{22} \frac{\partial^2}{\partial y'^2} \right) u = \left[E - \frac{\hbar^2 k_{z'}^2}{2} \left(\alpha_{33} - \frac{\alpha_{23}}{\alpha_{22}} - \frac{\alpha_{13}}{\alpha_{11}} \right) \right] u \quad . \quad (2.17)$$

The expression in parenthesis on the right hand side of the equation is equal to $(m_{33})^{-1}$, as can be shown from the relation $\boldsymbol{\alpha} = \mathbf{M}^{-1}$.

The above formalism leads to the conclusion that the dispersion relation of electron wavepackets in a cylindrical nanowire can be expressed as:

$$E(\mathbf{k}) \equiv E_{nm}(k_{z'}) = \varepsilon_{nm} + \frac{\hbar^2 k_{z'}^2}{2m_{33}} \quad , \quad (2.18)$$

(Eq. 2.18 being the equivalent of Eq. 2.9 in the simplified model shown earlier) where ε_{nm} are the eigen-values of the eigen-value problem

$$-\frac{\hbar^2}{2} \left(\alpha_{11} \frac{\partial^2}{\partial x'^2} + \alpha_{22} \frac{\partial^2}{\partial y'^2} \right) u = \varepsilon_{nm} u \quad (2.19)$$

with the boundary condition $u(r > \frac{dw}{2}) = 0$. The electron pocket parameters α_{11} , α_{22} and m_{33} are the components of the effective mass tensor and its inverse **given in the coordinate system of the nanowire (x', y', z') and rotated so that $\alpha_{12}=0$** . The variable $k_{z'}$ is interpreted from Eq. 2.18 as the wavenumber of the traveling wavepacket in the non-confined (longitudinal) direction.

It should be pointed out that the eigen-value problem of Eq. 2.19 can be solved analytically only for the case $\alpha_{11} = \alpha_{22}$, that is for materials with transverse isotropic effective masses. Since bismuth and antimony have very anisotropic Fermi surfaces, for most of the carrier pockets in $\text{Bi}_{1-x}\text{Sb}_x$ alloy nanowires, this condition does not apply. Thus, solutions for the eigen-values ε_{nm} in Eq. 2.19 were obtained using a MATLAB code based on a numerical method developed by Dr. Y.-M. Lin.[13]

2.4 Modeling the One-Dimensional Dispersion Relation of $\text{Bi}_{1-x}\text{Sb}_x$ Alloy Nanowires

In the previous section (Sect. 2.3) we described the formalism to obtain the dispersion relation $E(\mathbf{k})$ of a crystalline material shaped into a nanowire. The formalism utilizes

the known dispersion relation of the carrier pockets in the crystalline material in bulk form. In this section, we will describe the information available for bulk $\text{Bi}_{1-x}\text{Sb}_x$ alloys that is used in the model, and the results obtained for the dispersion relation of $\text{Bi}_{1-x}\text{Sb}_x$ alloy nanowires of various nanowire diameters (d_W) and compositions (described by the antimony mole fraction x).

As mentioned in Sect. 2.2, bismuth and antimony are semimetals in bulk form, while $\text{Bi}_{1-x}\text{Sb}_x$ alloys may be semimetals or semiconductors depending on their composition. This was illustrated in Fig. 2-4, which schematically shows the shift of the energy of the Brillouin zone high-symmetry points as a function of composition, and parametrized in Eqs. 2.2–2.5. In bulk $\text{Bi}_{1-x}\text{Sb}_x$ alloys, the valence-band edges are located at the T-point, the 3-fold degenerate L-point, or the 6-fold degenerate H-point (see Fig. 2-3 for the location of these points in the Brillouin zone) depending on composition, while the conduction band edges are located at the L-points for all compositions. Each band edge gives rise to a carrier pocket with a particular effective-mass tensor. In the nanowire model, each carrier pocket will yield a one-dimensional dispersion relation $E_{nm}(k_{z'})$ representing its splitting into subbands. The total one-dimensional dispersion relation of the $\text{Bi}_{1-x}\text{Sb}_x$ alloy nanowire will be the sum of the individual carrier pocket dispersion relations, shifted in energy with respect to each other by the composition-dependent bulk band edge energies.

The effective mass tensor of the T-, L- and H-point pockets in $\text{Bi}_{1-x}\text{Sb}_x$ alloys are expected to display temperature and composition dependence, since the crystal structure is a function of these two parameters. In the following study, we have focused on the modeling of the nanowire dispersion relations and the nanowire transport properties at 77 K. The motivation for choosing this particular temperature is that the thermoelectric performance of $\text{Bi}_{1-x}\text{Sb}_x$ alloys is optimal in the range 70–100 K, and is the highest among all examined materials in this temperature range.[18] In addition, the electronic band structure of bismuth has a strong temperature dependence above 80 K, but is relatively unchanged in the range 4-80 K, and there is more reliable data available about the band structure of $\text{Bi}_{1-x}\text{Sb}_x$ alloys in this low-temperature range.[44, 45] The composition range studied was in the bismuth-rich regime of $0 \leq$

Table 2.2: The effective mass tensor components for bulk $\text{Bi}_{1-x}\text{Sb}_x$ alloys at $T \leq 77$ K.

Parameters	Notation	Value	Reference
L-point carrier effective mass tensor components at the band edge (bulk bismuth, $x=0$) ^a	m_{xx}	$0.00119 m_0$	[47]
	m_{yy}	$0.263 m_0$	
	m_{zz}	$0.00516 m_0$	
	m_{yz}	$0.0274 m_0$	
T-point hole effective mass tensor components at the band edge	m_{xx}	$0.059 m_0$	[48]
	m_{yy}	$0.059 m_0$	
	m_{zz}	$0.634 m_0$	
H-point hole effective mass tensor components at the band edge	m_{xx}	$0.068 m_0$	[49]
	m_{yy}	$0.63 m_0$	
	m_{zz}	$0.34 m_0$	
	m_{yz}	$0.41 m_0$	

^a For other values of x , the mass tensor is modified to account for the dependence of the non-parabolicity of the band structure at the L-point on the bandgap energy, E_{gL} .

$x \leq 0.3$, again, where the most prominent thermoelectric behavior is observed in the bulk.[39, 46] The effective mass tensors from bulk elemental bismuth[47, 48] were used for the T-point and L-point carrier pockets, and for the H-point hole pockets the parameters from bulk elemental antimony were used.[49] The effect of composition on the effective mass was only introduced through the non-parabolic effects in the L-point dispersion relation (see below). It was found that this model approximated satisfactorily the experimental data of carrier effective masses in the alloys, which are scarcely available in the literature.[36, 38, 50–52] The effective mass tensor elements used in the calculations are given in Table 2.2 in the crystal coordinate system. The mass tensor components that are equal to zero were not included in the table.

At the L-point of the Brillouin zone of bismuth and bismuth-rich $\text{Bi}_{1-x}\text{Sb}_x$ alloys, there is a small direct bandgap between the conduction band and the valence band

($E_{gL} = 13.6$ meV in Bi at 4 K). The strong coupling between the bands results in a non-parabolic dispersion relation around the L-point given by[28]

$$E_L(\mathbf{k}) = \frac{\hbar^2 \mathbf{k}^2}{2m_0} \pm \frac{E_{gL}}{2} \sqrt{1 + \left(\frac{2}{E_{gL}}\right)^2 \frac{\hbar^2}{m_0^2} (\mathbf{k} - \mathbf{k}_L) \cdot \mathbf{p}^2 \cdot (\mathbf{k} - \mathbf{k}_L)} \quad (2.20)$$

for electrons (+ sign) and for holes (− sign), where E_{gL} is the direct bandgap at the L-point, \mathbf{k}_L is the wavevector of the L-point, and \mathbf{p}^2 is a momentum operator coupling term between the L-point wavefunctions $\mathbf{p}^2 = \langle \Psi_{cL} | \mathbf{p} | \Psi_{vL} \rangle \langle \Psi_{vL} | \mathbf{p} | \Psi_{cL} \rangle$. This dispersion relation is derived by the 2-band non-degenerate $\mathbf{k} \cdot \mathbf{p}$ perturbation theory, also known as the 2-band Lax model.[53] While \mathbf{p}^2 is difficult to calculate, we can derive a relation between the band edge inverse effective mass and the direct bandgap from the second derivative of the dispersion relation with respect to $\mathbf{k} - \mathbf{k}_L$:

$$\boldsymbol{\alpha}_{edge} = \frac{2}{\hbar^2} \frac{\partial^2 E_L(\mathbf{k})}{\partial (\mathbf{k} - \mathbf{k}_L)^2} = \frac{1}{m_0} \cdot \mathbf{I} \pm \frac{1}{m_0^2} \frac{2}{E_{gL}} \cdot \mathbf{p}^2 \quad , \quad (2.21)$$

where \mathbf{I} is the identity matrix.

Since the inverse effective mass tensor and the direct bandgap at the L-point of bulk bismuth are known (Table 2.2 and Eq. 2.4-2.5), we can use Eq. 2.21 to derive the inverse effective mass tensor at the L-point of bulk $\text{Bi}_{1-x}\text{Sb}_x$ given the direct bandgap at that composition

$$\boldsymbol{\alpha}_{edge}(\text{Bi}_{1-x}\text{Sb}_x) = \frac{E_{gL}(\text{Bi})}{E_{gL}(\text{Bi}_{1-x}\text{Sb}_x)} \cdot \boldsymbol{\alpha}_{edge}(\text{Bi}) + \frac{1}{m_0} \left(1 - \frac{E_{gL}(\text{Bi})}{E_{gL}(\text{Bi}_{1-x}\text{Sb}_x)}\right) \cdot \mathbf{I} \quad . \quad (2.22)$$

Once the subband edge energies ε_{nm} were calculated according to Eq. 2.19 using the band edge effective mass tensor components from Eq. 2.22, these energies need to be corrected to account for the non-parabolic effect away from the band edge. The correction is performed by finding the $(\mathbf{k} - \mathbf{k}_L)$ value that would correspond to each subband energy in a parabolic potential, and plugging it back into Eq. 2.20 to obtain the potential energy at that point in the non-parabolic potential. This procedure results in corrected subband energies given by

$$\varepsilon_{nm}(\text{non-parabolic}) \approx \frac{E_{gL}}{2} \left(\sqrt{1 + \frac{4\varepsilon_{nm}}{E_{gL}}} - 1 \right) \quad . \quad (2.23)$$

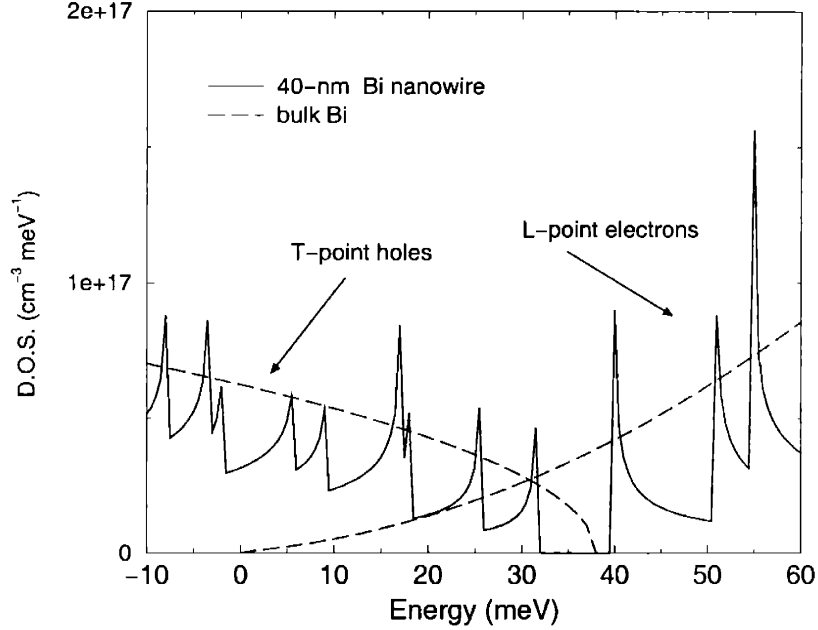


Figure 2-6: Calculated density-of-states profile of a bismuth nanowire (solid line) and bulk bismuth (dashed line) as a function of energy.[13]

The non-parabolic correction to the longitudinal effective mass component of the subband m_{33}^{nm} is calculated by substituting the corrected subband direct gap (the bulk direct bandgap plus twice the corrected quantization energy) for $E_{gL}(Bi_{1-x}Sb_x)$ in Eq. 2.22. The non-parabolicity of the dispersion relation of the subbands will be ignored during the calculation of the transport properties. Therefore, **the subband energy offsets ε_{nm} and the longitudinal effective mass components m_{33}^{nm} are sufficient to describe the nanowire electronic dispersion relation by this model** (Eq. 2.18). The electronic density-of-states can be calculated from the dispersion relation. An example calculation of the density-of-states in a bismuth nanowire and in bulk bismuth is presented in Fig. 2-6. The calculation clearly shows the transition from a slowly varying density-of-states function in bulk ($D.O.S. \approx (E - E_{edge})^{\frac{1}{2}}$), to a function composed of a set of spikes originating from the one-dimensional subbands in the nanowire ($D.O.S. \approx \sum_{i,n,m} (E - E_{n,m}^i)^{-\frac{1}{2}}$).

Note that under the assumptions of the model, the carrier pockets with parabolic

dispersion relations (the T- and H-point hole pockets) give rise to subband sets with a common effective mass value, while carrier pockets with non-parabolic dispersion relations give rise to subband sets in which the effective mass increases with the subband quantization energy ε_{nm} (see Fig. 2-5).

2.5 The Electronic Phase Diagram of $\text{Bi}_{1-x}\text{Sb}_x$ Alloy Nanowires

The model described in the previous section was used to calculate the dispersion relation of the electronic subbands of $\text{Bi}_{1-x}\text{Sb}_x$ nanowires of different wire diameters d_W and alloy compositions (described by the antimony mole fraction x). The calculation dealt with the composition range $0 \leq x \leq 0.30$. This range of $\text{Bi}_{1-x}\text{Sb}_x$ alloy compositions includes the thermoelectrics best bulk $\text{Bi}_{0.85}\text{Sb}_{0.15}$ alloys ($ZT=0.52$ at 80 K), and is the most interesting in terms of the number of carrier pockets involved in determining the transport properties and their relative energies (see Fig. 2-4). The range of wire diameters was chosen as $10 \text{ nm} \leq d_W \leq 100 \text{ nm}$. The upper limit results from the critical diameter for the transition from a one-dimensional system to a three-dimensional system, as the quantization energies become smaller than the thermal energy, and the carrier mean-free path becomes much smaller than the wire diameter. At larger wire diameters, the discretization of the band structure into subbands is not justified. The lower limit of the nanowire diameter is related to changes in the crystal structure of $\text{Bi}_{1-x}\text{Sb}_x$ as the nanowire diameter decreases. The fraction of nanowire atoms found on the nanowire surface has a d_W^{-1} dependence on the nanowire diameter. As we approach the atomic limit of the nanowire diameter, more and more atoms find themselves on the nanowire surface, with a lower number of neighboring atoms compared to atoms in the bulk. Thus, the potential they experience is different from that in the bulk, and a structural rearrangement is expected. In this case, our model is not valid since it is based on the conservation of the bulk crystal and electronic band structure in the nanowires. [In practice, the diameter can be as narrow as two

Bi atoms for bismuth lines self-organized on single crystal silicon surfaces.[54]] The trigonal axis (z) of the crystal structure of $\text{Bi}_{1-x}\text{Sb}_x$ was chosen as the main nanowire axis (z'). This orientation exhibits slightly stronger quantum confinement effects in Bi nanowires[16], exhibits the highest ZT in single crystal bulk Bi-Sb alloys[39], and its high symmetry reduces the computational cost.

From the dispersion relation of the $\text{Bi}_{1-x}\text{Sb}_x$ nanowires, we tracked the energy shifts of the (highest subband) valence band and (lowest subband) conduction band edges as a function of nanowire diameter and composition. The relative position of the band edges determine whether the band structure of the nanowire is semimetallic or that of a semiconductor. Figure 2-7 depicts the rich variety of electronic band structures predicted for the $\text{Bi}_{1-x}\text{Sb}_x$ nanowire system as a function of wire diameter and antimony mole fraction. We identified five sections (or “phases”) in the (d_w, x) parameter-space, corresponding to the five electronic structures of $\text{Bi}_{1-x}\text{Sb}_x$ bulk alloys (Fig. 2-4). The semimetal and the indirect semiconductor states in the low antimony content region ($x \leq 0.13$) have the highest valence band extremum at the T-point, while those states at the higher antimony content region ($x \geq 0.13$) have their H-point hole pockets at the highest energy. Along the solid lines in this “phase diagram”, the extrema of the first subband of carrier pockets at two different points in the Brillouin zone coalesce in energy. The bold arrow in the center of the diagram points to a particularly interesting situation: At $d_w=60$ nm and $x=0.13$, the extrema of all 10 hole pockets coalesce in energy. This results in a high density-of-states for holes, which is beneficial for increasing the magnitude of the Seebeck coefficient in p -type samples (see Sect. 2.6).

The solid arc at the top-left corner of Fig. 2-7 identifies the boundary between semimetallic and semiconducting phases. Going across this boundary, the highest T-point hole subband edge passes across the lowest L-point electron subband edge, a phenomena referred to as the semimetal-to-semiconductor transition.[15, 55] The diagram predicts that the critical diameter at which the semimetal-to-semiconductor transition occurs shifts to larger diameter values as Sb is added to pure Bi. The transition to a narrow-gap semiconductor benefits the thermoelectric behavior, since

in the semimetallic phase, carriers of opposite signs make canceling contributions to the Seebeck coefficient. It is therefore expected that the increase of ZT values due to quantum confinement in nanowires will be observed at larger diameters in $\text{Bi}_{1-x}\text{Sb}_x$ nanowires when compared to Bi nanowires.

The “phase-diagram” in Fig 2-7 reveals one more significant difference between small-diameter nanowires and large-diameter nanowires (and bulk): The direct-bandgap phase, which exists in the bulk for alloys with 9% to 17% Sb, is reduced to a narrower range in the nanowires and ceases to exist for $d_W \leq 60$ nm. The direct-bandgap phase corresponds to the highest population of L-point holes, which have the highest mobilities, and therefore the best thermoelectric characteristics. The vanishing of the direct-bandgap semiconductor phase at small diameters indicates that in p -type $\text{Bi}_{1-x}\text{Sb}_x$ nanowires there are competing effects modifying the ZT as the nanowire diameter decreases: The ZT gains from the high density of states obtained from the reduction to a one-dimensional system, and it suffers from the depletion of the high-mobility low-mass holes at the L-points.

The optical properties of nanowires are of great interest, since sharp optical transitions and high quantum efficiency are expected from their characteristic density-of-states profile consisting of sharp singularities.[57] It is therefore interesting to note, that the direct bandgap in $\text{Bi}_{1-x}\text{Sb}_x$ nanowires is strongly dependent on the nanowire diameter, but it is almost independent of composition, as shown in Fig. 2-8. This is in contrast with the direct bandgap dependence on composition observed in the bulk (Fig. 2-4). It is, however, easy to realize that as the bulk bandgap decreases, the non-parabolic effect becomes more pronounced (Eq. 2.20). The effective mass components decrease (Eq. 2.21) due to the coupling between the bands, leading to a higher quantization energy, which counteracts the change in the bulk bandgap. This note is valid for the semiconducting nanowires only, as the L-point electron pocket in semimetallic nanowires is expected to be heavily populated, shifting the absorption edge to higher frequencies. Fig. 2-8 also indicates that the direct bandgap may be large for small diameter nanowires (for example, $E_{gL} > 200$ meV for $d_W < 20$ nm). The 2-band Lax model used in the calculation assumes, that E_{gL} is much smaller than the energy

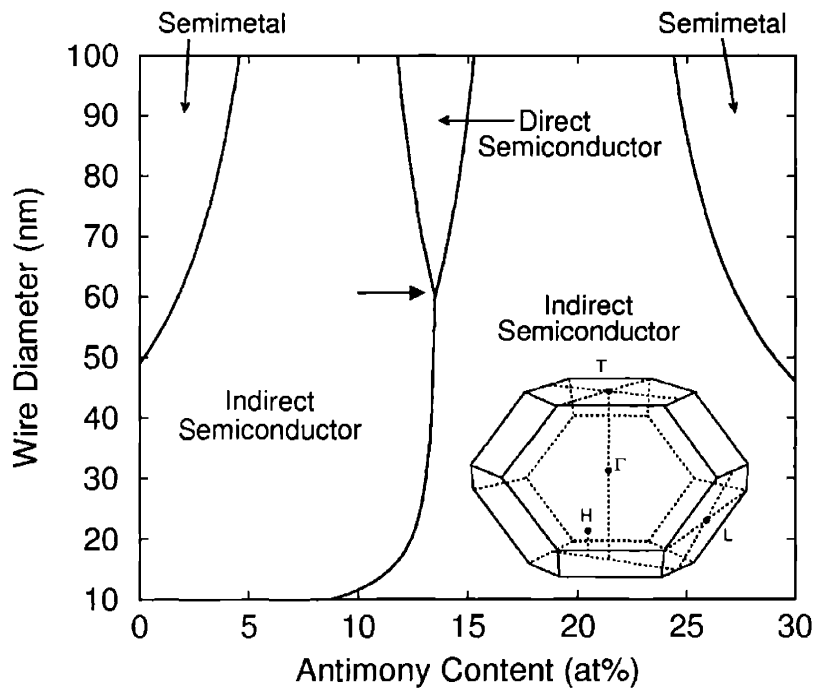


Figure 2-7: Phase diagram of the electronic band structure of $\text{Bi}_{1-x}\text{Sb}_x$ nanowires. The bold arrow in the center points at the condition where the 10 hole pockets (about the T-point, the 3 L-points and the 6 H-points in the Brillouin zone) coalesce in energy. The locations of these points in the Brillouin zone are shown in the inset.[56]

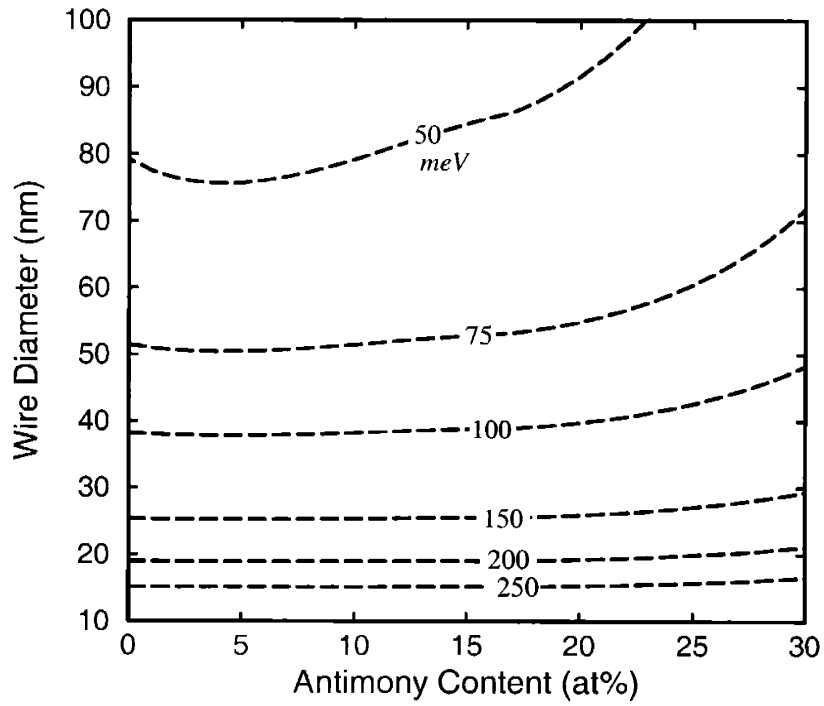


Figure 2-8: Contour plot of the direct bandgap energy at the L-point of $\text{Bi}_{1-x}\text{Sb}_x$ nanowires as a function of nanowire diameter and composition. Values shown are in *meVs*.

difference between the two coupled states and other electronic states at the L-point of the Brillouin zone. The calculated values of E_{gL} are smaller than the first excited state energies calculated for bismuth (1100 meV according to Golin[58], or 870 meV according to Rose and Schuchardt[59]) and for antimony (430 meV according to Rose and Schuchardt[59], 250 meV according to Liu and Allen[60], or 435 meV according to Falicov and Lin[33]), thus confirming the validity of the 2-band approximation, as it was used.

2.6 The Calculated Thermoelectric Properties of $\text{Bi}_{1-x}\text{Sb}_x$ Nanowires

Given the electronic band structure of the $\text{Bi}_{1-x}\text{Sb}_x$ alloy nanowires as a function of wire diameter d_W and antimony mole fraction x , the electrical conductivity (σ), the Seebeck coefficient (S) and the electronic contribution to the thermal conductivity (κ_{el}) were calculated using the semi-classical Boltzmann equations of motion within the constant relaxation time approximation.[61]

In the semi-classical picture, the motion of an electron in (r, k) space is described by the equations:

$$\frac{dr}{dt} = v(k) = \frac{1}{\hbar} \frac{dE(k)}{dk} = \frac{\hbar k}{m} \quad (2.24)$$

$$\hbar \frac{dk}{dt} = F_{externalfield} = q\mathbf{E} \quad (2.25)$$

For the flow of charged carriers in a one dimensional system, the electric current density and thermal current densities are given by:

$$j = -e \int \frac{dk}{\pi} v(k) g(k) \quad (2.26)$$

$$j_q = \int \frac{dk}{\pi} (E(k) - \xi) v(k) g(k) \quad (2.27)$$

where $g(k)$ is the non-equilibrium distribution function, and ξ is the chemical potential. Using the constant relaxation time approximation, and under a small perturbation from the equilibrium distribution, $g(k)$ has the form[61]

$$g(k) = g^0(k) + \tau \left(-\frac{df}{dE} \right) v(k) \left[-e\mathbf{E} + \frac{E(k) - \xi}{T} (-\nabla T) \right] \quad (2.28)$$

where $g^0(k)$ and $f(E)$ are the equilibrium and the Fermi-Dirac distribution functions, respectively, τ is the relaxation time, and T is the temperature. Plugging Eq. 2.28 into Eqs. 2.26–2.27, we obtain the current densities as a function of the electric field and the thermal gradient in the wire

$$j = L^{(0)}\mathbf{E} - \frac{1}{eT} L^{(1)}(-\nabla T) \quad (2.29)$$

$$j_q = -\frac{1}{e} L^{(1)}\mathbf{E} + \frac{1}{e^2 T} L^{(2)}(-\nabla T) \quad (2.30)$$

with the “ L -integrals”

$$L^{(\alpha)} = e^2 \tau \int \frac{dk}{\pi} \left(-\frac{df}{dE} \right) v(k)v(k)(E(k) - \xi)^\alpha \quad . \quad (2.31)$$

The quantities σ , S , and κ_{el} are derived from their definitions:

$$\sigma \equiv j \cdot \mathbf{E}^{-1}|_{\nabla T=0} = L^{(0)} \quad (2.32)$$

$$S \equiv \mathbf{E} \cdot (-\nabla T)^{-1}|_{j=0} = -\frac{1}{eT} \frac{L^{(1)}}{L^{(0)}} \quad (2.33)$$

$$\kappa_{el} \equiv j_q \cdot (-\nabla T)^{-1}|_{j=0} = \frac{1}{e^2 T} \left(L^{(2)} - \frac{(L^{(1)})^2}{L^{(0)}} \right) \quad (2.34)$$

and ZT is evaluated by Eq. 2.1. When evaluating the “ L -integrals”, $E(k)$ is given by Eq. 2.18, ξ is set equal to the Fermi energy E_F , $v(k)$ is given by Eq. 2.24, and τ is obtained from the mobility and the effective mass according to

$$\tau = \frac{\mu m_{z'}}{e} \quad . \quad (2.35)$$

The experimental values for the mobilities of the L- and T-point carriers in bulk bismuth and of the H-point pocket carriers in bulk antimony were used. The mobilities in the alloys have been determined experimentally only for a number of Bi-rich compositions, and the results are found to be sensitive to the sample quality.[34, 36, 62] From a theoretical standpoint, the effect of alloying on the mobility is hard to predict, since both the scattering time and the effective mass of the carriers will be affected. Therefore, regrettably, the composition dependence of the mobility had to be ignored. The lattice contribution to the thermal conductivity, needed to evaluate ZT , was obtained, in accordance with Matthiesen’s law, by fitting experimental results[39, 63] to the formula $\kappa_{ph}^{-1} = \kappa_0^{-1} + \kappa_1^{-1}x$, where κ_0 and κ_1 are constants. This fit is appropriate up to $x \sim 0.25$. Beyond this composition the experimental value of the thermal conductivity increases with Sb concentration. An additional constraint was imposed on the thermal conductivity, by setting its upper limit so that the effective phonon mean free path will not exceed the nanowire diameter.

The ZT dependence of the position of the Fermi level in the nanowires shows one maximum at carrier concentrations that correspond to an excess of negative carriers (denoted by $ZT_{n,opt}$) and one or two maxima at carrier concentrations corresponding

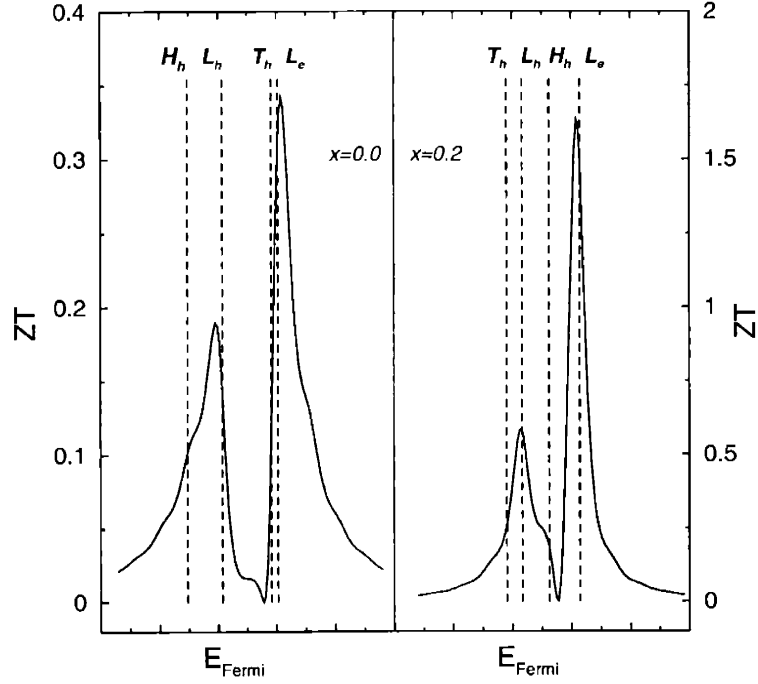


Figure 2-9: ZT versus Fermi energy position in a Bi (left) and a $\text{Bi}_{0.8}\text{Sb}_{0.2}$ (right) nanowire of diameter of 40 nm. The vertical dashed lines indicate the positions of the extrema of the various carrier pockets. The subscripts 'e' and 'h' indicate electrons and holes respectively. The minor ticks in the x -axis are spaced in intervals of 50 meV.

to an excess of holes (the highest among them denoted by $ZT_{p,opt}$). The maxima normally occur when the Fermi level is in the vicinity of the band edge of the first subband originating from one of the carrier pockets at the L-, T-, or H-points of the Brillouin zone. An example of the variation of ZT with Fermi energy position is shown in Fig. 2-9 for a Bi and a $\text{Bi}_{0.8}\text{Sb}_{0.2}$ nanowire 40 nm in diameter. The strong variation of ZT emphasizes the need to carefully control the doping of the nanowire to position the Fermi energy at its optimal position for thermoelectric performance. It also demonstrates the need to have a large density of states at the conduction- and valence-band edges, an effect that is achieved by low dimensionality, and by a high degeneracy of the carrier pockets.

The values of $ZT_{p,opt}$ and $ZT_{n,opt}$ were calculated at 323 non-uniformly spaced

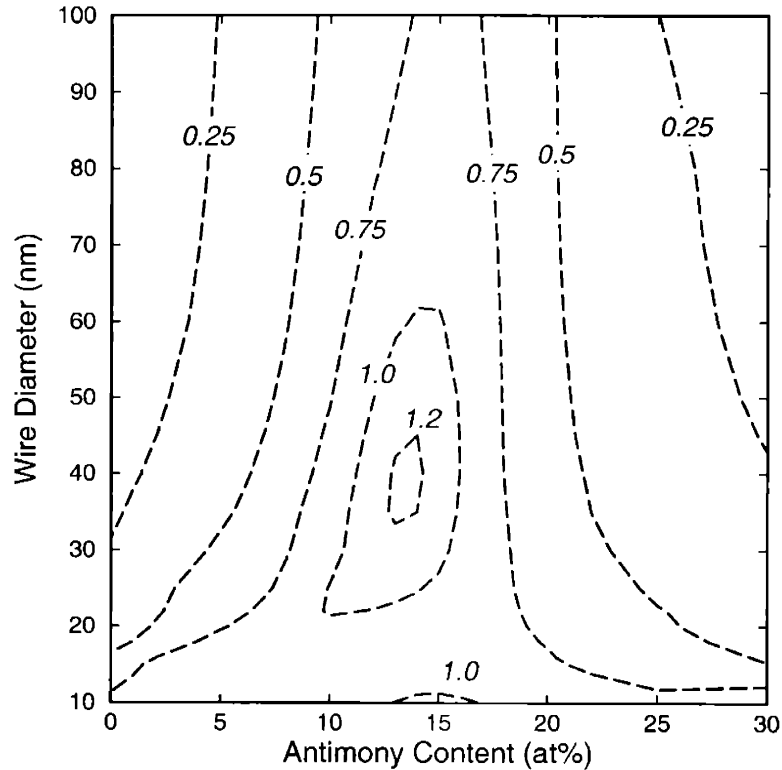


Figure 2-10: Contour plot of the optimal ZT values for p -type $\text{Bi}_{1-x}\text{Sb}_x$ nanowires vs. wire diameter and antimony concentration. The contour lines were generated using MATLAB from a grid of 323 non-uniformly spaced point calculations.[56]

points in the (d_W, x) space in the range of interest. From these results, two contour plots were constructed, shown in Figs. 2-10 2-11, estimating the “equi- ZT ” lines (i.e. contours of constant ZT values in the (d_W, x) space). The results for the n -type nanowires (Fig. 2-11) will be discussed first, and the discussion on the p -type systems (Fig. 2-10) will follow.

The contour plot of $ZT_{n,opt}$ for $\text{Bi}_{1-x}\text{Sb}_x$ in Fig. 2-11 reflects the trends previously observed in the bismuth nanowire system.[16] In particular, the value of $ZT_{n,opt}$ increases as the wire diameter decreases, for all values of x . As the content of Sb is increased at constant d_W , $ZT_{n,opt}$ increases until a certain optimal value of x (dependent on d_W) at which a maximum is reached. The dependence on d_W is explained by two main factors: (i) The change in the density of states and (ii) the semimetal-to-

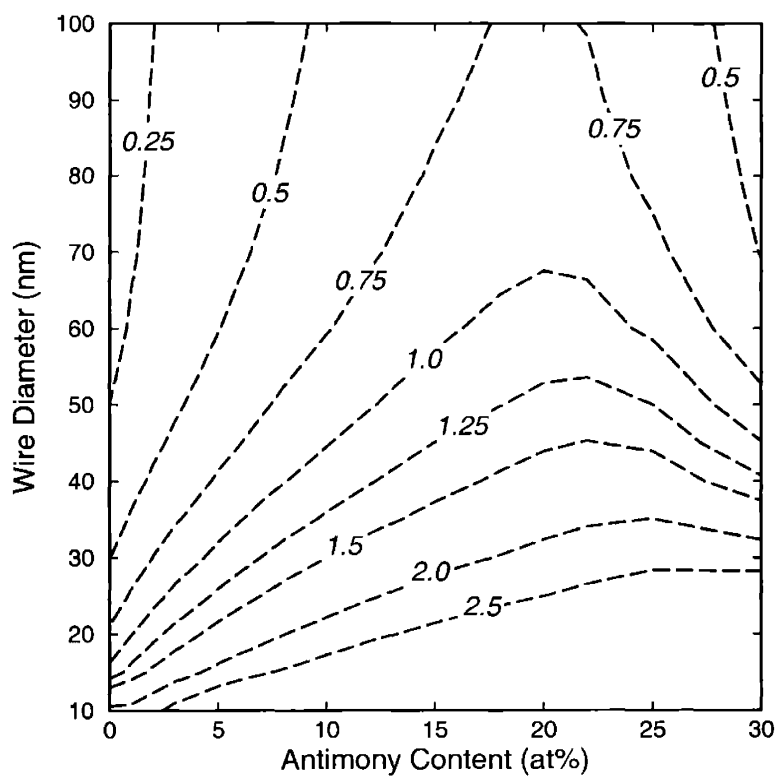


Figure 2-11: Contour plot of the optimal ZT values for n -type $\text{Bi}_{1-x}\text{Sb}_x$ nanowires vs. wire diameter and antimony concentration. The contour lines were generated using MATLAB from a grid of 323 non-uniformly spaced point calculations.[56]

semiconductor transition as the system is reduced from bulk form (three-dimensional) to a nanowire form (one-dimensional). The first refers to the evolution of the electronic structure into one consisting of sets of subbands in the nanowire electronic band structure. The diverging density of states at the extrema of a subband leads to high values of S and of ZT . The second factor is unique to the semimetals, in which the spatial confinement of carriers in the nanowire shifts the edges of the valence- and conduction-bands to lower and higher energies, respectively. These shifts effectively induce a semimetal-to-semiconductor transition, as the band overlap is eliminated and an energy gap is formed.[15,55] This was shown before in the context of the “phase diagram” of $\text{Bi}_{1-x}\text{Sb}_x$ nanowires (See Sect. 2.5). In the semimetallic state, both electrons and holes coexist, and their contributions to the Seebeck coefficient have opposite signs, due to the term $E(\mathbf{k}) - \xi$ in $L^{(1)}$. In the semimetallic state, the undesirable contribution of the minority carriers that lowers the magnitude of the Seebeck coefficient is further reduced by the proper positioning of the Fermi level. The dependence of $ZT_{n,opt}$ on x follows the same trend as in the bulk alloy, and is a consequence of two additional factors: (i) Bulk $\text{Bi}_{1-x}\text{Sb}_x$ is semiconducting in the range about $0.07 \leq x \leq 0.22$, with a maximum band gap at $x = 0.17$, and displays its best TE performance in this range.[30,39,41] (ii) The large mass difference between the atomic components of the $\text{Bi}_{1-x}\text{Sb}_x$ alloy gives rise to efficient scattering of phonons, thereby lowering κ_{ph} with increasing antimony content, while the carrier mobilities only slightly decrease as long as $x < 0.10$.

While mostly complying with these trends, the contour plot of $ZT_{p,opt}$ for p -type $\text{Bi}_{1-x}\text{Sb}_x$ nanowires in Fig. 2-10 shows a significant deviation relative to $ZT_{n,opt}$: a local maximum is found in the range $0.13 \leq x \leq 0.14$ and $35 \text{ nm} \leq d_W \leq 45 \text{ nm}$, with a predicted $ZT_{p,opt}$ value higher than 1.2 at 77 K. As seen in the plot, such high values of ZT in p -type materials are not expected for any other p -type $\text{Bi}_{1-x}\text{Sb}_x$ alloy at wire diameters above 10 nm, and are significantly higher than the bulk values. Unexpectedly, $ZT_{p,opt}$ does not increase monotonically with the reduction of the wire diameter. To understand the source of this unprecedented enhancement in $ZT_{p,opt}$, one should go back and reexamine the electronic band structure of the $\text{Bi}_{1-x}\text{Sb}_x$

nanowire system as depicted in Fig. 2-7. As was previously mentioned, the optimal ZT values are obtained when the Fermi energy is near a subband extremum. In the case of p -type nanowires, this is a hole subband extremum (Fig. 2-9). Of interest are the highest valence subband extrema, which occur at the three L-points, one T-point and six H-points of the Brillouin zone. It is in the vicinity of the point in the phase diagram where the merging of the edges of the 10 hole pockets occurs that the enhancement in $ZT_{p,opt}$ is observed. Furthermore, the region of high $ZT_{p,opt}$ seems to follow the boundary between the two indirect semiconductor phases, along which the H-point and the T-point pocket edges have comparable energies. It is this degeneracy that leads to an increased density of states near the Fermi energy for valence band carriers in p -type $\text{Bi}_{1-x}\text{Sb}_x$ nanowires, which in turn is manifested by the exceptionally high enhancement of $ZT_{p,opt}$ found in our calculations. This degeneracy is absent in the conduction band of this material system, and thus no maxima in $ZT_{n,opt}$ is expected. Another factor contributing to the appearance of the maximum in $ZT_{p,opt}$ is the relative weight of the high mobility L-point holes in the total carrier concentration (n_L/n). The ZT of n -type $\text{Bi}_{1-x}\text{Sb}_x$, for which only L-point electron carriers exist, is higher than that of p -type $\text{Bi}_{1-x}\text{Sb}_x$ where additional carrier pockets contribute to transport. Thus, the contribution of the L-pocket carriers to the enhancement of ZT is the most beneficial. The percentage of the holes contributed by the L-point subbands was calculated, and a contour plot of these values at optimal ZT_p was constructed (see Fig. 2-12). In the studied region, at the conditions for optimal ZT_p , the calculations suggest that the partial population of the L-point holes reaches a maximum of 28% for $\text{Bi}_{0.88}\text{Sb}_{0.12}$ with $d_W=100$ nm. It drops to 7% of the hole population as the antimony mole fraction increases to 0.165 or the wire diameter decreases to 15 nm. The depletion of the L-point hole population with increasing x for $x \geq 0.12$ is in agreement with the observation that, for a given wire diameter, the peak in $ZT_{p,opt}$ occurs at lower concentrations of antimony than the peak in $ZT_{n,opt}$: In the p -type systems, the benefit of alloying is countered by the increase in the population of non-L-point holes. The existence of the local maximum in $ZT_{p,opt}$, and the fact that the maximum does not appear at the same diameter and composition

as the 10 hole subbands alignment, are therefore explained as an interplay between the lower population in the L-point hole pockets and a higher subband edge density-of-states, as we decrease the diameter of the $\text{Bi}_{1-x}\text{Sb}_x$ nanowires. The fact that the direct bandgap phase ceases to exist below the wire diameter of 60 nm undermines the effort to make use of the quantum confinement effects for thermoelectricity at small diameter *p*-type nanowires. The general understanding of thermoelectricity in low-dimensional systems gave rise to the notion that ZT values monotonically increase with the reduction of size of the confined dimension. This is the first example of a system, in which this principle does not hold.

2.7 Limitations of the Model

Several assumptions were made to simplify our modeling of the $\text{Bi}_{1-x}\text{Sb}_x$ alloy system to a tractable problem, preserving the important physical aspects of the system. The main weakness of the model comes from the lack of information regarding the mobilities of the different carriers as a function of alloy composition. The experiments necessary to obtain such information are challenging with regards to the sample preparation. Contradictory results from bulk samples suggesting either the conservation or the strong decrease of mobility upon alloying bismuth with antimony can be found. The extension of these studies to nanowire system will be necessary as well, as we predict changes in the energies of the band edges, and in the dispersion relations in general. Such changes are bound to affect the scattering probabilities, and thus the carrier mobilities. For example, along the “phase transition” lines, inter-valley scattering processes might play a dominant role, strongly influencing the mobilities and the figure-of-merit ZT .^[41] Thus, in this respect, the values observed here represent an optimistic estimate for the thermoelectric performance of this nanowire system. However, even though the calculated values necessarily include uncertainties, the concepts unveiled by this work in the $\text{Bi}_{1-x}\text{Sb}_x$ alloy nanowire system, namely the phase diagram characteristics, the alignment of all the hole pockets, and the non-monotonic behavior of ZT with respect to nanowire diameter, are not sensitive to the accuracy

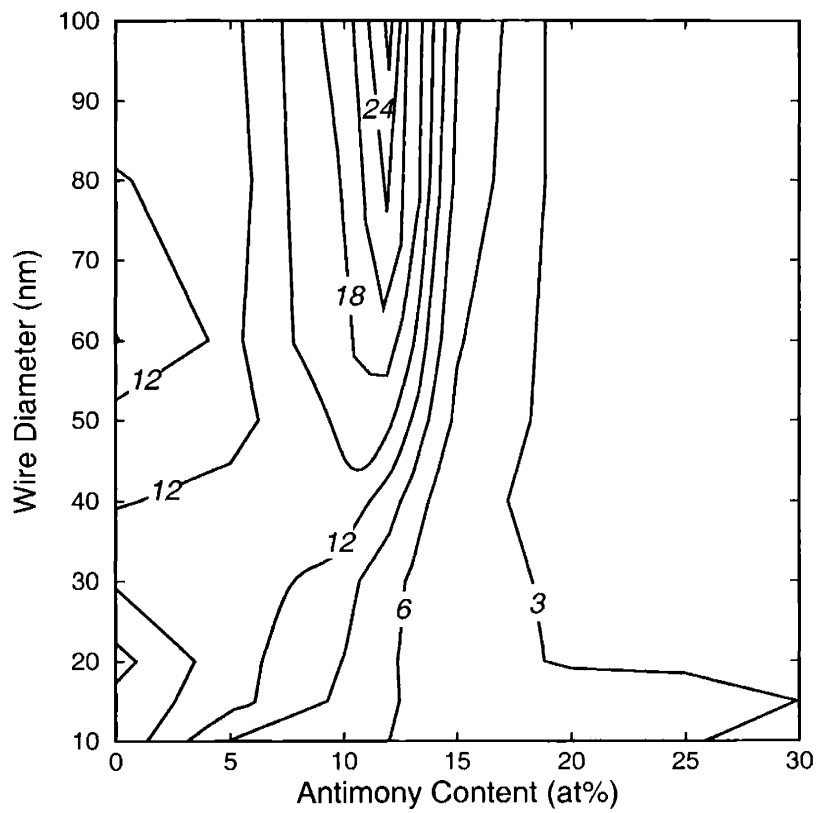


Figure 2-12: Contour plot of the percentage of holes populating the L-point subbands in optimal ZT -optimized p -type $\text{Bi}_{1-x}\text{Sb}_x$ nanowires vs. wire diameter and antimony concentration. The contour lines were generated using MATLAB from a grid of 323 non-uniformly spaced point calculations.

of the model and are expected to hold true.

2.8 Experimental Verification of the Model

The model presented above has a great predictive power in determining the effects of quantum confinement in a nanowire on the thermoelectric properties. The model is also very simplistic. It has been assumed that the key features of the electronic band structure of the bulk are conserved in the nanowires, and the electronic band structure of the nanowire can be derived from it, by imposing a confining potential in two dimensions. One must therefore question whether these simplifications are justified.

Several experimental studies produced Bi and $\text{Bi}_{1-x}\text{Sb}_x$ nanowire samples, and their investigations support the validity of the model calculations described in this chapter. First, x-ray diffraction studies of bismuth nanowires down to 23 nm in diameter prepared by template synthesis (Ref. [15, 64] and Chap. 4) show that the crystal structure of bismuth is conserved in the nanowires. The conservation of crystal structure is a necessary (but not sufficient) condition for the electronic band structure to be conserved. Transport studies on bismuth nanowire arrays prepared by a gas-phase impregnation technique [15] and transport studies on $\text{Bi}_{1-x}\text{Sb}_x$ nanowire arrays prepared by a pressure injection technique [65, 66] provided evidence in support for a semimetal-to-semiconductor transition, as predicted by the calculated “phase diagram” of $\text{Bi}_{1-x}\text{Sb}_x$ nanowires (Fig. 2-7). For bismuth nanowires, the transition occurs at a diameter of about 50 nm, and for 65 nm diameter $\text{Bi}_{1-x}\text{Sb}_x$ nanowires, the transition occurs at 2 at-% antimony. Furthermore, the experimental resistance of the arrays of nanowires in the semiconducting regime becomes less sensitive to temperature as one “moves away” from the transition diameter and composition. These results are in accordance with an increase in the bandgap, as the nanowire diameter decreases or as the antimony content increases (up to $x = 0.15$). Finally, the Seebeck coefficient of nanowire arrays with $d_W = 45$ or 65 nm and $x = 0$ or 0.05 was determined experimentally. The Seebeck coefficient increased as predicted by the

calculations, being the highest for the low diameter, high antimony content sample among the four samples examined.[66]

2.9 Summary

In summary, a simple model used for the evaluation of ZT and other transport properties of nanowires was presented. The model was applied to the mixed-carrier multi-pocket electronic structure of $\text{Bi}_{1-x}\text{Sb}_x$ alloys. An electronic band-structure phase diagram was constructed showing semimetal-to-semiconductor transitions and hole pocket alignment conditions for $\text{Bi}_{1-x}\text{Sb}_x$ nanowires. Optimal ZT_p and ZT_n values are calculated. A non-monotonic dependence of ZT on wire diameter was discovered in p -type systems, and explained in terms of the relative contributions of the various carrier types to the transport. The limitations of the model were discussed and experimental data supporting the model were presented.

The model can be easily applied to a two-dimensional system (thin $\text{Bi}_{1-x}\text{Sb}_x$ films). Two-dimensional systems have the advantage that they can be fabricated with excellent control over thickness, composition, and doping by molecular beam epitaxy. However, since only one dimension is quantized in the films, the thicknesses of the films necessary to observe substantial effects on the transport are lower ($d < 10\text{nm}$) than the corresponding nanowire diameters. Surface effects are expected to be more dominant, and are harder to model. Nonetheless, measurements and device fabrication with films are easier to perform, and important information regarding to quantization of the electronic band structure in bismuth can be obtained. These data, in turn, will help improve the models for the nanowire system.

Chapter 3

Modified Porous Anodic Alumina Templates

3.1 Background

The anodization of metals[67–69], and in particular the anodization of aluminum[70–72], has been extensively studied for many decades, since the resulting oxide coatings are of practical interest for protective and decorative finishing. Anodic coatings are formed when a metal is used as (a part of) an anode in an electrochemical setup and a large voltage (typically 5–200 V) is applied. The anodization process can be carried out at a constant voltage or at a constant current density. Depending on the generation conditions, i.e. the electrolyte chemistry, the voltage or current density control mode, the temperature, and the metal used, the anodic coating can be dense or porous.

Dense coatings are commonly formed under constant voltage conditions. The current decays with time, and goes to zero, once a certain oxide thickness has been reached. For this reason dense coatings are also known as barrier-layer type coatings.[70, 72] Every metal usually exhibits a constant barrier layer thickness-to-voltage ratio.[69, 70]

Porous anodic film formation is, on the other hand, a steady state process, in which the film thickness increases with time. The porous film evolves from the pitting action

of the electrolyte on the initially formed barrier layer oxide (oxide dissolution). The pitting process is usually facilitated by the local electric field, making it strongly dependent on the voltage and on the surface morphology.[71] Since the pitting leads to the local thinning of the barrier layer oxide, more metal is subsequently converted into oxide to conserve the constant barrier layer thickness-to-voltage ratio.[71, 73] Thus, a porous film is formed between the electrolyte and the metal, with a barrier-layer of constant thickness at the interface between the oxide and the metal. In the steady state condition, equal rates are established for the oxide dissolution and the oxide formation across the barrier layer, and the current density is constant with time.

3.1.1 The Structure of Porous Anodic Alumina

Porous anodic alumina (PAA) films[71] are particularly interesting, because under certain anodization conditions, ordering of the pores may be achieved.[74–76] The pores in ordered PAA films grow perpendicular to the aluminum surface (along the electric field lines) resulting in arrays of parallel channels.[71] Schematic drawings of the structure of PAA are presented in Fig. 3-1. In perfectly ordered regions, the channels are organized in a close-packaged triangular array, as shown in the scanning electron microscopy image of the top surface of an ordered PAA films in Fig. 3-2. Each pore is located in the center of a hexagonal alumina cell, and the pore cross-section is approximately circular. The sizes of the pore and the cell are related to the applied voltage in an almost linear fashion.[75] The pore diameter can be varied from 7 to ~ 200 nm, and the interpore distance (or cell diameter) can be varied from 20 to 500 nm. These two structural quantities are strongly coupled during the anodization process, but the pore diameter can be modified independently by post-anodization pore enlargement in an etch solution. The ordering of the pores into a hexagonal lattice improves with anodization time, as the pores elongate, resulting in defect-free domains a few microns in size. Larger domains can be obtained by seeding the pore initiation sites, by e-beam lithography[77, 78] or imprint lithography[79]. The formation of this self-organized nanoscale structure via the simple process of

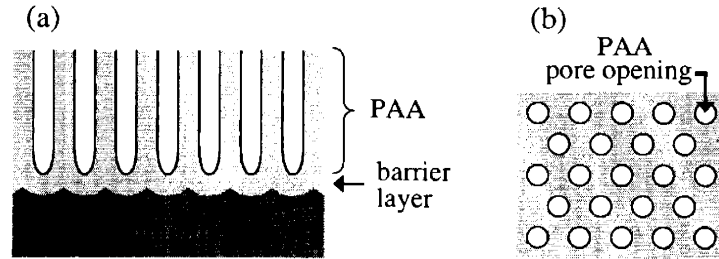


Figure 3-1: Schematic representation of the structure of a conventional porous anodic alumina film [(a) vertical cross section (b) top surface].

anodization is so far unique to aluminum among the metals. Similar structures were obtained in semiconductors (silicon[80], III-Vs[81]). These systems, however, are more difficult to control and the structural features of their arrays are somewhat larger (periodicities in the range of 50 nm to 10 microns).

3.1.2 The Preparation of Porous Anodic Alumina Templates

The fabrication process of the PAA films on aluminum sheets is schematically illustrated in Fig. 3-3. Various fabrication recipes are available in the literature sharing the processing steps shown in the figure (see for example Refs. [70], [72], and [75]). Here, the recipe most commonly used by the author and coworkers, before adopting the modifications discussed in the chapter, will be presented.[64]

A sheet of aluminum (99.997% metal purity, 2cm*1cm*0.25mm) was flattened between glass sides with a pneumatic press. The sheet was mechanically polished on a polishing wheel, using polishing solutions with decreasing particle size (50 nm colloidal silica suspensions were used in the last step). The sheet was cleaned by sonication in water, acetone, and isopropanol, and annealed in air at 350°C for one hour. The roughness of the aluminum sheet surface was further reduced by an electrochemical polishing step: The aluminum was used as the anode in a system, consisting also of a platinum cathode and a polishing bath of 76 mL H₃PO₄ (assay: 85%), 4 mL H₂SO₄ (assay: 97%), and 1.6 g CrO₃ at 85°C. A voltage of 20 V was applied for

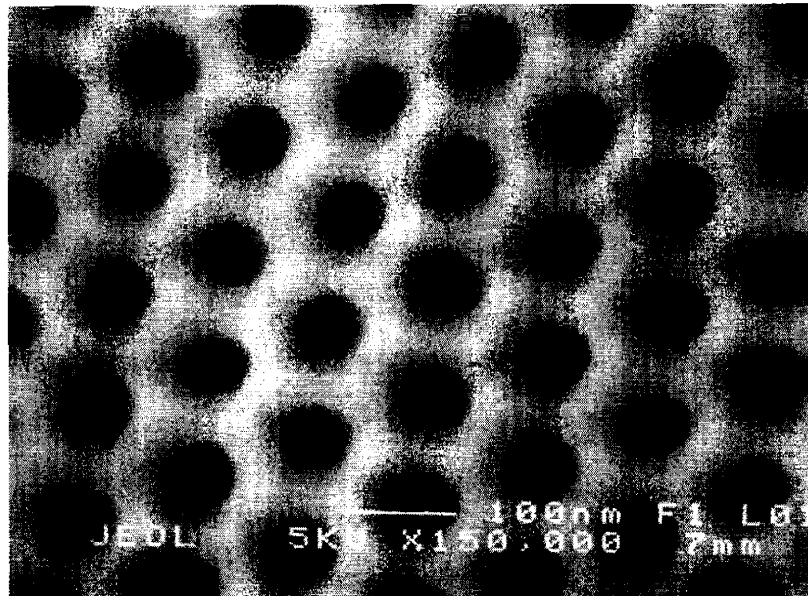


Figure 3-2: SEM image of the top surface of a PAA film with an ideal pore ordering structure (pore diameter = 55 nm; center-to-center pore separation = 100 nm).

10–30 secs, while limiting the current density to 2 A/cm². Immediately prior to the anodization, the aluminum was dipped for at least 20 min in an aqueous etch solution of 3.5 vol% H₃PO₄ and 45 g/L CrO₃ to remove the native oxide formed under ambient conditions. A typical anodization was carried out at room temperature in a 4 wt% oxalic acid aqueous solution at 40 V, yielding a porous structure with an average interpore distance of 100 nm and pore diameters of 35–40 nm. To improve the ordering of the pores a “double anodization process” was adopted.[82] The process builds on the improvement of the hexagonal ordering of the pore array with time. The anodization was first carried out for 2–4 hours. The PAA film was etched away in the above mentioned H₃PO₄/CrO₃ etch solution for ~12 hours, exposing the underlying aluminum substrate, whose surface was indented with a triangular array of concave depressions as a result of the anodization process (Fig. 3-1a). Each depression serves as a nucleation site for pore formation in a subsequent anodization step. Thus, the PAA film formed in the second anodization of the film has a significantly more ordered structure and more uniform pore diameters than the film obtained from the

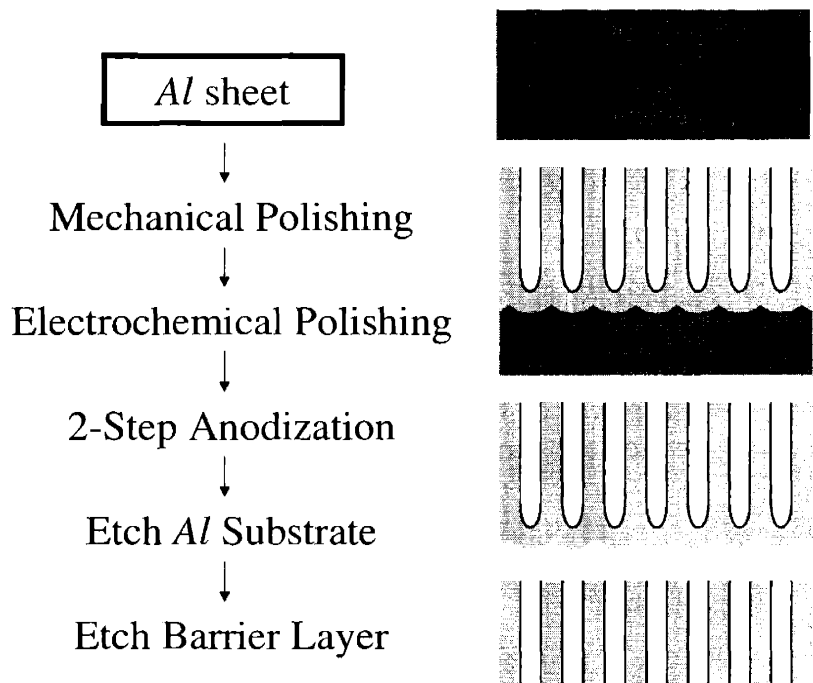


Figure 3-3: Main processing steps in a typical preparation of PAA films on aluminum sheets. The drawings represent the cross section structure of the film at different preparation stages. From top to bottom: Polished Al sheet, PAA film on Al sheet, free-standing PAA film, and through-channel PAA film.

first anodization. The length of the second anodization step is chosen to achieve the desired film thickness, with the relation $thickness(nm) \approx 200 * time(min)$. During the anodizations, the back side of the aluminum sheet was covered with an insulating film (Crystalbond, Buehler) to maximize the current efficiency. After the anodization, the pore diameter was modified by etching in a 5 vol% H_3PO_4 aqueous solution. When necessary, the aluminum substrate was etched away in a 0.2 M $HgCl_2$ aqueous solution to give a free-standing PAA film. The barrier layer could be subsequently etched away by soaking in a 5 vol% H_3PO_4 solution for 20 min, to obtain a membrane with pore channels running from side to side. To prevent pore enlargement, the top surface was covered during the etching of the barrier layer.

In this chapter, we will describe alternative methods that were developed for the preparation of high-quality PAA films suitable for the templating of nanostructures. The main part of the chapter will introduce the fabrication of PAA films on rigid substrates, and demonstrate their use as templates. The last section will discuss improvements made to the process of preparation of aluminum-supported PAA films, as described in the above paragraph.

3.2 Motivation

Porous anodic alumina films are made of amorphous hydrated alumina. These films are thin (with thickness up to several tens of microns) and brittle. It is very difficult to prepare large area samples without defects, and it is very difficult to manipulate the free-standing films without compromising their integrity. Even when supported by the aluminum sheet, the films are sensitive to mechanical forces, since aluminum is a soft metal and thin sheets of aluminum deform. Thus, PAA films are commonly limited in area to a few cm^2 .^[83] Furthermore, PAA films formed on aluminum sheets have a significant amount of inhomogeneities, which deteriorate the optical properties of these structures. The inhomogeneities result both from impurities in the original aluminum film and from defects introduced during the polishing steps: mechanical polishing leaves scratches of the surface, while electrochemical polishing enhances

grain boundaries in the polycrystalline aluminum.

It is therefore of value to develop a method to grow porous anodic alumina films on rigid substrates. The strength of the substrate will serve to protect the PAA film from bending and cracking. The substrate will also serve as a handle for the manipulation of the PAA film on it, making it possible to process the porous films in ways that thus far have compromised their integrity.

The method of growing porous anodic alumina films on rigid substrates needs, however, to satisfy several requirements in order for its implementation to be worthwhile.

1. The process should not be substrate specific.
2. The process should require minimum substrate-preparation steps.
3. The process should not compromise or modify the porous structure of the PAA.
4. The process should be suitable for the preparation of PAA films by a variety of recipes, in a variety of porosities, and in a wide range of thicknesses.
5. Most importantly, the process should afford PAA films without a barrier layer blocking the bottom of the pores, or the process should allow for the removal of the barrier layer without the need to separate the PAA from the substrate.
6. The additional cost of fabrication should be low and predictable.

While there has been some success in growing PAA films on silicon wafers, the reported processes failed to satisfy points (4) and (5) above.[84–94]

3.3 Growth of Porous Anodic Alumina Templates on Rigid Substrates from Evaporated Aluminum Films

In this section, we investigate the influence of the various processing steps on the growth of PAA films on silicon and on glass substrates. We briefly discuss the me-

chanical, structural and optical properties of the resulting structures, and present a model for the structural evolution of the barrier layer at the PAA–substrate interface.

3.3.1 Influence of Aluminum Evaporation Methods, Annealing, and Polishing on Porous Anodic Alumina Formation on Silicon Wafers

In order to prepare PAA films on rigid substrates, thick films of aluminum were deposited on silicon wafers, and the conversion of these films to PAA by anodization was examined. Three deposition methods were tested: Physical vapor deposition (PVD), electron-beam (e-beam) evaporation, and thermal evaporation. The tools were used to deposit films of at least 1 micron in thickness. The substrate temperature was not controlled. The aluminum films were not polished. They were used as-deposited, except for the removal of the native oxide right before the anodization step. A double anodization process was carried out at 45 V in a 4 wt% oxalic acid aqueous solution.

The three deposition methods resulted in PAA films of poor quality. The anodized surfaces of a PVD and a thermal evaporation sample after the first anodization are shown in Fig. 3-4. It is evident that hexagonal pore ordering was not achieved, pore diameter variations are large, and there is a high concentration of defects. It is known that the surface quality of the aluminum film has a strong influence on the anodization results[95, 96] Even though the films were observed to have a mirror finish, SEM and AFM observations indicated that the roughness in the films was significant (see Figs. 3-5-3-7) compared to polished samples of commercial aluminum sheets. The surface roughness is expected to disrupt the pore nucleation and ordering processes.

Another structural factor influencing the anodization is the uniformity of the film density obtained by the different deposition techniques. Indirect information about the film homogeneity is obtained from the analysis of the crystal domains. The formation of large crystalline grains indicates that atomic diffusion on the surface

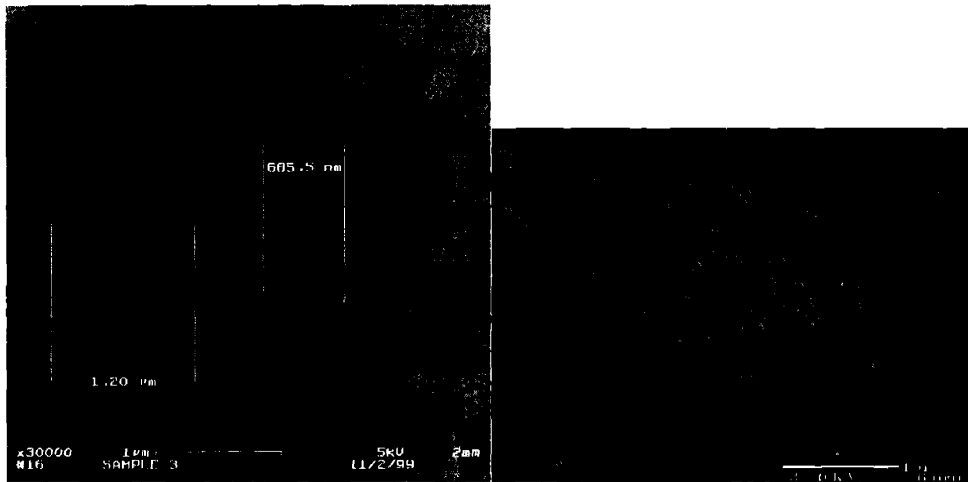


Figure 3-4: SEM images of anodic films on as-deposited PVD aluminum (left) and thermally evaporated aluminum (right). Both samples show poor pore ordering and large defects at grain boundaries.

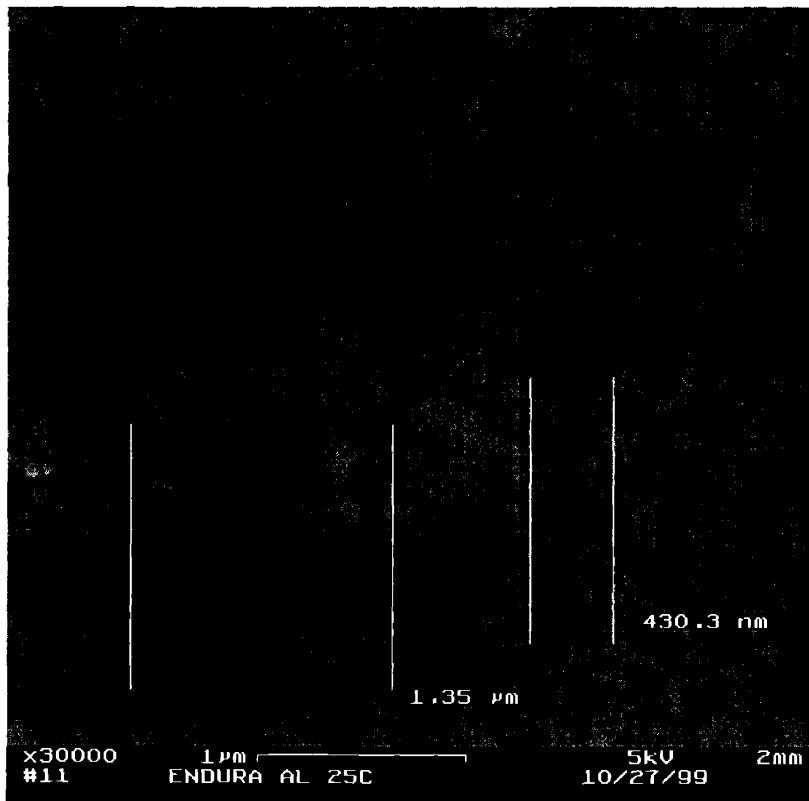


Figure 3-5: SEM image of the top surface of an as-deposited PVD aluminum film.

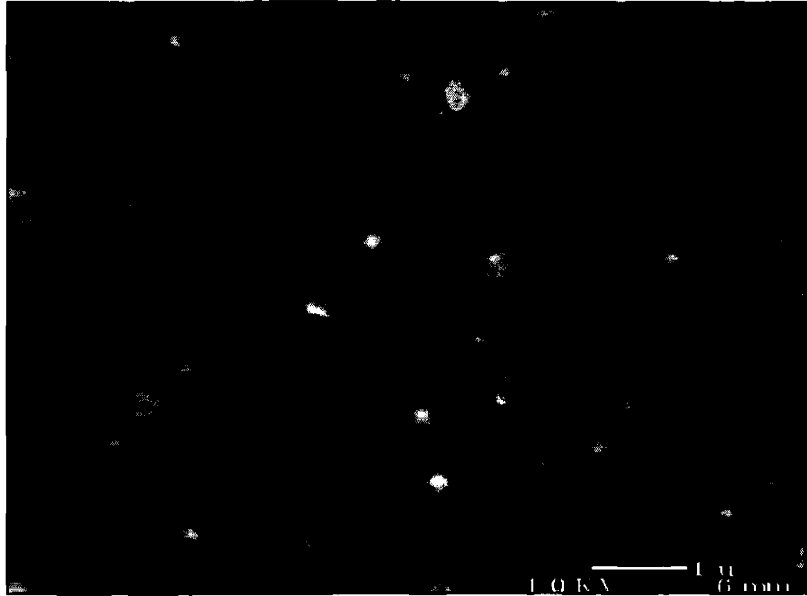


Figure 3-6: SEM image of the top surface of an as-deposited e-beam evaporated aluminum film.

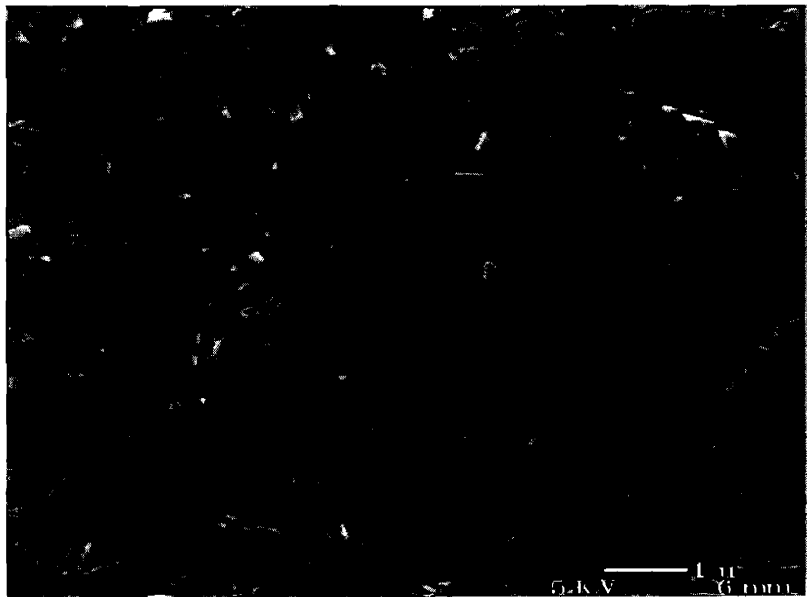


Figure 3-7: SEM image of the top surface of an as-deposited thermally evaporated aluminum film.

was occurring under the film growth conditions. Thus, samples with large grains are expected to be denser, including voids only along the grain boundaries, while finely-structured samples are expected to be less dense, with unfilled volumes at random positions. The top surface SEM images of the aluminum films (Figs. 3-5-3-7) show that the grain sizes are larger for the thermally evaporated sample than for the e-beam evaporated sample. No grain structure was recognized in the SEM images of the PVD sample, indicating that the film is made of fine agglomerates smaller than 20 nm in size. Numerous voids in the PVD film can be identified in Fig. 3-5. Cross sectional SEM images of the anodized films were inspected for the presence of voids in the film, and their effect on pore growth. The cross section image of the PVD sample in Fig. 3-8 shows, in addition to the disordered pore channel structure, the presence of voids in the film. These voids are also indicative of the porosity of the original aluminum film. Leakage of the electrolyte through the voids disrupted the uniformity of the anodization. The cross section image of the thermal evaporation sample (not shown) did not show voids in the pore walls, and the pore channels were relatively straight. This indicates that the bulk structure of the film obtained by thermal evaporation is the most dense, and the most appropriate for sustaining a uniform anodization. The lack of pore ordering was only the result of surface roughness and limited film thickness. Due to the small thickness of the films, the first anodization could be carried out only for a limited duration of time, before a high degree of pore ordering was achieved.

To improve pore ordering and pore diameter uniformity, thermally evaporated aluminum samples were annealed at 400°C for 3 hours and/or electrochemically polished. The samples were then anodized, and subsequently inspected by SEM. There was no noticeable effect of the annealing process on the porous film morphology. On the other hand, electrochemical polishing greatly improved the appearance of the aluminum films (increased reflectivity) and greatly improved the pore ordering in the PAA films. Comparison of Fig. 3-9 and Fig. 3-4 shows that the electrochemical polishing of the surface resulted in the formation of pores with more uniform diameters, and the elimination of defects at voids and sharp surface features.

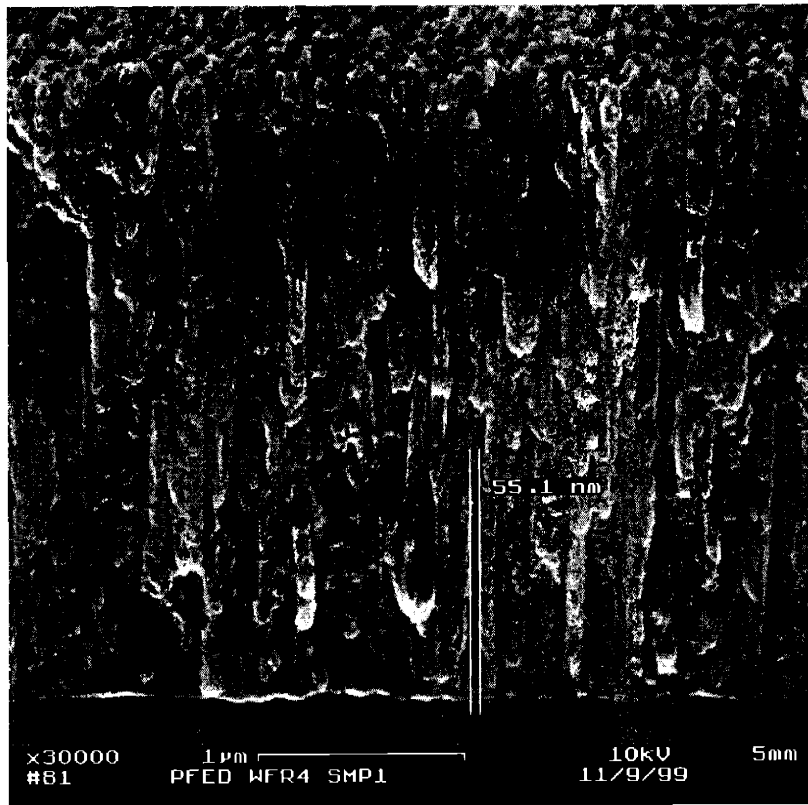


Figure 3-8: SEM image of the vertical cross section of a PAA film formed by the anodization of an as-deposited 10 micron thick PVD aluminum layer on a silicon substrate.

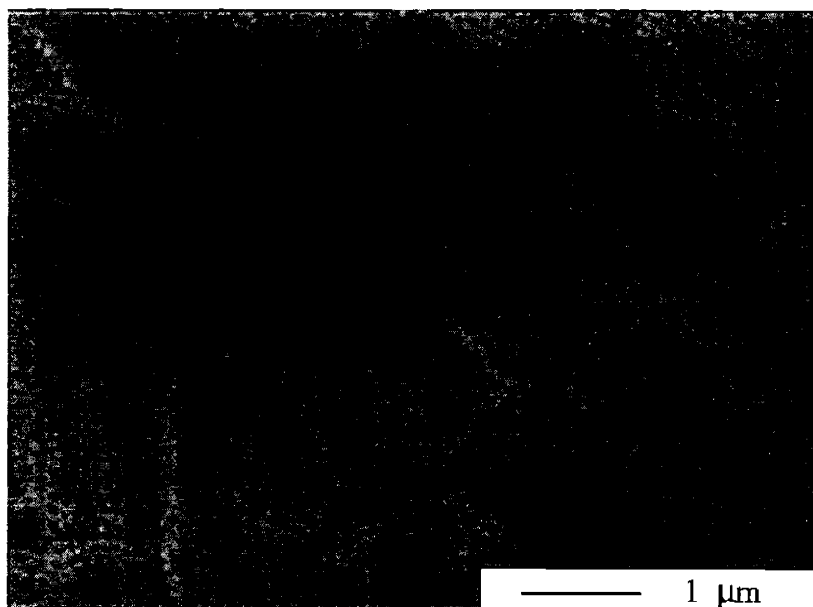


Figure 3-9: SEM image of the top surface of a PAA film formed on a thermally evaporated aluminum film that was electrochemically polished before anodization.

The need to employ an electrochemical polishing step to generate good PAA films from evaporated aluminum films raises a question about the amount of aluminum that is lost in the polishing process, considering that the evaporation tool imposes a limit on the amount of material that can be deposited. In contrast to the electrochemical polishing step for mechanically polished aluminum sheets, the electrochemical polishing process for thermally evaporated films required the duration of only 1 sec, since the films are of good finish quality to begin with. Profilometry (Tencor P-10 Surface Profilometer) showed that the thickness loss due to the electrochemical polishing was approximately 70 nm.

The process was modified further to increase the film thickness resulting from the thermal evaporation of a charge of aluminum onto the wafer. The position of the wafer in the thermal evaporator chamber was changed, so that the distance from the aluminum source was reduced from the chamber standard of ~ 60 cm to a distance of ~ 15 cm. This modification led to the increase of the average film thickness obtained from an ~ 1 cm³ pellet of aluminum to ~ 10 μm. The films had notably worse surface

quality after the modification, but the surface imperfections were removed by the electrochemical polishing step. An inevitable result of the modification is that the film thickness varied significantly across the sample (up to 50% of the maximum thickness across a 4 inch wafer). It was also shown that multiple evaporations of aluminum can be employed on the same substrate to obtain thicker aluminum films. Even though the vacuum conditions were broken in between the subsequent evaporations, and the wafer surface was exposed to air for several minutes, the cross section of the PAA film did not show structural discontinuities at the interface between the first and second evaporated layers. However, if the first aluminum layer was deposited by PVD and the second by thermal evaporation, the pores of the PAA grew straight across the external layer, but then became disordered in the inner layer.

Thus, PAA films were successfully grown on silicon wafers via the thermal evaporation of aluminum, electrochemical polishing of the obtained film, and anodization under conventional conditions. Methods for increasing the aluminum mass deposited on the wafer were successfully tested. The increase of the aluminum layer thickness leads to an improvement of the pore ordering. SEM images of good quality films obtained on silicon via the newly developed process are shown in Fig. 3-10. The cross section image shows that the pores are straight and parallel, except when defects were found on the surface. If the defect was small and the film thickness was large enough, the self-organizing property of the anodization process gradually repaired the pore disorder caused by the defect. This is observed in the shape of the pores coming out of the small defect in the cross section image in Fig. 3-10. The improved hexagonal ordering of the pores can also be deduced from the comparison of the images of the top and bottom surfaces of the film in Fig. 3-10.

3.3.2 The Anodization Process on a Silicon Substrate

In order to maximize the thickness of the PAA films, and possibly remove the barrier layer, the complete conversion of the aluminum films to anodic alumina was attempted. The instance in which the aluminum film converts fully into PAA is easily detectable by following the color change of the film from metallic to transparent.

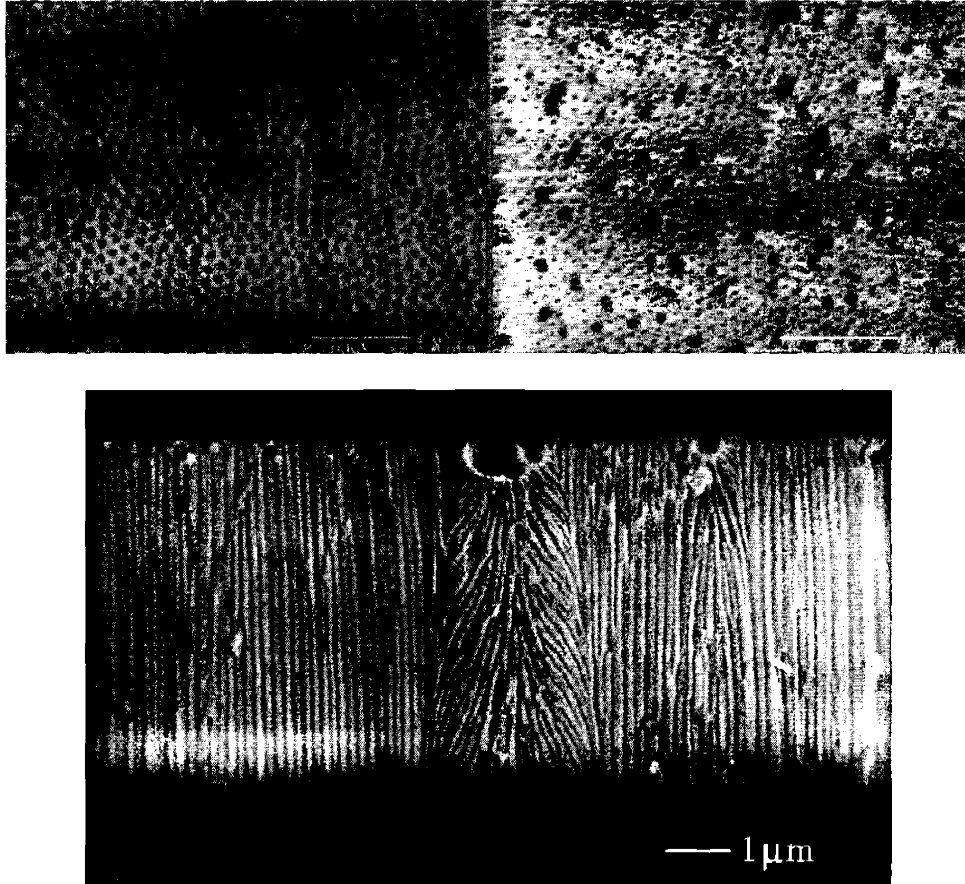


Figure 3-10: Top surface (top left), bottom surface (top right) and cross section view (bottom) of a good quality PAA film formed on a silicon wafer by the thermal evaporation of a thick film of aluminum, electrochemical polishing, and a double anodization process (see text).

The complete anodization process was carried out on thermally evaporated films of large aluminum film thickness ($> 2\mu\text{m}$). A cross section view of the anodized film (Fig. 3-11) showed that the morphology of the barrier layer was different than that of barrier layers obtained between PAA and aluminum sheets, as described in a previous report.[84] Instead of a scalloped edge interface, with convex structures penetrating the aluminum layer (as in the scheme in Fig. 3-1), the barrier layer interfacing with a rigid silicon crystal was found to have a planar interface with convex structures pointing into the PAA film (Fig. 3-11). The pore bottom is split around the convex structures. Such a barrier layer is termed "inverted". A plausible mechanism for the barrier layer inversion is presented schematically in Fig. 3-12. As the barrier layer approaches the silicon wafer, the tips of the scalloped barrier layer will reach the wafer first, creating a series of ridges of aluminum at the interface. This situation changes the distribution of the electric field at the bottom of the pore. The electric field is stronger at the sides of the pore bottom than directly underneath it. Thus, the pore growth direction changes and the pores begin to grow sideways. At this stage, the newly formed alumina is located underneath the pores walls, while the alumina directly underneath the pore channel can only dissolve but not grow in thickness. Considering the volume expansion during the conversion of aluminum to alumina[97], the net result is lateral forces within the barrier layer from the periphery of the pore inwards (indicated by arrows in Fig. 3-12). If the adhesion between the barrier layer and the wafer is weak, or is weakened by anodic reactions at the interface, the structure can relax by detaching the thinner portions of the barrier layer from the wafer, and bending it into the pore space. Thus, the barrier layer at the pore will be inverted, and a void will appear underneath it.

Interestingly, the experiment revealed, that unless the anodization was stopped as soon as the entire aluminum film was converted into PAA, the PAA film spontaneously detached from the silicon wafer, and a free-standing film was obtained (see Fig. 3-13). The film delamination is the result of the strain accumulated in the PAA film due to the volume expansion during the conversion of aluminum to PAA[97], of anodic reactions at the wafer surface that generate oxygen bubbles, weakening the adhesion

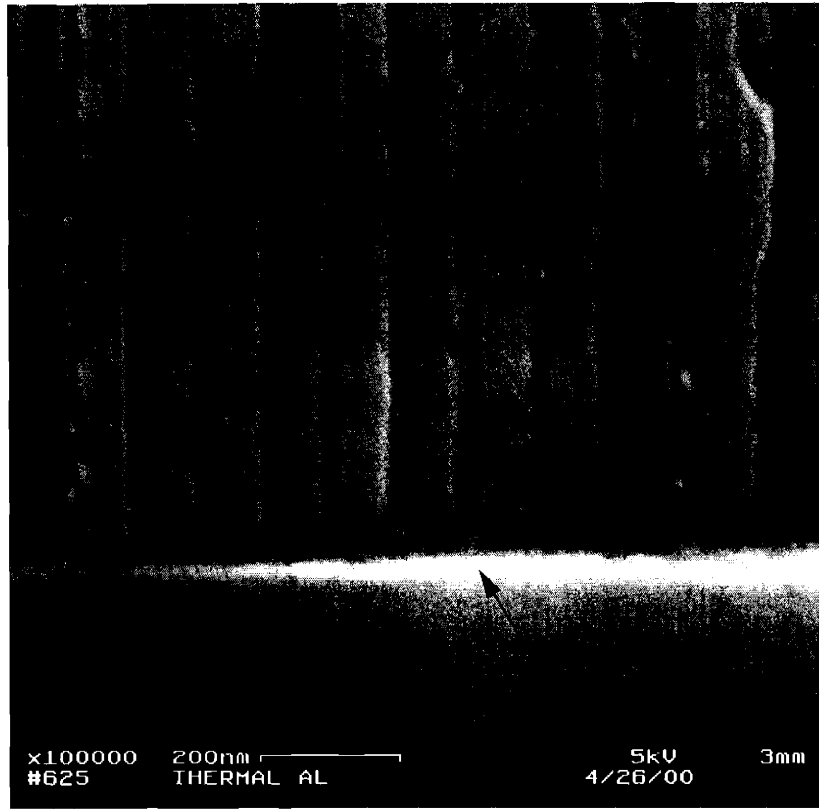


Figure 3-11: SEM image of the inverted barrier layer at the interface between PAA and silicon generated by the complete anodization of the film on the wafer.

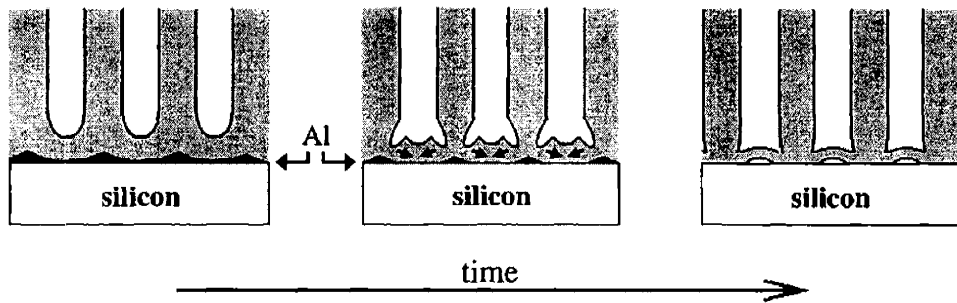


Figure 3-12: Schematic representation of the mechanism of barrier layer inversion at the PAA-silicon interface. The arrows in the drawing in the center indicate the direction of the forces related to volume expansion.



Figure 3-13: Photograph of a PAA film delaminated from the supporting silicon wafer. An area covered with aluminum, that was not submerged in the anodization bath, holds the PAA film by its edge.

of the film to the wafer, and of the reduction of contact surface between the PAA and the wafer as a result of the barrier layer inversion.

The top (electrolyte-facing) and bottom (wafer-facing) surfaces of a free-standing film were examined by SEM and AFM after its spontaneous detachment from the silicon wafer at the completion of the anodization (Fig. 3-14). The SEM images show little difference between the surfaces, indicating that the porous PAA structure is conserved across the entire film. The pores at the bottom surface are smaller, consistent with the presence of an inverted barrier layer. However, the AFM images show a dramatic difference between the two surfaces: The bottom surface of the PAA film is extremely flat around the pores, mirroring the flat surface of the silicon wafer it was attached to. The top surface displays a rough topography that resulted from the depressions on the surface at the end of the first anodization and from the etching action of the anodization solution. Free-standing PAA films have been used as masks in pattern-transfer processes, transferring the self-assembled nanoscale hexagonal ordering to substrates which lack the self-organization process.[82, 98–105] The extreme flatness of the bottom surface, and the ease of detachment from the wafer, make the free-standing PAA films thus obtained very attractive as contact masks for such nanoscale pattern-transfer processes.

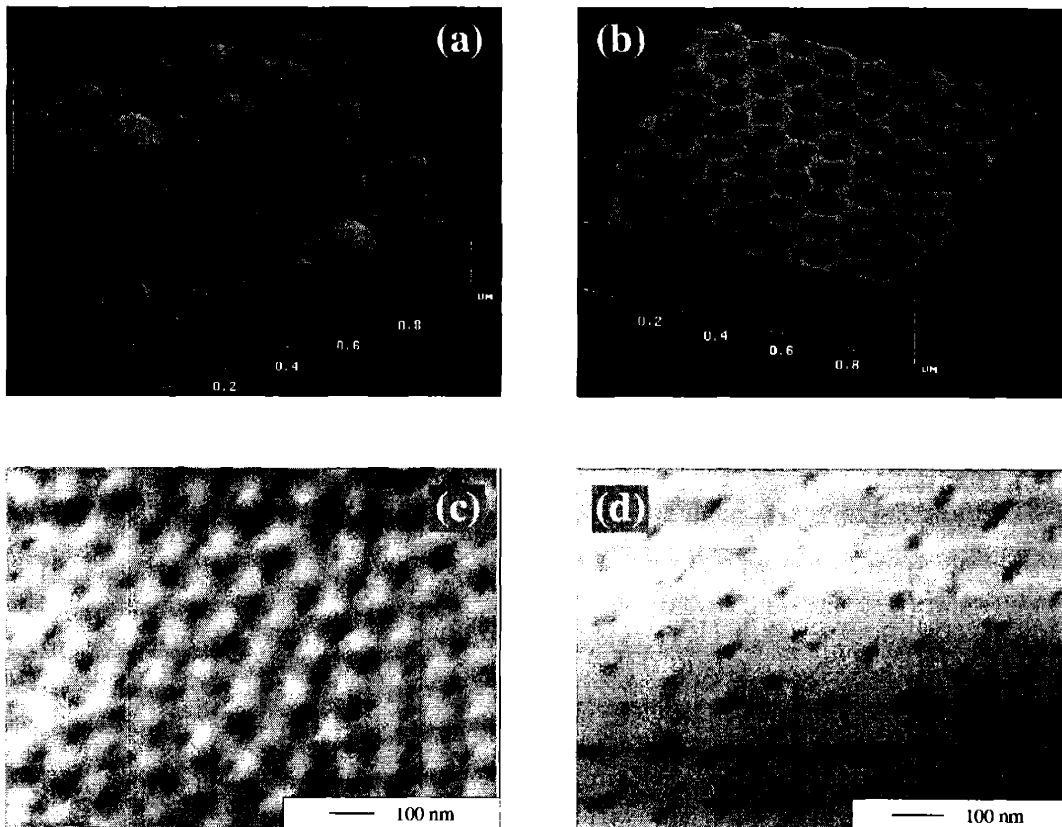


Figure 3-14: AFM micrographs of the surfaces of a PAA film that detached from the silicon substrate on which it was anodized [(a) electrolyte-facing, top surface; (b) wafer-facing, bottom surface], and SEM micrographs of the same surfaces [(c) top surface; (d) bottom surface].

3.3.3 Growth of PAA Films on an Optically Transparent Substrate

For optical applications of substrate-supported PAA films, the substrate and the anodic alumina should not be transparent to light in the relevant portion of the electromagnetic spectrum. PAA films show strong absorption in the far IR, but appear transparent to the naked eye. Thus, PAA films were prepared on microscope glass slides to evaluate their light transmission in the visible spectrum. Unfortunately, both the thermally evaporated aluminum and the PAA films displayed poor adhesion to the glass. A buffer layer of 10 nm titanium was employed on the glass to facilitate the formation of the structure, and reduce the formation of trapped aluminum islands at the end of the anodization. The transmission of the PAA-glass bilayer was measured in the range of 200–1800 nm (Cary 6000i UV-Vis-NIR spectrometer, Varian). The spectrum of the sample, presented in Fig. 3-15, shows that the film has a high optical transmission in the visible and near-IR regions. The reduction in transmission compared to the bare glass slide is mainly attributed to the featureless absorption of the titanium layer. Recently, transparent PAA films were prepared by others on ITO-coated glass slides.[106, 107]

3.4 The Effect of Thin Film Coatings on the Growth of Silicon Wafer-Supported Porous Anodic Alumina Films

In the previous section, the preparation of PAA film by the gas-phase deposition of aluminum on silicon wafers was described. While the method was successful in generating large area PAA films, these films possessed a normal barrier layer if the aluminum was not exhausted, and an inverted barrier layer if the aluminum was consumed. Furthermore, the PAA films detached from the silicon surface at the end of the anodization. These observations indicate that understanding the interface at

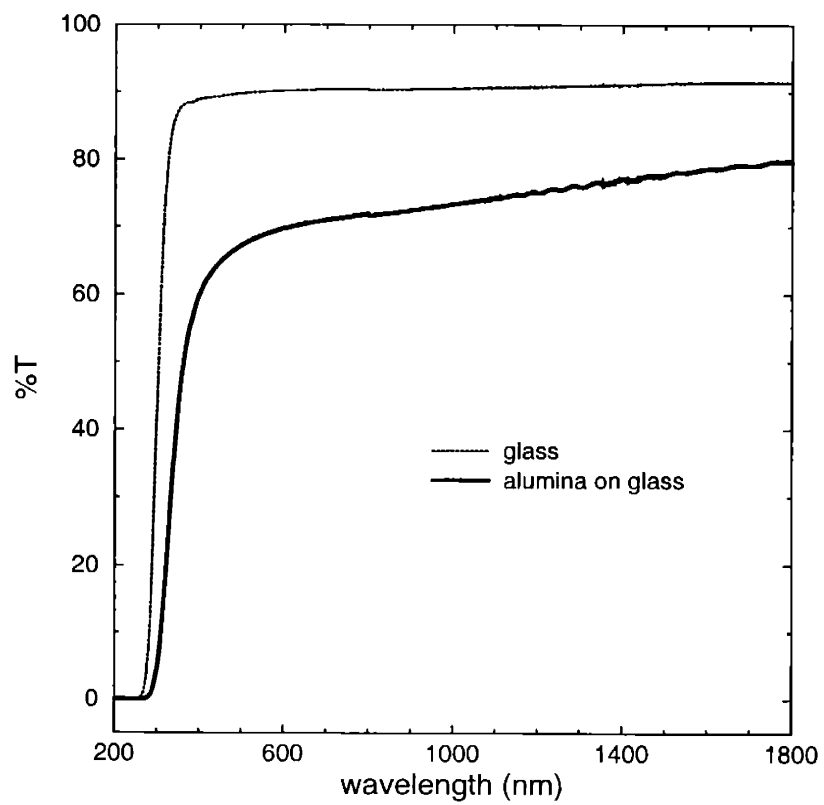


Figure 3-15: Comparison between the UV Vis-Near-IR transmission spectra of a PAA-glass bilayer slide and the transmission spectra of a bare glass slide.

the PAA–substrate boundary is critical to accomplish the substrate-supported PAA structure, since that interface has influence on both the adhesion of the PAA to the substrate and the morphology of the barrier layer.

To investigate the effect of the interface on the anodization process, silicon wafers with various thin film coatings were prepared. These wafers were then used as substrates for the thermal deposition of aluminum, and the aluminum films were anodized to completion. In the resulting structures, the thin films acted as interface buffer layers between the PAA and the wafer. By changing the composition of the coatings, the properties of the interface were varied. The interface film got exposed to the anodization conditions applied to the aluminum as the anodization front reached the bottom of the aluminum film. Time–current transients of the anodization process were recorded, and the data were correlated with the adhesion between the layers in the final structures and the morphology of the barrier layer.

3.4.1 Anodization Time–Current Transients

The time–current profiles of the anodization processes were manually recorded, or were recorded using a computer-interfaced digital multimeter and a custom-written recorder program. The current transients consist of three stages:

1. The initial stage, in which the voltage is ramped up, and the current peaks and then decreases as the aluminum oxide barrier layer is created on the surface of the sample. This phase lasts up to 60 seconds.
2. The steady state aluminum anodization, in which the current gradually increases as the ordering in the film is improved.
3. The final stage, in which the anodization front reaches the bottom of the aluminum layer, and signatures from the interface layers are observed.

The first two stages are very similar for all the films regardless of the nature of the interface layers, and are very similar to the current profile obtained during the

anodization of aluminum sheets. During these stages, only the aluminum film participates in the charge transfer between the sample and the electrolyte. The current transient during the last phase varies significantly from interface layer material to material. Roughly speaking, the interface layer materials could be divided into four categories according to their anodization response. Typical time–current transients of these categories are presented in Fig. 3-16.

The first category I includes all insulating interface layers. The example in Fig. 3-16 is from a silicon wafer coated by 520 nm of thermally grown silicon oxide. The current in this case runs from the leads to the electrolyte interface exclusively through the aluminum layer and not through the wafer. Thus, as the aluminum layer is consumed, the current decreases until the current flow stops. Since the anodization front is parallel to the PAA–electrolyte interface, unless care is taken in controlling the thickness variation across the sample, aluminum islands can be trapped in between the PAA and the SiO₂ layers, as they lose a conducting path to the anode lead.[108]

The second category II includes interface layer materials which also form porous anodic films under the anodization conditions of aluminum. The example in Fig. 3-16 is from a silicon wafer coated with 250 nm of sputter-deposited titanium (Applied Materials Endura System). Here, a decrease in the anodization current was observed and a new steady-state current was obtained, as the anodization front crossed from the aluminum layer to the titanium layer. The anodization of titanium is slower than the anodization of aluminum under the same voltage.[109] Therefore, the oxidation reactions at the titanium did not interfere with the anodization of the aluminum, even when the two processes occurred simultaneously (due to the aluminum layer thickness variations across the sample). However, if a titanium surface was exposed to the electrolyte during the first phase of the anodization, gas evolution and erosion of the titanium were observed to occur, interfering with the aluminum anodization. This is a surprising result. It demonstrates the capability of the nanoporous film and of the barrier layer to regulate the rates of ion transport in an electrochemical process, and to alter the reaction mechanism.

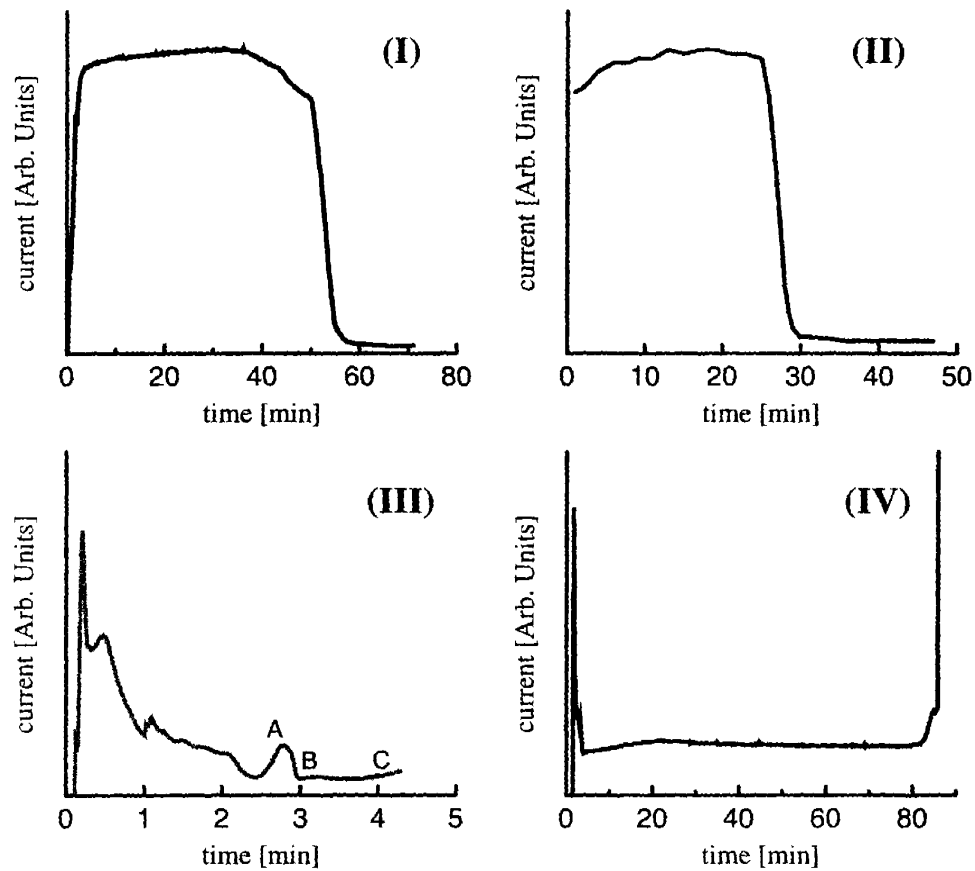


Figure 3-16: Time-current transients from anodization processes with different interface layers materials. (I) silicon oxide, (II) titanium, (III) *n*-type polysilicon, and (IV) platinum. The current (y-axis value) is proportional to the sample area, and the duration of the anodization is proportional to the aluminum layer thickness. The slope of the current drop in plots (I) and (II) is proportional to the thickness variation across the sample.

The third category III includes interface layer materials which oxidize under the anodization conditions of aluminum, yet form barrier layer-type oxides. The example in Fig. 3-16 is from a silicon wafer coated with 100 nm *n*-type polysilicon over an insulating layer of SiN_x (the aluminum in this sample was prepared by e-beam evaporation and was limited to 200 nm to obtain a uniform thickness). The current is observed to decrease at the end of the aluminum anodization, but then a peak is observed ('A' in plot), corresponding to the oxidation of the polysilicon layer. The second decrease in current ('B') indicates the formation of the barrier layer at the surface of the silicon. At this point the PAA film is observed to delaminate from the wafer, and the current increases again ('C') as a result of direct contact between the wafer and the electrolyte, leading to oxygen evolution.

The fourth category IV includes noble metals and metals that dissolve – but do not form anodic oxides – under the anodization conditions of aluminum. The example in Fig. 3-16 is from a wafer coated with 50 nm platinum over a 40 nm thick titanium adhesion layer. The current in this case is observed to increase sharply as the anodization front reaches the platinum film. Oxygen is generated at the metal surface, and the gas bubbles rupture the PAA film. These processes also hinder the anodization of aluminum from continuing in parallel. Thus, only small areas of fully anodized aluminum can be achieved with interface layers of this category, if there are thickness variations in the aluminum layer.

3.4.2 Adhesion Properties

One objective of adding an interface layer between the PAA film and the wafer is to control the adhesion between the layers of the structure. As was mentioned in Sect. 3.3, the use of bare silicon wafers leads to the formation of high-quality free-standing PAA films, since the adhesion is poor. The same was observed with polysilicon interface layers. In general, coatings of the first category showed good adhesion to the PAA film, as no anodic reactions could occur at the interface. The exception to the rule was glass microscope slides, which showed poor adhesion to both the aluminum film and the PAA film. However, the problem was fixed with the use of

a 20 nm thick titanium buffer layer on the glass. From the second category, only titanium was tested, and it resulted in a robust structure. Three materials tested from the third category (Si, polySi and Ag) lead to the detachment of the PAA film. A layer of 20 nm of silver was the most effective among the interface layers examined in causing the separation of the film, and adhered to the PAA stronger than to the wafer. The delamination mechanism probably involves structural changes at the interface due to the oxidation processes, which require a rearrangement of the atomic structure. However, there is no reason not to expect that some materials from this category will not cause delamination. Some members of the fourth category appear to have good adhesion properties towards the PAA film[88, 110], indicating that no structural changes occur at their interfaces. However, the evaluation of the robustness of the structure is difficult in this case, since the quality of the films depends very much on the precautions taken to prevent damage to the PAA from gas evolution.

3.4.3 Barrier Layer Morphology

Scanning electron microscopy (SEM) studies were carried out to analyze the structure of the barrier layers that were obtained by using wafers coated with different thin films. It was previously observed that the anodization of aluminum directly on a silicon wafer results in the creation of an inverted barrier layer.[84] It is expected that the barrier layer morphology will depend on the interface layer material composition: Since the materials at the interface have different anodization signatures (Sect. 3.4.1), each leads to a different sequence of anodic reactions and generates different PAA formations.

SEM cross section images of 4 types of PAA–substrate interfaces are shown in Fig. 3-17. The barrier layer formed at the interface with SiO₂ is seen to be thick (~40 nm), and differs from the barrier layer on aluminum substrates only in having a flat interface (instead of a wavy one) with the substrate. In some instances, the pore bottoms are approximately rectangular in cross section. Pyramidal aluminum islands trapped under the PAA film can be seen in between alumina cells (Fig. 3-17I). The barrier layer formed on bare silicon wafers has an inverted morphology (Fig. 3-

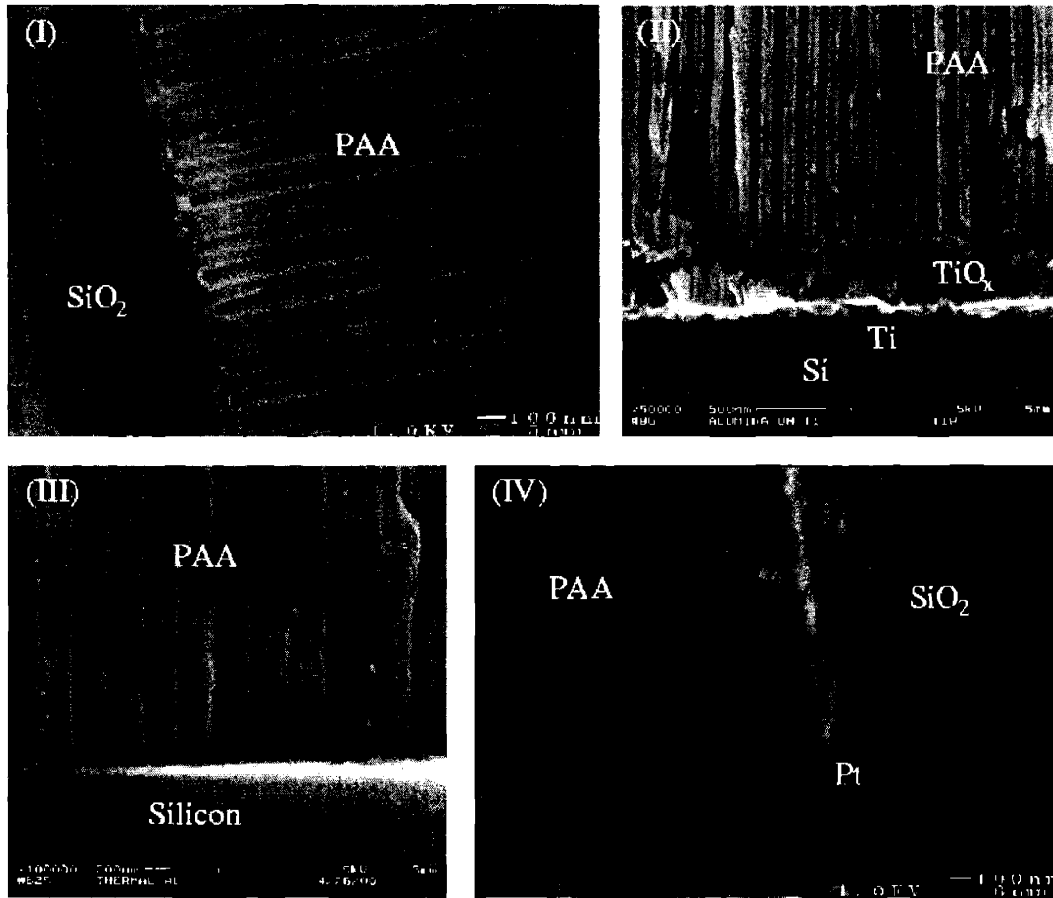


Figure 3-17: Cross section SEM images of the barrier layer region from PAA films on different interface layers materials. (I) silicon oxide, (II) titanium, (III) *n*-type silicon, and (IV) platinum.

17III). The mechanism of formation of this structure has been proposed in Sect. 3.3. Barrier layers over a surface of platinum were difficult to image by SEM, because of the large difference in brightness between the conducting metal and the insulating oxide layer (Fig. 3-17IV). It appears that some channels end in a thick barrier layer, separating the pore from the Pt film, while others lack a barrier layer. Less frequently, an intermediate structure is observed, in which the barrier layer at the bottom of the pore appeared to have a narrower channel across it, connecting the pore and the Pt film. These observations indicate that the anodic reactions at the platinum interface (most probably the generation of oxygen gas) damage and remove the barrier layer at the bottom of the channels. However, this occurs only at the channels located in the thinnest aluminum regions, whose bottoms reach the platinum surface first. The electrolysis at these locations thwarts the continuation of the anodization at other locations. Thus, pores at other locations just approaching the Pt film will retain their barrier layer, and pores at locations with thicker aluminum layers will even have aluminum, in addition to the barrier layer, between them and the platinum layer. More evidence for this was obtained by nanowire growth experiments (Sect. 3.5). Finally, PAA films on titanium coated substrates, in which the anodization continues into the titanium layer, display a barrier layer somewhat similar to the inverted barrier layer on silicon (Fig. 3-17II). The anodization slows down at the Al-Ti interface but does not stop. Field-enhanced oxide dissolution continues, and the barrier layer of the PAA films is thinner and less uniform than the one seen on silicon. As the anodization front crosses over to the titanium layer, a new barrier layer is formed between the titanium and the porous titania.

3.5 Fabrication of Nanowire Arrays in Silicon Wafer-Supported PAA films: Overcoming the Barrier Layer Challenge

PAA films were successfully prepared on the surface of silicon wafers with appropriate coatings (Sect. 3.4). These films could be fabricated on large areas, as the rigid substrate protected them from bending and cracking. The films showed a low degree of imperfections and high optical transparency in the visible–near IR spectrum. Therefore, the usage of these films as templates for nanoscale fabrication was investigated. In particular, preparing arrays of nanowires in physical contact with the substrate is desirable. Such a structure will enable, for instance, the incorporation of the nanowires in electrical circuits[111, 112], and could take advantage of the unique conduction properties of nanowires[113]. However, to generate such structures, one needs to be able to remove the barrier layer at the interface between the pores and the substrate, without removing the PAA film from the substrate, and without damaging the porous structure. This is one of the challenges that have significantly limited the use of nanowire arrays templated by PAA, although some techniques were developed to circumvent the problem.[84, 88, 90, 107]

As mentioned in the context of the analysis of the barrier layer morphology (Sect. 3.4.3), wafers coated with a platinum thin film were found to yield PAA films that lacked a barrier layer at the bottom of, at least, part of the channels. Since the platinum layer does not anodize, the layer serves as an electrical lead to the bottom of those channels in which the barrier layer is missing. Thus, the interface layer could be used as a working electrode for the electrochemical deposition from electrolytes in the PAA pores. The deposition process, templated by the walls of the PAA channels, will result in the formation of nanowires in the channels directly connected to the electrode. Furthermore, since deposition can occur only on bias surfaces, the growth of a nanowire will necessarily indicate that there is electrical continuity across the filled channel and between the filled channel and the platinum surface. Various

electroplating baths were used to deposit nanowires of different materials (Au, Ag, Bi, Cu, polypyrrole) in the pores of PAA films on Pt-coated wafers by standard direct current electrodeposition. The only precaution necessary was to make sure the electrolyte comes in contact with the working electrode only within the pores of the alumina. Figure 3-18(a) shows an SEM micrograph of the cross section of a PAA membrane on a Pt-coated wafer, in which some channels have been filled with bismuth nanowires by electrochemical deposition. The aspect ratio of these nanowires, 60-70 nm in diameter, is very high, exceeding 100. Aspect ratios exceeding 300 were achieved for thinner nanowires, 30 nm in diameter. The image in Fig. 3-18(a) was taken at the interface between a fully anodized region and a region in which the PAA pores have not yet reached the Pt surface. The image shows dense groups of continuous nanowires growing from the Pt layer toward the solution side of the PAA template. The density of the nanowires decreases sharply toward the top of the micrograph, as we approach the region where the aluminum was not fully anodized. There is also a large distribution of nanowire lengths within the groups of nanowires, indicating that the openings at the barrier layer are not of uniform size and quality. Figure 3-18(b) shows an SEM image of a gold nanowire array obtained by the electrochemical deposition of gold into the channels of a PAA template on a Pt-coated wafer. The image shows the Pt surface after the complete etching of the PAA membrane, which exposes the nanowires. In this image, a region of short nanowires can be identified. The nanorods did not shift from their original positions, nor lose their orientation, retaining the hexagonal arrangement of the pores of the template. Back scattering electron imaging and EDS analysis indicated that the nanowires were made of gold while the surrounding surface was made of Pt. Since the nanowires are the inverted image of their template, this finding indicates that the interface between the PAA and the Pt layers consists of non-interconnected pore openings.

The Pt-coated substrates demonstrated the ability to grow arrays of nanowires on the wafers. However, since it is not possible to anodize the aluminum layer deposited on Pt-coated wafers in a complete manner, a thick barrier layer remains over extensive areas of the sample, leading to a non-uniform nanowire density across the

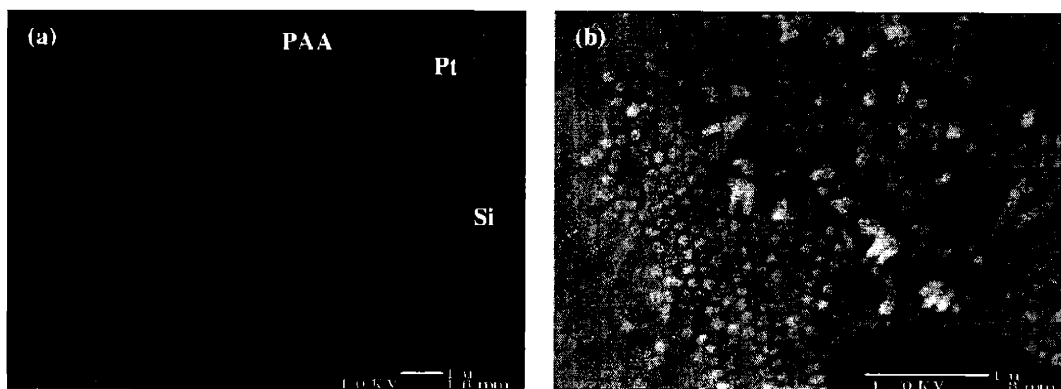


Figure 3-18: (a) Cross section SEM micrograph (back-scattering mode) of bismuth nanowire arrays grown on a Pt-coated silicon wafer. (b) Top view of gold nanowires grown on a Pt-coated silicon substrate after dissolution of the PAA template.

templates. To achieve a higher uniformity in the structure of the barrier layer and in the nanowire filling within a large area, the Ti-coated wafers are more appealing, since the anodization of the aluminum can be driven to completion on these substrates. In these samples most of the channels end in a barrier layer, but this barrier layer is thin. The titanium layer was oxidized under the operating conditions for Al anodization, forming a porous oxide coating[109]. Underneath this oxide, a low-resistance metallic titanium layer remained (Fig. 3-17II). The titanium was used to induce an electrochemical process at the interface between the substrate and the PAA for the purpose of removing the barrier layer. The process consisted of immersing the sample in a dilute potassium chloride electrolyte and cathodically polarizing the titanium layer for several minutes at -2.25 V *vs.* a platinum plate electrode. Under these conditions, hydroxide ions were produced at the surface of the titanium, locally increasing the pH. Since dissolution of the PAA membrane is enhanced at $\text{pH} > 8$ [114], the process led to the thinning of the alumina. Figure 3-19 shows a cross sectional view of the PAA–Ti interface after barrier layer dissolution. It can be noticed that most channels lack a barrier layer, ending in a partially or completely open pore. Hints of the inverted barrier layer can be seen in some of the channel ends. When the cathodic polarization was applied to a Pt-coated substrate, it re-

sulted in a current density higher by an order of magnitude, and defects soon became visible in the film. A cross sectional SEM inspection (Fig. 3-20) revealed that these defects were localized at the substrate-PAA interface as cave-like structures, while the solution-PAA interface remained flat and undamaged. These observations imply that localized electrochemical reactions at the substrate-electrolyte interface led to the selective etching of the barrier layer without the disruption of the porous alumina structure. The selective etching of the barrier layer is a unique quality of the presented process[115, 116], which distinguishes it from other attempts to template the electrodeposition of nanowires on substrates using PAA films.[88, 107] These other works failed to remove the barrier layer without causing significant alterations to the porous structure. The barrier layer-depleted PAA films on the Ti-coated wafers were used as templates for nanowire growth by electrochemical deposition. Figure 3-21 shows a cross section of such a template after being overfilled with bismuth telluride (prepared in collaboration with Dr. M. A. Ryan and Dr. A. Borshchevsky from Jet Propulsion Laboratory, Pasadena CA).[117] In contrast to the Pt-coated samples in which the density of nanowires varied significantly across the sample, here the growth of the nanowires was uniform over the entire area of the sample ($\sim 0.5 \text{ cm}^2$).

The substrate-supported PAA could, in principle, serve as a template for nanowire synthesis via other growth techniques, as long as the substrate material does not interfere with the growth process and it is not damaged by it. Melt injection[118], sol-gel processing, chemical vapor deposition, and vapor-liquid-solid growth[119] are examples of possible methods for nanowire synthesis that can be coupled with the substrate-supported templates. The use of these templates in melt injection was demonstrated in the synthesis of bismuth nanowires. Since this technique results in a large excess of bismuth on top of the template, the pores were imaged by separating the PAA film from the substrate, and then imaging its wafer-facing side. Figure 3-22 shows an SEM image of the surface showing bismuth nanowires in channels that were filled from end to end ($\sim 10\%$ of the channels).

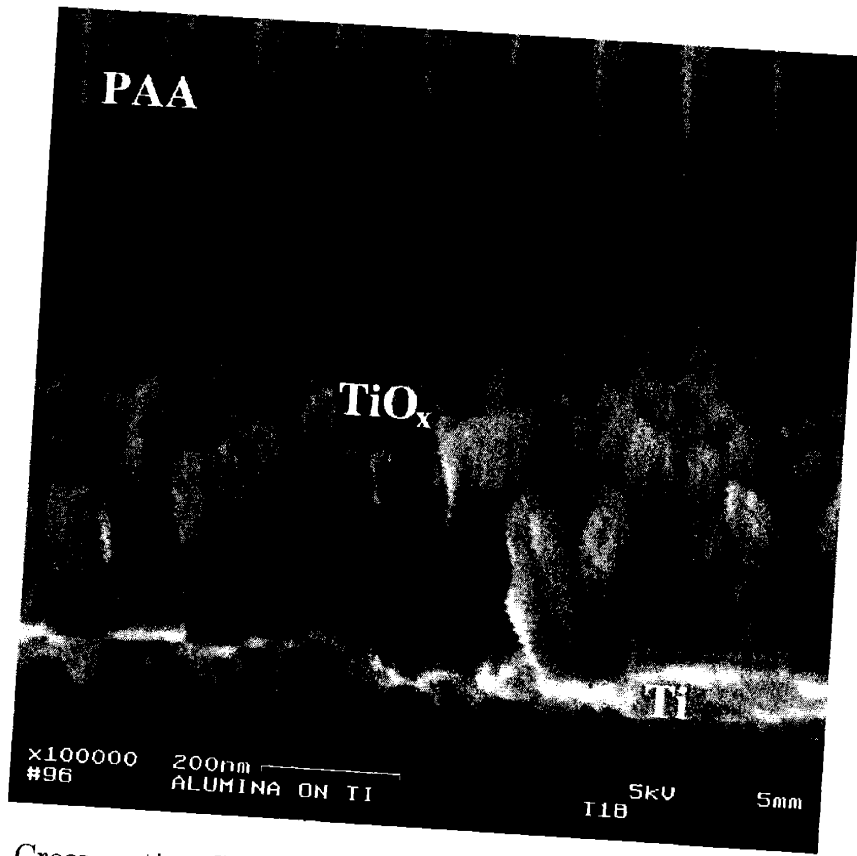


Figure 3-19: Cross section SEM micrograph of the interface between the PAA film and the titanium/titanium-oxide layer after an anodization on a Ti-coated silicon wafer. The sample was then subjected to the pore widening and the electrochemical barrier layer removal processes described in the text. From top to bottom, we observe the ordered alumina channels, oxidized titanium pillars, and a titanium film coating the silicon surface.

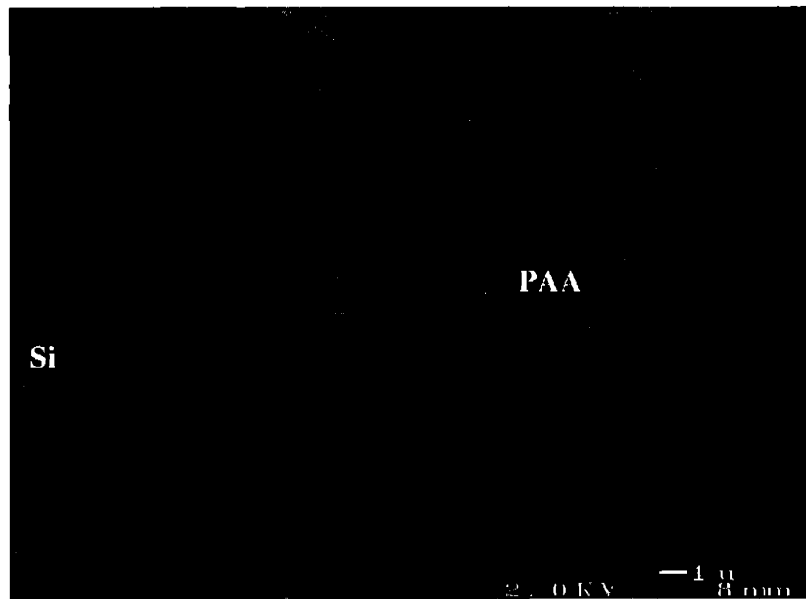


Figure 3-20: Cross section SEM micrograph of the PAA and of the wafer (on the left) after an anodization on a Pt-coated silicon wafer. The sample was subjected to the electrochemical barrier layer removal process for a prolonged period of time. The process caused damage in the form of gaps in the PAA structure starting at the interface with the substrate and extending up to $\sim 5 \mu\text{m}$ into the PAA layer. The undamaged, external surface of the PAA is seen on the right.

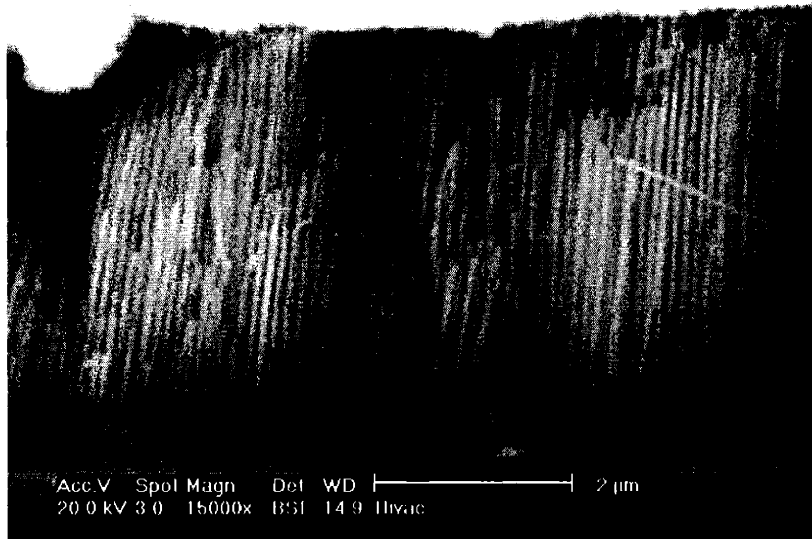


Figure 3-21: Cross section SEM micrograph of bismuth telluride nanowires grown in a barrier layer-depleted PAA template on a Ti-coated wafer.[115]

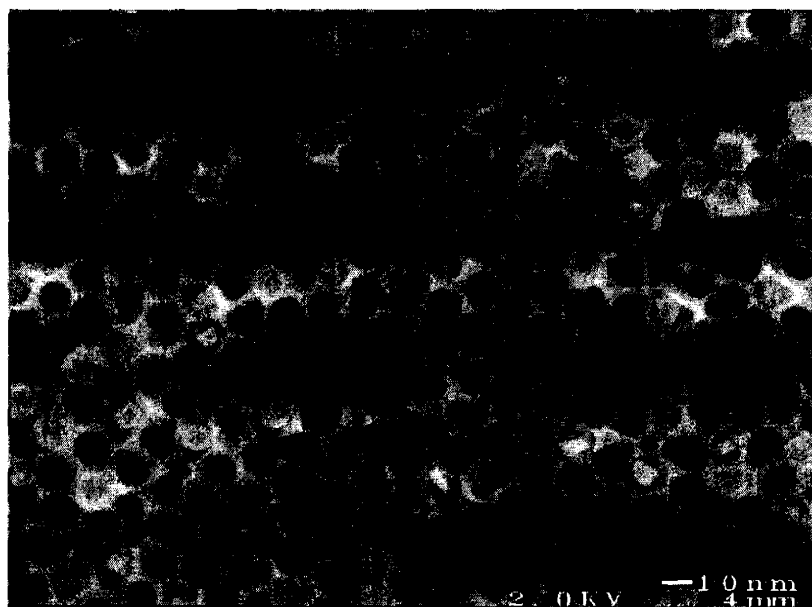


Figure 3-22: SEM image of a bismuth-filled PAA film obtained by the pressure injection technique. The dark circles denote unfilled pores and the light pores are filled with bismuth.

3.6 Patterned Porous Anodic Alumina Films

Due to the rigidity of the substrate, the samples can be manipulated considerably without the danger of cracking, a common problem encountered when processing conventional PAA films (free standing or on aluminum sheets). As an example of the versatility of PAA films prepared by the method reported here, a new method for patterning PAA is presented.

Previously, the patterning of PAA films was achieved by etching regions of the anodic alumina film after anodization.[120] Since porous surfaces complicate the processes of spinning on the photoresist and of its removal, a pattern transfer layer covering the PAA was used.[120] For PAA films on silicon wafers, in addition to this post-anodization selective-etch method, patterned PAA films were obtained by employing a patterned substrate. On a Ti-coated silicon substrate, an array of lines of silicon oxide was deposited by sputtering. The trenches between the lines were 2.5 mm long, 10–250 μm wide, and 500 nm deep. Aluminum was evaporated on the patterned substrate, electrochemically polished and anodized. Since the entire substrate was originally coated with a continuous conducting layer of titanium, the patterned aluminum structures did not need to be continuous. Figure 3-23 shows PAA lines obtained by this patterning method in the trenches between slabs of silicon oxide. Detailed examination of the cross section of the structures shows that due to the poor step coverage of the aluminum deposition, weak links were formed between the sections of the aluminum film in the trenches and those on top of the silicon oxide structures (Fig. 3-23b). During the subsequent anodizations and etchings, the connecting necks were broken or dissolved, leaving PAA structures mostly within the trenches (compare Figs. 3-23b and 3-23c). Since the side walls of the aluminum line were exposed to the electrolyte, pores grew simultaneously, vertically from the top surface down and horizontally from the side walls inward. Thus, only pores within a region along the center of the PAA line actually reached the substrate (Fig. 3-23e). A barrier layer grew diagonally along the top angle-bisectors, where pores from the top and from the side surfaces met (Fig. 3-23f). Non-planar PAA films such as this

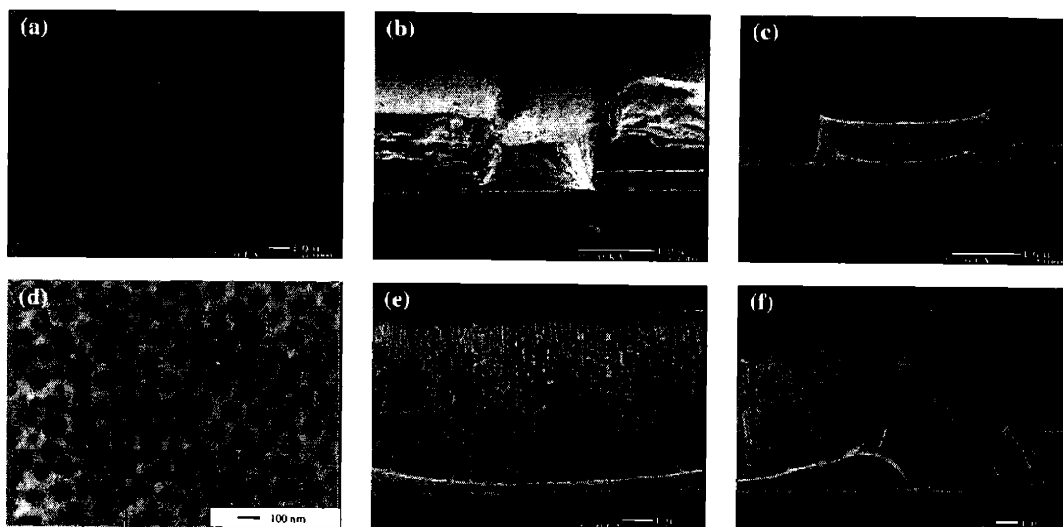


Figure 3-23: Patterned lines of PAA on a Ti-coated, SiO₂-patterned wafer [(a) top view of a PAA line between two slabs of SiO₂; (b) side view before anodization; (c) side view after anodization; (d) high magnification of top view of the PAA line shown in (a); (e) and (f) high magnification cross sectional views of the PAA line shown in (c)].[115]

have been rarely investigated.[121] Their growth on a patterned substrate greatly facilitates their design and preparation. Non-planar PAA structures are of interest as the orientation of the channels (or of the nanowires) can be engineered to change continuously (as in curved films) or abruptly (as in films with kinks). However, it was found that some formations are not easily achieved, due to factors such as the internal strain in the growing film, and the geometric dependence of the pore density on curvature and film thickness. Non-planar porous anodic alumina structures are an exciting subject for further exploration.

The process described here also offers a means for the fabrication of several new “flavors” of arrays of nanowires in PAA templates that were impossible or difficult to prepare with the previously available technology. Primarily, the location of the growth of nanowires can be prescribed by the design of the substrate, particularly by the patterning of conducting and insulating regions on the substrate. Furthermore, the patterns can be designed so that areas on the wafer can be biased independently

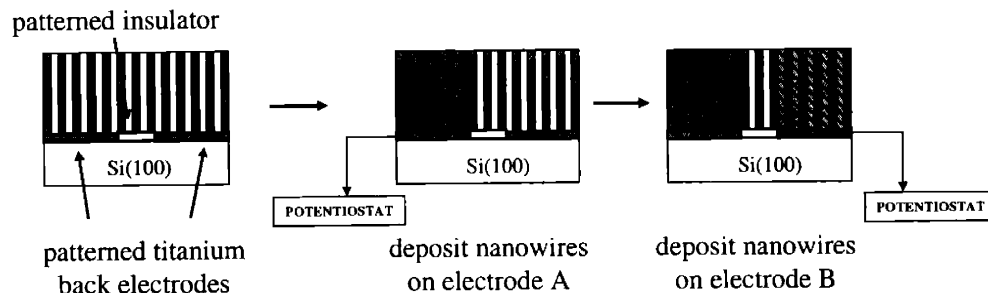


Figure 3-24: Schematic representation of the use of conducting and insulating pads on the substrate to electrodeposit nanowire arrays of different compositions on the same PAA template.

(Fig. 3-24). This design will allow the fabrication of several arrays of nanowires on a single PAA film, each array being distinct in terms of its composition (or its composition profile along the main nanowire axis[122]). Such a 'super-array' is well suited for sensing applications of nanowires[122]. In addition, this process offers a means of generating nanowires of different lengths within the same template, dictated either by the topography of a patterned substrate or by the thickness profile of the deposited aluminum film, and possibly using planarization processes.

3.7 Other Modifications: Porous Anodic Alumina Films on Patterned Aluminum Supports

Conventionally, PAA films are grown on aluminum sheets, as detailed in Sect. 3.1.2 and depicted in Fig. 3-3. While the PAA films prepared on rigid substrates have great advantages over those made on aluminum sheets, at the present time, the latter are still more convenient when thick PAA films are required (for example, to template nanowires longer than 10 μm). Thus, improvements made in the fabrication of PAA films on aluminum sheets are still of value.

In order to grow nanowires by electrochemical deposition, through-channel PAA

films are necessary. These can be prepared by the removal of both the aluminum substrate and the barrier layer by a chemical etch (Sect. 3.1.2). However, removing the aluminum substrate leaves a free-standing film that is difficult to manipulate because of its small thickness and its low rigidity. As was shown in Sect. 3.5, growing the PAA on a rigid substrate can alleviate this problem. Alternatively, patterned etching of the aluminum substrate could serve as a way to balance the need for structural rigidity with the need to expose the pore ends at the barrier layer side.[123]

The back side of aluminum sheets was patterned by hand with an insulating coating (lacquer or Crystalbond) to define areas to be protected from contacting the etching solution. When a saturated HgCl_2 solution was used to etch the aluminum foil, the coating protected the covered areas from oxidation by the Hg^{+2} ions. However, it was not possible to remove all the mercury liquid that was formed in the reaction. Mercury serves as a catalyst for the oxidation of aluminum even in air[124], and thus the patterned coating fails to protect the aluminum. In addition, the traces of mercury on the sample make this process a severe health and environmental hazard. Other commonly used aluminum etching agents, such as the PAN etch solution (a mixture of phosphoric, acetic and nitric acids), are also potent aluminum oxide etchants. Their activity depends on their ability to remove the protective oxide coating from the aluminum surface. Their use is not adequate for the purpose of removing the aluminum substrate, as they primarily dissolve the PAA film. Copper chloride (CuCl_2) is a suitable aluminum reducing agent, that does not react with aluminum oxide. Selective removal of aluminum was achieved in a solution of 20 vol% HCl (assay: 37%) and 0.1 M CuCl_2 . The native oxide on the aluminum was scratched away in order to initiate the reaction. The copper film generated on the aluminum surfaces by the redox reaction was removed by mechanical agitation. No reactivity of the solution toward the protective coatings or the coated surfaces was detected, except for an undercut formed by lateral etching, as expected from an isotropic etch process. Figure 3-25 shows photographs of PAA films on patterned-etched Al substrates obtained by this method. In one of the films, bismuth nanowires were grown using a gold film back-electrode.

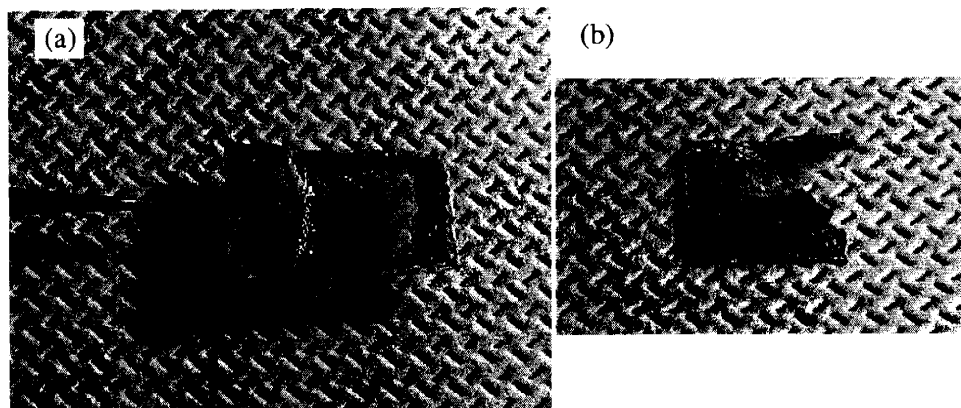


Figure 3-25: Photographs of PAA films on aluminum sheets that were subjected to a selective-area CuCl_2 etch. (a) A transparent porous alumina film supported by an aluminum frame. (b) An aluminum-supported porous alumina film with an e-beam deposited gold back-electrode and electrodeposited bismuth nanowires (dark area).

3.8 Summary and Future Directions

In this chapter, work leading to the development of a new process for the preparation of PAA templates and nanowire arrays has been presented. Samples produced by this process are superior in terms of their uniformity, robustness and effective area. This process is expected to greatly facilitate the development of nanowire-based electronic and optical devices.

Near-future developments on the fabrication of substrate-supported membranes will probably focus on the improvement of the ordering and diameter distribution of the pores. Since the current process utilized aluminum films of limited thickness, not enough material is available for the self-ordering process of the hexagonal pore lattice to anneal defects and to reach a perfectly-ordered structure. A process for the transfer of thick aluminum layers to the substrate is desirable, as it will allow for both the improvement of the pore ordering and the fabrication of longer nanowires. Pore ordering is also attainable through a well-established process of imprint-lithography.[79, 90, 125]. By pressing a stamp with patterned protrusions in a hexagonal lattice arrangement against the aluminum film surface, ordered depres-

sions are formed on the film surface that serve as nucleation points for the pores. Thus, a perfectly ordered pore array is formed already at the initial moments of anodization, regardless of the thickness of the aluminum layer. Additionally, by using stamps with patterns of suitable (non-hexagonal) lattice geometries, pores can be ordered into square or rectangular lattices.[126]

In chapter 3.6, it was proposed that a patterned conducting interface layer on the substrate could be used to regulate the growth of the nanowires across the substrate, for example, to control the composition of the nanowires by their location. Attempts to realize this idea have failed so far. It was realized from the experiments, however, that the non-planarity of the surfaces of the patterned substrates used was responsible for the failure of the process. The aluminum layer could not be deposited onto the non-planar substrates without the formation of voids at the step edges of the pattern back-electrodes. During the anodization, electrolyte leakage through the voids allowed for competing anodic reaction to occur and to corrupt the PAA film. The damaged PAA films were not appropriate for electrochemical growth of nanowires. There is a need therefore to develop a method to prepare substrates with patterned thick (≈ 250 nm) conducting films and planar surfaces.

Porous anodic alumina membranes could be of use in an array of emerging application, such as chemical and biological sensors, microfluidic and lab-on-chip devices, controlled-release systems, photonic and MEMS devices. As we improve our capabilities to make membranes of arbitrary shape, or on an array of substrates (i.e. plastics, living tissue), and to grow arrays of nanowires by-design, more powerful devices will be within reach.

Chapter 4

Bismuth, Antimony, and Bismuth-Antimony Nanowire Arrays: Electrochemical Synthesis, Structural Characterization and Electrical Properties

4.1 Background

Bismuth-Antimony ($\text{Bi}_{1-x}\text{Sb}_x$) alloys in bulk form show a very rich electronic behavior, and can be tuned to be semimetals, direct or indirect bandgap semiconductors, depending on the antimony mole fraction, x . [27] From the perspective of thermoelectricity, $\text{Bi}_{1-x}\text{Sb}_x$ alloys display their best figure-of-merit ZT at low temperatures (*circa* 77 K); and for these temperatures their ZT values are among the highest measured so far. [5] Furthermore, theoretical studies of low dimensional systems for thermoelectric applications have predicted an enhancement in ZT in Bi [16, 127] and $\text{Bi}_{1-x}\text{Sb}_x$ nanowires [56] as the wire diameter, composition, and carrier density are optimized (see Chap. 2).

The fabrication of bismuth nanowires has been demonstrated by various methods[15, 64, 128, 129], and the study of their transport properties is an active research area.[15, 130, 131] Bismuth nanowires have been prepared by electrochemical deposition into the channels of polymeric membranes[129, 132]. These nanowires, however, were of large diameter (> 95 nm), and were polycrystalline. A pressure-injection technique[64, 128], in which anodic alumina templates were infiltrated with liquid bismuth at high pressures, was used to fabricate arrays of single-crystal bismuth nanowires of smaller diameters (> 30 nm). Due to the non-wetting properties of liquid bismuth on alumina, the applied pressure scales as the inverse of the pore diameter, and as the diameter is decreased, the portion of filled pores – the filling factor – decreases rapidly. Since the anodic alumina channels are all parallel to each other, it was possible to identify by x-ray diffraction with respect to the normal to the film, that the nanowires show a common crystallographic orientation along their main axis. The nanowires were oriented with the (001), (012), or (101) planes perpendicular to their main axis, depending on nanowire diameter, and preparation conditions. Smaller diameter nanowires, down to 7 nm, were also attainable by impregnation of the anodic alumina templates with bismuth vapors in vacuum and their solidification in the channels under a temperature gradient.[15]

It should be noted that bismuth nanowires have not been fabricated by methods which do not make use of templates, such as the vapor-liquid-solid mechanism, or solvothermal processes. This is due to the low melting point of bismuth, and its high tendency to form oxides. Recently, a low yield solvothermal process for bismuth nanowire synthesis was described.[133]

The synthesis of Bi-Sb alloy nanowires has only recently been attempted[65, 134, 135], in response to the theoretical studies.

In this chapter, the synthesis of Bi-Sb nanowires via electrochemical methods is revisited, choosing porous anodic alumina substrates as the templating matrix. New electrolytes are proposed for this purpose, circumventing solubility problems often observed with these elements. Extensive efforts were made to improve the crystallinity of the samples. The electrical properties of the arrays were also investigated.

4.2 Electrochemical Deposition in Porous Anodic Alumina Templates – General Comments

Porous anodic alumina (PAA) films were chosen as the template matrix for the synthesis of nanowires in this work. The matrix is required to be electrically insulating, and to have a low thermal conductivity. The advantages of the PAA films over other common templates, such as track-etch polymeric membranes, block copolymer templates, porous silicon, and zeolites, are:

1. Wide range of nanoscale pore diameters (7–200 nm).
2. Monodispersity of the pore diameters.
3. Straight channels with high aspect ratios (commonly ~ 100).
4. Very high density of pores (10^{10} cm^{-2}).
5. Thermal stability (first phase change occurs at 820°C).[136]
6. Can be removed by etching in acid or base solutions.[137]
7. Stable in organic solvents.

Electrochemical deposition was chosen as the synthesis method for its numerous advantages:

1. A relatively cheap, low-temperature technique.
2. It can be used on a variety of materials.
3. The nanowires are necessarily in electrical contact with the working electrode, and show electrical continuity.
4. The pore diameter does not affect the filling factor.
5. Oxide formation is usually prevented by the applied potential (in cathodic deposition).

The electrochemical synthesis of nanowires is carried out as depicted in Fig. 4-1: The working, counter, and reference electrodes were immersed in the electrolytic bath. The working electrode consists of the PAA film with through-channels. One face of the PAA film is coated by a conducting film, that serves as the back electrode from which the deposit begins to grow. This film is protected by an insulator, which prevents direct contact between the conducting electrode and the bulk of the electrolyte solution (to avoid electroplating outside the pores). The other face of the PAA film is wetted by the electrolyte, and the channels get filled with electrolyte (for small diameter pores, sonication might be necessary to remove air from the channels). The counter electrode was a mesh of platinum wire (AlfaAesar). The reference electrode was a saturated calomel electrode (SCE; Aldrich). The three electrodes were hooked to a potentiostat (Gamry Instruments, model PC4-300, operating with VFP600 and PHE200 software packages).¹

The back electrode on the PAA film (labeled “metal” on the right hand sketch in Fig. 4-1) was composed of a 10 nm chromium layer and a 200 nm gold layer deposited via e-beam evaporation. For PAA films with large pore diameters (Anodisc 13, Whatman International Ltd., nominal pore diameter: 200 nm), the evaporated films were not thick enough to seal the pore openings. Thus, a micron thick copper film was electrochemically deposited over the evaporated films in the galvanostatic mode of the potentiostat (Technic-Copper-U electroplating solution, 1–2 mA, 1–3 hrs).

Insulation of the back electrode from the bulk electrolyte was achieved by the application of lacquer on the conducting surfaces of the working electrode (labeled “insulator” in Fig. 4-1). This method was seemingly effective and cheap. However,

¹During the first year and a half, the electrochemical nanowire synthesis work was carried out with a home-built feedback-controlled voltage/current source (voltage resolution ± 10 mV) provided by Mr. S. Rabin. Since the latter use of a commercial potentiostat with electrochemical capabilities (resolution ± 0.1 mV; cyclic voltammetry scans; noise filtering; real-time display) led to the fabrication of nanowire arrays with an improved crystallinity and a higher filling factor, through the more accurate determination and control of process parameters, only the latter results are reported. Nonetheless, the home-built source was constructive in the process of testing and resolving many of the chemical and engineering questions associated with the electroplating of bismuth nanowires.

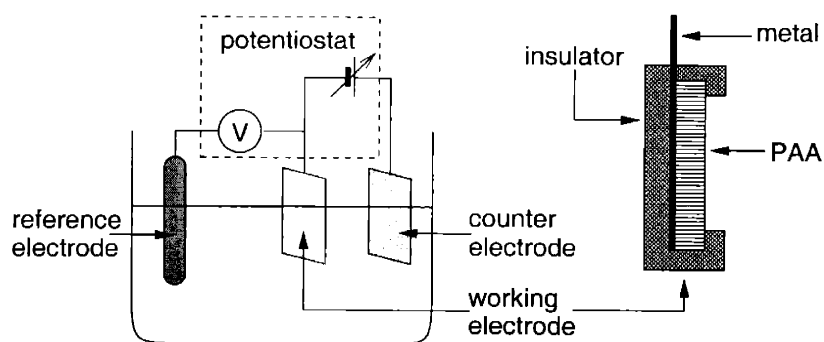


Figure 4-1: General setup for the electroplating of nanowires in PAA films. On the right, a detailed drawing of the cross section of the working electrode is shown.

multiple layers and long drying times were required, and the coatings gradually degraded during the deposition. When non-aqueous electrolytes were employed, this type of coating could not be used, since the solvent quickly dissolved the coating. No other fast drying and removable sealant was found appropriate. Thus, to improve the insulation and make it indiscriminating toward the solvent used in the electroplating process, an alternative method was followed: A deposition cell was designed, in which the porous face of the working electrode is pressed against an opening in the bottom of the electrolyte-containing compartment. The structure of the cell is presented in Fig. 4-2. The cell was machined out of Teflon. A chemically resistant rubber (silicone rubber for aqueous electrolytes, neoprene for DMSO-based electrolytes) was used to make the sample-Teflon interface leak-proof, and to prevent the cracking of the template by the tightening pressure applied on it. The conducting sample holder and tightening screw were used to lead current from the working electrode. Separate cells, however, were necessary to accommodate samples of different sizes, and the samples were required to be planar. This approach was effective in preventing electrolyte leakage and deposition on the back electrode. As will be shown later, usage of the Teflon cell also helped in improving the crystal structure of the deposit.

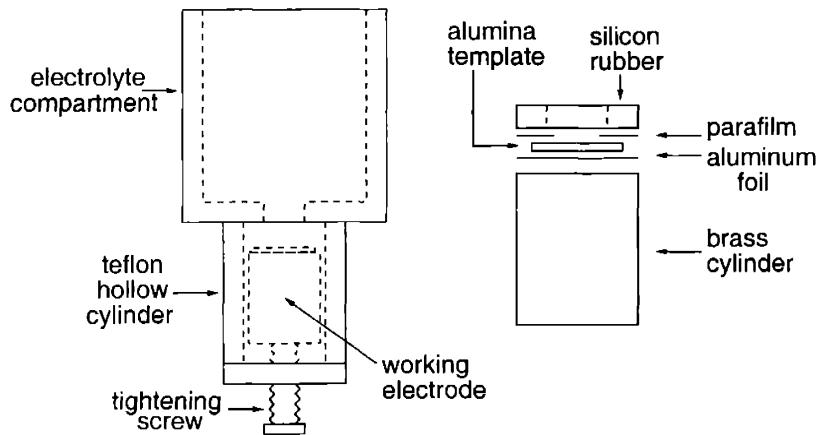
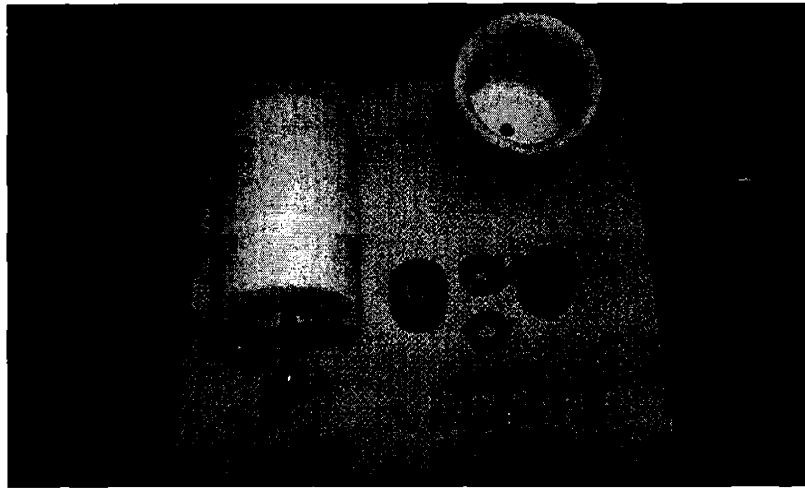


Figure 4-2: Schematics and photograph of the components of the custom-designed electroplating setup. On the right, a detailed drawing of the working electrode components is shown.

4.3 Electrochemical Deposition of Bismuth Nanowires in Porous Anodic Alumina Templates

The electrochemical deposition of bismuth nanowires in PAA templates was not reported until recently, perhaps due to chemical compatibility issues arising from the low solubility of bismuth salts in aqueous solutions. Only the nitrate and the perchlorate bismuth salts are commonly used in electroplating baths.[138] Furthermore, the solubility of the bismuth salts is highly dependent on the pH of the solution. As the pH is increased, the bismuth salt hydrolyzes, and a basic salts (the oxy- or hydroxy-derivatives) precipitate. Thus, electroplating solutions are available only at very acidic pH. Examples include a $\text{Bi}_2\text{O}_3/\text{HClO}_4$ bath[139], a $\text{Bi}(\text{OAc})/\text{acetic acid}$ bath[140], a $\text{Bi}(\text{NO}_3)_3 \cdot 5\text{H}_2\text{O}/\text{tartaric acid}/\text{nitric acid}$ bath[129], and a $\text{BiCl}_3/\text{HCl}/\text{NaCl}$ bath[141]. On the other hand, PAA films are also sensitive to pH. PAA films are etched in both acidic and basic media (a property that is used to release the nanowires from the PAA template post-deposition). Studies on the etch rate of PAA films in HCl and NaOH solutions of various pH values concluded that the stability window of PAA is limited in the pH range from 5 to 9 (See Fig. 4-3). It is therefore expected that the bismuth plating baths will erode the PAA template. Indeed, pore widening was observed when anodic templates were soaked in a nitric-acid based bath for several hours. Moreover, the $\text{BiCl}_3/\text{HCl}/\text{NaCl}$ bath promoted a redox reaction, leading to the dissolution of aluminum metal (that served as support for the PAA film) and the electroless deposition of dendritic, nano-structured, black bismuth.

To satisfy both the requirement of high Bi^{3+} ion solubility and the narrow pH window of PAA stability, a new aqueous electrolyte solution was formulated for this work. The electrolyte was to contain a chelating ligand to stabilize the solvated form of the cation, yet the amount of additives was kept as low as possible to reduce the possibility of contamination of the deposit. Additionally, additives with a strong interaction with metallic surfaces were to be avoided. Adsorption and desorption of such additives affect the diffusion rates of the cations to nucleation and growth sites. In general, such additives promote finely polycrystalline smooth deposits. The

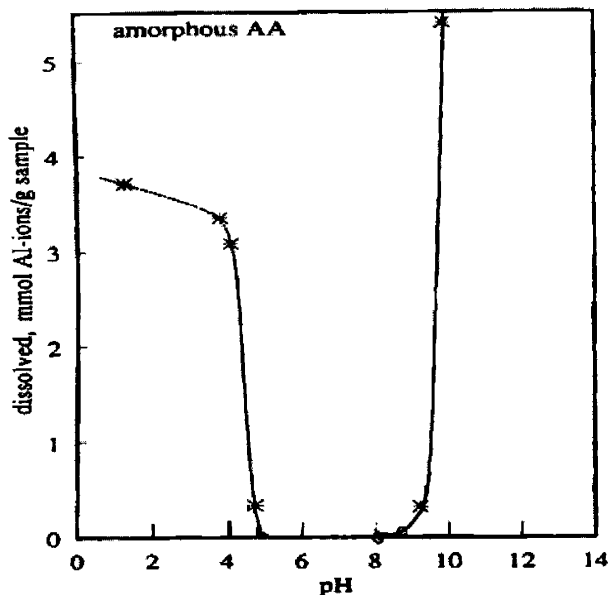


Figure 4-3: Dissolution rate of porous anodic alumina films as a function of pH in HCl and NaOH solutions. Data from Paterson *et al.*[137]

electrolyte developed in this work contained 40 mM of $\text{Bi}(\text{NO}_3)_3 \cdot 5\text{H}_2\text{O}$, a bismuth salt with relatively high solubility, and 70 mM ethylenediaminetetraacetic acid (EDTA), an excellent metal ion chelate. Upon vigorous stirring or sonication, a clear solution is obtained with a pH of 6. To improve the crystallinity of the deposit, this solution was prepared with a 1 M KNO_3 supporting electrolyte (See Sect. 4.6).

Cyclic voltammetry (CV) data of three bismuth electrolytes with different compositions are shown in Fig. 4-4. The working electrode was an HNO_3 -treated platinum sheet. A freshly HNO_3 -etched bismuth rod was used as a quasi-reference electrode, since chloride ions from the SCE were found to interfere with the voltage reading in the EDTA-containing electrolyte. The positive peaks correspond to reduction waves (bismuth metal deposition), while the negative peaks correspond to oxidation waves (bismuth metal dissolution and oxidation of aqueous species). The shape of the voltammetric curve is a result of the combination of the rates of the electron-transfer reactions at the electrode interface and the rates of ion mass-transport in the solution. A comparison between the CV plots shows a shift of approximately -250 mV in the

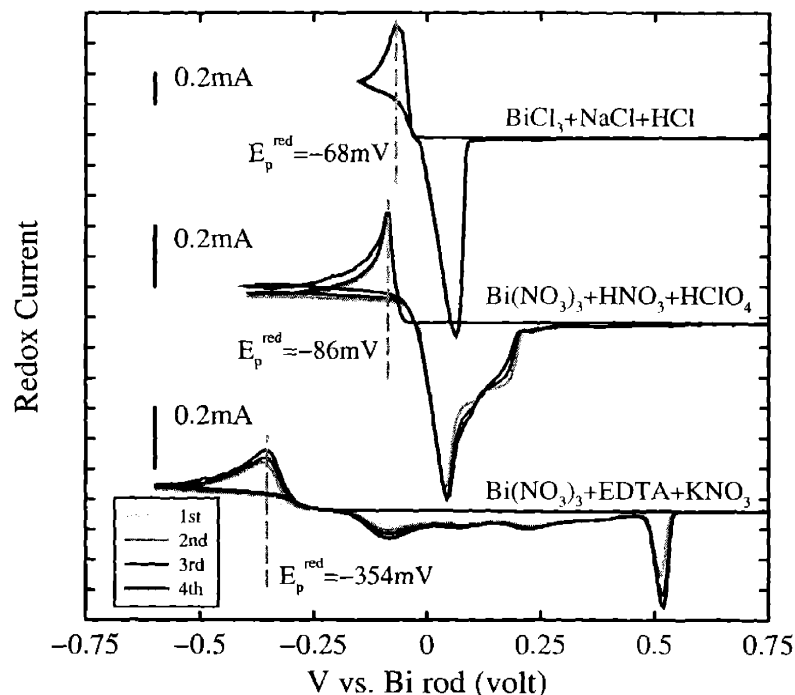


Figure 4-4: Cyclic voltammograms of bismuth electrolytes. Scans began at +1.0 volt, at 50 mV/sec. The first four cycles were plotted for each bath (see legends). The sets were offset along the y-axis for clarity.

reduction potential of bismuth in the EDTA-containing electrolyte. The additional EDTA-Bi⁺³ binding energy is expected to cause such a shift in the equilibrium potential. Plating at a more negative potential might have a detrimental effect on the quality of the deposit, as more impurities are expected to be incorporated.

4.4 Electrochemical Deposition of Antimony Nanowires in Porous Anodic Alumina Templates

The synthesis of antimony and bismuth-antimony nanowires via physical methods has been explored less compared to that of bismuth nanowires. The melting point of antimony is significantly higher than that of bismuth (630.76°C vs. 271.44°C), the vapor pressures of the two elements are not similar, and there is a large temperature differ-

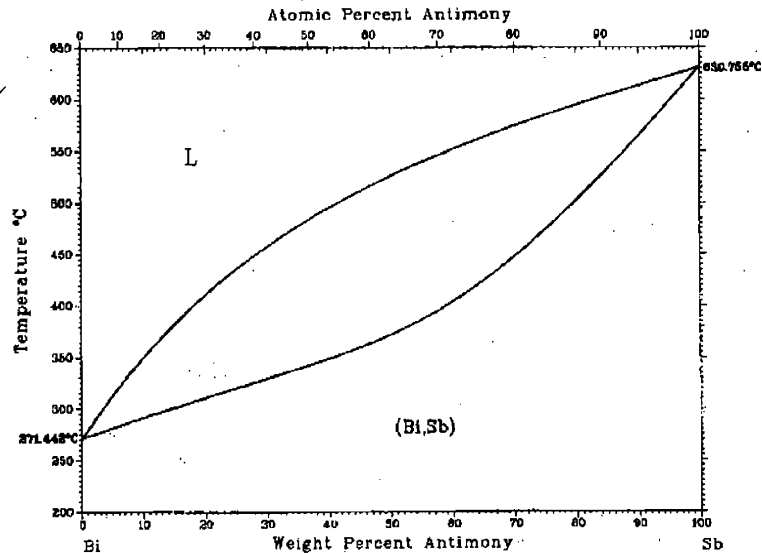


Figure 4-5: The bismuth-antimony binary alloy phase diagram. The large gap between the calculated liquidus and solidus curves is apparent.[142]

ence between the solidus and liquidus lines in the Bi-Sb phase diagram (Fig. 4-5.[142]) The latter leads to macroscopic segregation of the elements in the growing crystal and to crystal inhomogeneities resulting from constitutional supercooling. Antimony nanowires were synthesized via the gas-phase method[143] and bismuth-rich $\text{Bi}_{1-x}\text{Sb}_x$ nanowires were synthesized by pressure injection.[65, 144]

Similarly to the situation with bismuth electroplating (Sect. 4.3), studies on the electrodeposition of antimony and bismuth-antimony alloy nanowires in porous anodic alumina films are scarce due to the low solubility of antimony salts, and the very high[145] or very low[141, 146] pH values of common plating baths. Common antimony sources include Sb_2O_3 and SbCl_3 dissolved in inorganic acids.

Attempts to prepare near-neutral pH plating solutions of antimony with the aid of EDTA, as described previously for bismuth, were not successful. The use of antimony oxide or antimony chloride led to a large amount of precipitate. Antimony electroplating was carried out from the supernatant solutions, but the concentration of Sb^{+3} was estimated as $< 10^{-5}$ M, and the current densities were very low.

An alternative to the deposition of antimony from acidic solutions is the use of non-aqueous electrolytes. Organic polar solvents, such as *N,N*-dimethylformamide (DMF), acetonitrile, and dimethylsulfoxide (DMSO), can dissolve inorganic salts and be used for electroplating. They also have the advantage of having a broader electrochemical potential window than water, that undergoes electrolysis at -820 mV and +410 mV vs. the standard hydrogen electrode. The deposition of bismuth and bismuth-rich $\text{Bi}_{1-x}\text{Sb}_x$ nanowires from the corresponding chlorides in DMSO in PAA films has been reported recently.[134,135,147] Here, antimony and antimony-rich $\text{Bi}_{1-x}\text{Sb}_x$ nanowires were deposited from a bath of 50 mM SbCl_3 in DMSO and a bath of 55 mM SbCl_3 and 25 mM $\text{Bi}(\text{NO}_3)_3 \cdot 5\text{H}_2\text{O}$ in DMSO saturated with NaCl (Bi:Sb=3:7). The deposition was carried out in Whatman templates with 200 nm pore diameters, in the Teflon setup shown in Fig. 4-2. A freshly etched bismuth rod served as quasi-reference electrode, since the calomel electrode was observed to generate a precipitate at the water–DMSO interface.

Cyclic voltammetry studies were carried out on DMSO electrolytes, containing the bismuth salt, the antimony salt and a mixture of both. The results are shown in Fig. 4-6. The cyclic voltammograms of the mixed-ion electrolyte (solid lines in Fig. 4-6) show only one reduction wave and one oxidation wave. Furthermore, these waves do not correspond in potential and shape to either the redox waves of bismuth in DMSO or those of antimony in DMSO. The cyclic voltammetry thus indicates that the deposition and the stripping in the case of the mixed electrolyte are one-step processes, the simultaneous co-deposition or co-desorption of the two elements. The ratio of the maximum current to the individual ion concentrations is higher in the case of the mixed electrolyte than in the solutions of the individual elements, also indicating that both ions contribute to the current. The codeposition was also proved by EDS analysis of the deposit (Sect. 4.5). The codeposition of the two elements is highly desirable for the plating of alloys to prevent segregation of the elements in the deposit.

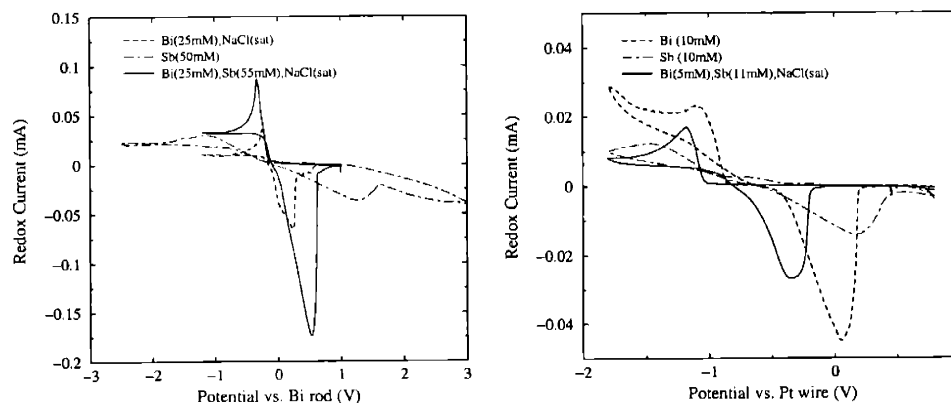


Figure 4-6: Cyclic voltammograms of DMSO-based bismuth, antimony, and bismuth-antimony electrolytes. Left: Bismuth quasi-reference electrode. Scan rate: 20 mV/sec. Right: Platinum quasi-reference electrode. Scan rate: 50 mV/sec.

4.5 Material Characterization of the Electrochemically-Deposited Nanowire Arrays

Characterization of the electrochemically deposited nanowire arrays was performed by scanning electron microscopy (SEM; JEOL 6320FV equipped with a back-scattering electron detector and an energy-dispersive x-ray detector), transmission electron microscopy (TEM; JEOL 200CX), x-ray diffractometry (XRD; Rigaku 185 mm Bragg Brentano Diffractometer), and energy-dispersive x-ray spectroscopy (EDS; in the SEM).

Figs. 4-7 and 4-8 show the cross sectional SEM view of the filled templates in the back-scattering mode, which is sensitive to the composition. The bright regions correspond to bismuth, antimony, and bismuth-antimony deposits in the corresponding images. The SEM images show that almost all the pores are filled with nanowires, i.e. a high filling-factor was achieved in each of these samples. The high filling-factors were observed only when the deposit was allowed to overfill the template, creating a continuous film over the top of the PAA template (shown on the right in Fig. 4-8a, and on the left in Fig. 4-8b). At earlier stages, i.e. before the complete filling of the

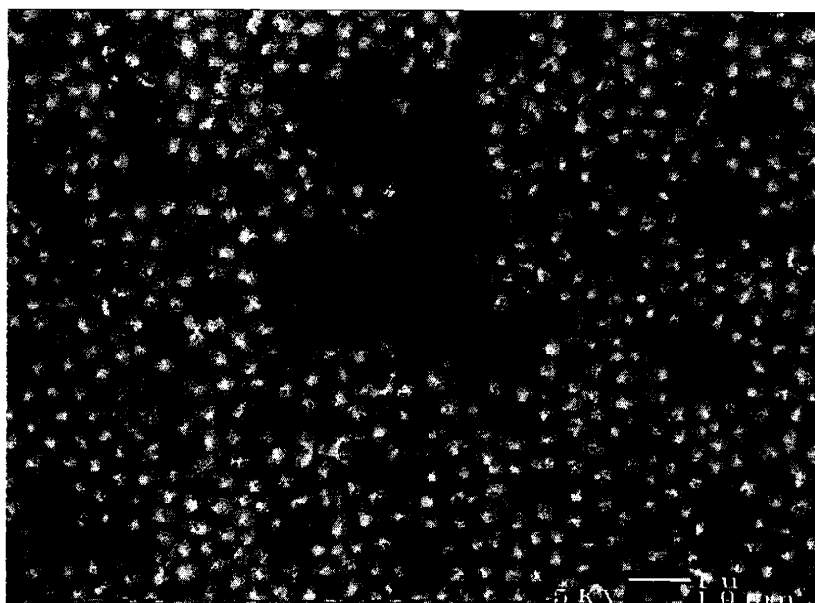


Figure 4-7: SEM image (back-scattering imaging mode) of a cross section of a bismuth nanowire-filled PAA template obtained by polishing the sample surface perpendicular to the nanowire growth direction.

template, pores were observed to be filled to different extents, suggesting the growth rate of the nanowires varies from pore to pore. The variation in growth rate was attributed to the dispersities in the pore diameter and in the quality of the pore-back electrode interface.[115, 148] The growth rate dispersion appears to depend also on the deposition conditions, as uniform nanowire growth was occasionally observed. Pulsed deposition methods have been developed to achieve more uniform filling rates and higher filling factors.[147, 149] Preliminary pulsed deposition experiments in the bismuth/PAA system did not reveal any effective improvement in the growth rate uniformity; however, a pre-deposition electrode conditioning-step (see Sect. 4.6) was found to increase the filling factor. In the case of Bi-Sb alloy nanowires (Fig. 4-8b), no domain segregation of the elements was apparent at the resolution of the instrument (better than 100 nm), although a rigorous analysis of the image brightness levels was not attempted.

EDS analysis of the samples was used to demonstrate that the material in the

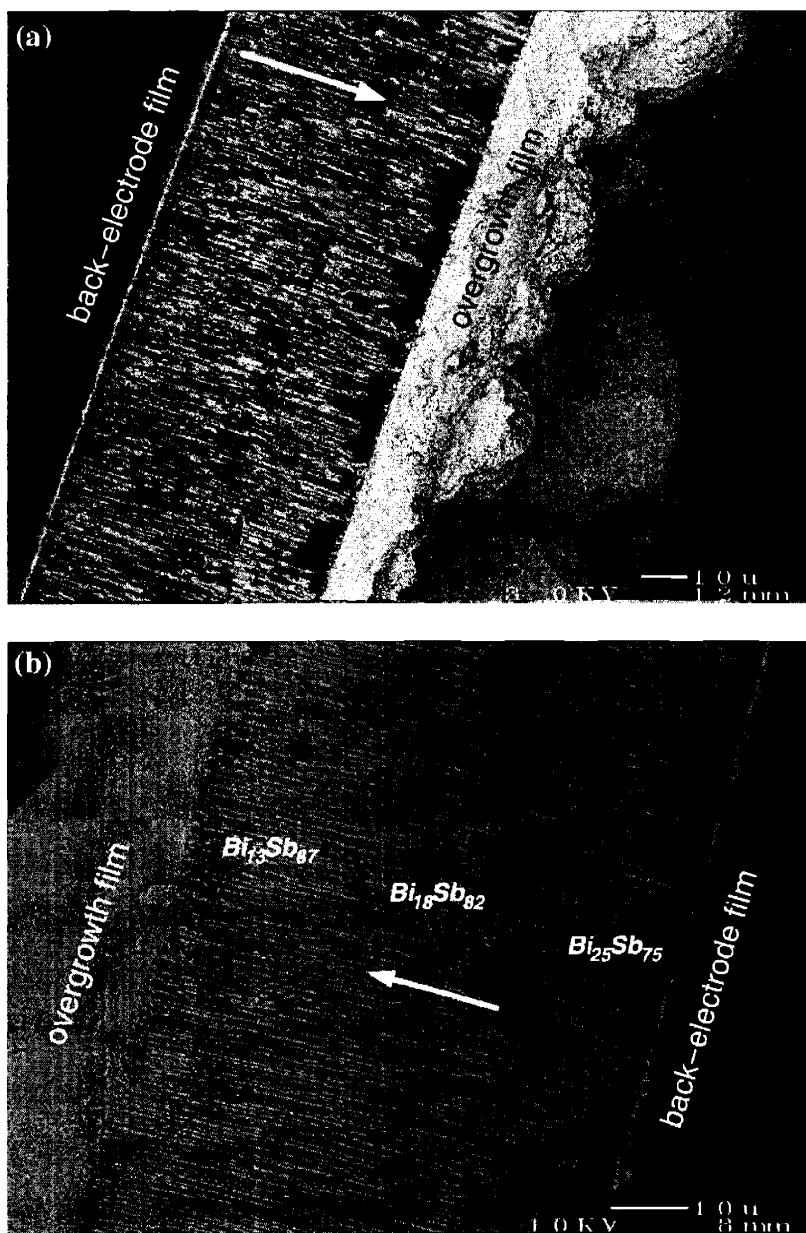


Figure 4-8: SEM images (back-scattering imaging mode) showing cross sections of nanowire-filled PAA templates obtained by film cleavage: a) antimony nanowires, and b) bismuth-antimony alloy nanowires with axial compositional-variations as indicated. The arrows indicate the nanowire-growth direction.

pore channels corresponded to the composition of the electrolytic bath. No signals from impurities, the solvent, or EDTA were observed; however, the detection limit of the technique is about 1%, the technique is not equally sensitive to all elements, and the determination of oxygen and aluminum in the nanowire was not possible due to the strong signal from the PAA matrix. The EDS analysis provided particularly interesting results for the case of the deposition of Bi-Sb alloy nanowires: First, it indicated that the deposition of antimony was preferred, as the average composition of the alloy in the nanowire ($\text{Bi}_{18}\text{Sb}_{82}$) deviated from the ratio of the elements in solution ($\text{Bi}:\text{Sb}=31:69$). Second, there was a pronounced compositional variation along the nanowire, ranging from $\text{Bi}_{25}\text{Sb}_{75}$ near the copper back-electrode to $\text{Bi}_{13}\text{Sb}_{87}$ at the top of the deposit. The initial deposit composition did not vary between nanowires plated at different potentials (-250 and -350 mV vs. Bi), but the composition variation seemed to be more pronounced in the slow growing sample (-250 mV). The enrichment of antimony was previously observed in electrochemical film deposition, where a $\text{Bi}_{11}\text{Sb}_{89}$ alloy was obtained from a DMSO bath with a concentration ratio $\text{Bi}:\text{Sb}$ of 2:6[134], and in other works with aqueous electrolytes.[141, 150] It is interesting to note, that the concentration gradient along the nanowire axis exhibits an opposite trend to what would be expected considering only that the depletion of antimony from the electrolyte occurs at a faster rate than the bismuth depletion. One might hypothesize that the mobility of the smaller antimony ions is higher than the mobility of the bismuth ions in solution. This leads to a narrower depletion region for the antimony concentration and a faster deposition rate. However, due to the confinement in the pores of the template, the difference in the mobilities of the ions is reduced. The deposition is that of an alloy with an atomic ratio similar to that of the electrolyte. As the pore filling proceeds, the diffusion processes within the pore become less influential, and the alloy resembles that obtained in film deposition.

XRD analysis of the nanowire arrays was used to study the crystal structure of the nanowires. Since the nanowires within the PAA matrix are parallel to each other and perpendicular to the film surface, the diffraction identifies the crystal planes that are perpendicular to the main nanowire axis. This is achieved by keeping the

x-ray source and detector at an equal angle with respect to the normal to the film, at opposite sides of the normal, while scanning the angle of incidence (or angle of reflection) of the x-rays (a.k.a. 2θ reflection geometry). The XRD data from arrays of electroplated bismuth nanowires 200-nm in diameter is shown in Fig. 4-9a. The data includes signals corresponding to multiple crystal planes, and their relative intensities are in agreement with the powder diffraction pattern of bismuth.[25] Similar diffraction patterns were obtained for arrays of bismuth nanowires with diameters of 70 nm and 30 nm. Measurements on arrays of antimony and Bi-Sb alloy nanowires also resulted in the powder pattern diffraction of the corresponding materials. The diffraction pattern peak positions, therefore, indicate that no significant structural change occurs within the crystal of bismuth or antimony when they are deposited into the form of a nanowire. The observed powder pattern could result from two types of samples: samples in which the nanowires are polycrystalline, and samples in which the nanowires are single-crystalline but there is no global relation between the crystal axes and the nanowire main axis.

TEM provided further information regarding the microstructure of the nanowires (Fig 4-9b). Electron diffraction patterns from individual nanowires 70-nm in diameter showed several diffraction patterns superimposed on each other, indicating the existence of multiple crystal grains along the nanowire. The grain size was determined by dark-field imaging to be of the order of the wire diameter. None of these TEM studies was successfully performed on nanowires 200-nm in diameter, since the electron beam transmission through the thicker samples was too weak to be detected. A polycrystalline structure was assumed as the reason for the powder pattern XRD signal from the 200-nm diameter samples as well.

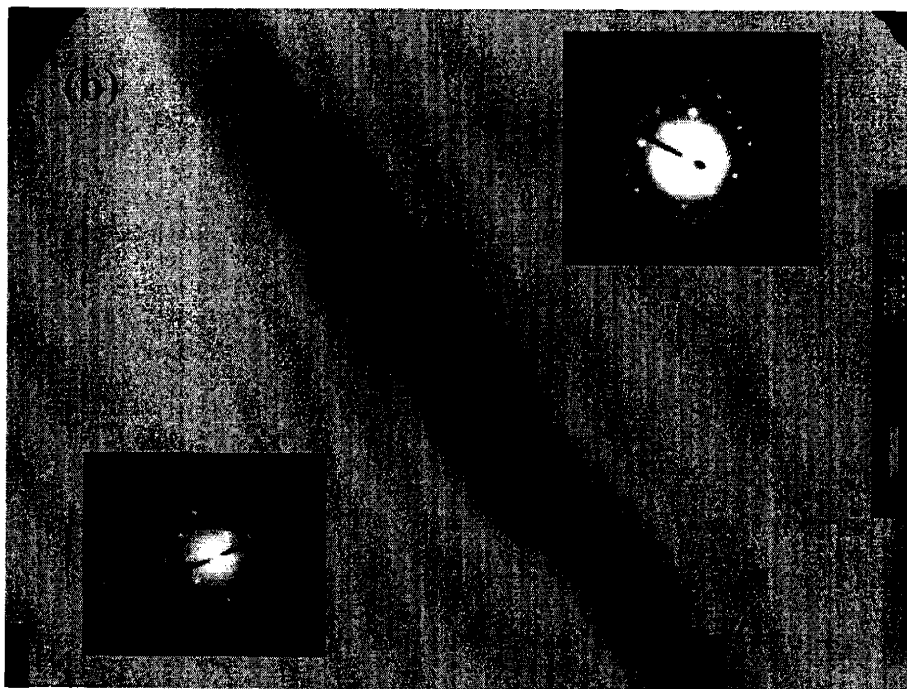
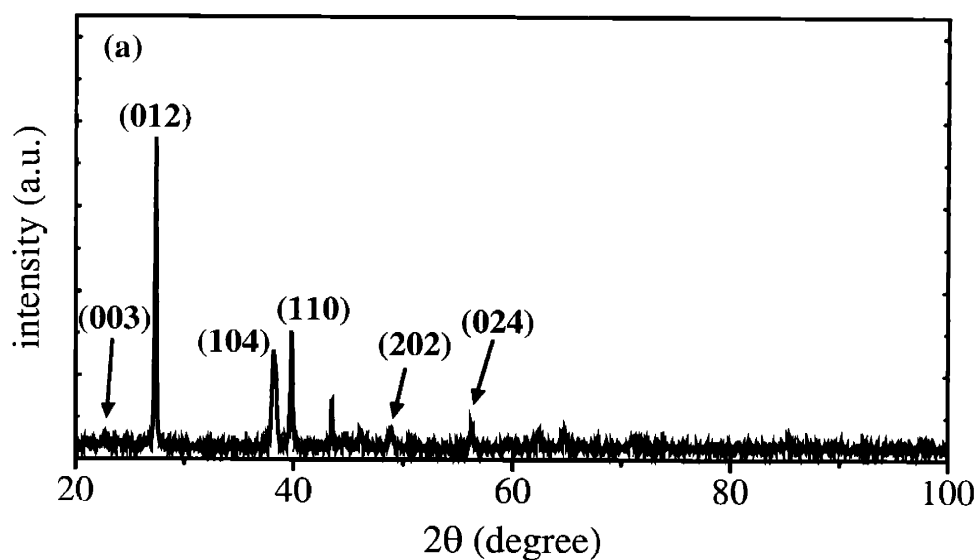


Figure 4-9: (a) XRD pattern from an array of as-deposited polycrystalline bismuth 200-nm diameter nanowires. (b) TEM image of a 70-nm diameter nanowire indicating its polycrystalline nature. The insets show electron diffraction patterns from different bismuth grains.

4.6 Improving the Crystallinity of the Electrochemically-Deposited Bismuth Nanowire Arrays

Since bismuth is an anisotropic material, the properties of the nanowires are predicted to depend on the crystallographic orientation along the main axis. The properties will differ also between a single crystal and a polycrystalline nanowire, in which all the orientations are sampled. Furthermore, enhanced carrier scattering is expected in polycrystalline samples due to the grain boundaries. Comparison between transport in bismuth nanowires arrays prepared by electrochemical deposition[129,132] and impregnation methods[130] shows that the temperature dependence of the resistance of these samples can differ significantly. The distinguishing behavior is particularly pronounced in bismuth nanowires 100–200 nm in diameter. The differences in electrical transport could be attributed to the polycrystalline nature of the electrodeposited samples[129] versus the crystallographically oriented single-crystal nature of the nanowires made by the physical methods.[64]

Electrochemical deposition, unless well-controlled, generates solid material with a polycrystalline microstructure. This microstructure results from deposition under non-equilibrium conditions. Non-equilibrium conditions in the electrochemical cell can be a result of an excessive applied over-potential at the electrode, or the accumulation or depletion of the reactants or products of the reaction near the electrode (“the diffusion layer”) due to high generation rates and low diffusion rates. Additionally, surfactants and contaminants can promote polycrystallinity by impeding the growth rates of crystals and promoting nucleation events.

Three approaches can be adopted in order to improve the crystallinity of the electrodeposited material:

1. Following the deposition steps, the material can be annealed or recrystallized by a physical method, such as thermal treatment or pulsed laser irradiation.
2. The electrodeposition can be carried out with a tight control over the elec-

trode over-potential to minimize the nucleation rate for new crystallites. Very slow growth rates will be necessary to ensure that the electron transfer reactions proceed at near-equilibrium conditions, and new atoms are incorporated solely at the low-energy lattice sites. Furthermore, competing processes, such as hydrogen formation, are reduced.[151, 152]

3. Pulsed deposition techniques are employed to ensure a steady supply of ions to the growing crystal.[153, 154] A short deposition pulse is applied, followed by a long rest period. During the rest period, the concentration of the ions near the surface of the electrodes is allowed to recover. A stripping pulse can also be applied following the deposition pulse to redissolve atoms that were deposited in unfavorable lattice sites.[149]

The first two approaches were found to be effective in improving the crystallinity in arrays of electrodeposited bismuth nanowires 200-nm in diameter. The results are presented in Fig. 4-10 with a comparison to a randomly oriented sample.

Nanowire arrays were heat-treated in a tube furnace under a flow of 5% H_2/N_2 at atmospheric pressure at 300°C for 3 hours followed by a slow cooling at a rate of 40°C per hour. The melting point of bismuth is 278°C, so the nanowires are expected to melt and recrystallize during the process. The XRD pattern of the heat-treated arrays show a significant improvement in the nanowire crystallographic orientation (compare Fig. 4-10b *vs.* Fig. 4-10a), with 82% of the sample presenting the (101) planes normal to the nanowire main axis and 12% of the sample presenting the (110) planes. These orientations were also obtained perpendicular to the surface, when an electrodeposited *film* of bismuth on a copper substrate was heat-treated under the same conditions. The (101) signal also dominated the diffraction pattern of bismuth nanowires with diameters larger than 50-nm, prepared by the pressure injection technique.[64, 130] It is therefore probable that even more uniform crystallinity can be achieved by the optimization of the annealing conditions. However, this approach is not the most favorable. During the recrystallization process, volume changes occur as bismuth undergoes phase transitions. It was found that the resistance of the sample increases

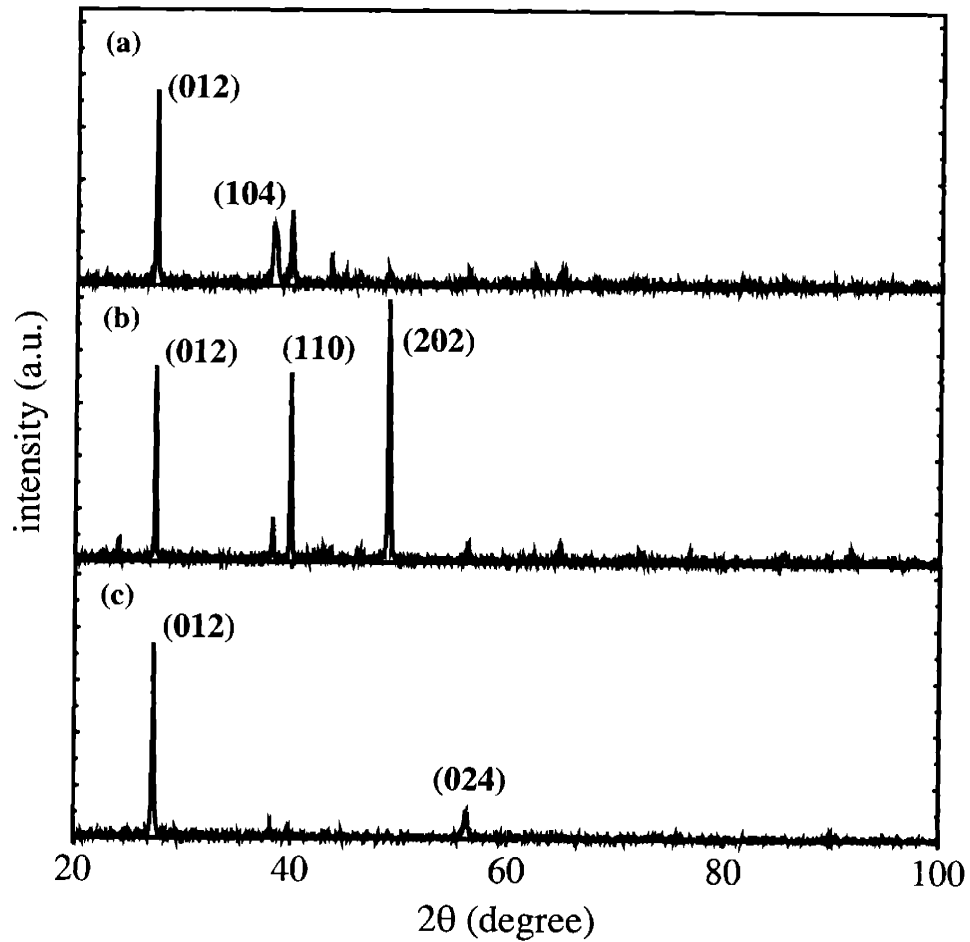


Figure 4-10: XRD pattern from bismuth 200-nm diameter nanowire arrays: a) as-deposited polycrystalline nanowires, b) same sample after thermal treatment at 300°C, and c) as-deposited crystallographically-oriented nanowires.

substantially, suggesting the nanowires become discontinuous, and possibly oxidation occurs even though reducing conditions were employed as a precaution. It was also found that bismuth reacts under the process conditions with other metals to create intermetallic compounds. Diffraction peaks from Au_2Bi were observed after annealing a bismuth film on a gold electrode, also indicating that bismuth rapidly diffused through the gold layer. Thus, the heat-treatment limits the range of materials that can be used in the back-electrode to metals that do not form intermetallic compounds with bismuth, such as copper. Interestingly, no improvement in crystal quality was observed when the heat-treatment was carried out under low pressure conditions (40 millitorr) instead of the H_2/N_2 gas flow. This observation suggests that the presence of bismuth oxide can thwart the formation of large-grain bismuth crystals.

The crystal quality of bismuth nanowires 200-nm in diameter was also improved by adjusting the electrodeposition conditions to generate as-deposited crystallographically oriented nanowires. To achieve this goal, efforts were directed into the elimination of parasitic current losses and voltage drops in the system, while maintaining a low electrode over-potential. Current losses were observed due to leakage of the electrolyte through the pores or through the protective insulating coating. The electrolyte would eventually reach the metallic film on the back of the working electrode, as evident by bismuth deposits found on the back side of the electrode. The leakage was prevented by the electroplating of a thick copper layer on the back of the working electrode to seal the pores. Satisfactory platings were achieved with a commercial copper sulfate electrolyte (Technic-Copper-U), a current density of 1.8 mA/cm^2 , deposition time of 2 hours, and a platinum mesh counter electrode. The insulating coating was avoided completely by the use of the deposition setup shown in Fig. 4-2, as described earlier, further minimizing the leaks. Accurate electrode potential control was improved by the addition of a supporting electrolyte of 1 M KNO_3 to the plating solution. This leads to the reduction of the resistance of the electrolyte, and thus a lower error in the measurement of the cell potential. In addition to the electrochemical potentials and the iR potential, interfacial chemical potentials also contribute to the measured cell potential. In the bismuth deposition set-up, when

using a SCE, the reference electrode is kept in a separate compartment (containing a 1 M KNO_3 electrolyte) to separate the bismuth ions from the chloride ions, and to prevent precipitation. Interfacial potential drops exist across the ceramic membrane or the salt-bridge connecting the SCE compartment and the bismuth electrolyte compartment. To eliminate those interfaces, we opt for using a freshly-etched bismuth rod as a quasi-reference electrode that can be immersed in the same compartment as the working electrode. After implementing these modifications, electrodepositions were carried out, first at -450 mV for 1–3 minutes, and then at -350 mV for at least 1 hour. The initial higher over-potential is used to promote the nucleation of bismuth deposits in as many pores as possible, overcoming variations that exist in the pore-back electrode interface from pore to pore. The potential is then turned to a more positive value to enhance the growth rate over the nucleation rate, and prevent the polycrystalline morphology of the plated material. The XRD patterns of the as-deposited nanowire arrays obtained by this approach show exclusively the (012) and the (024) diffraction peaks, as shown in Fig. 4-10c, indicating that crystallographically oriented nanowires were obtained, and no post-deposition treatment was necessary. Interestingly, the nanowires obtained by this approach show a different preferred orientation than those prepared by a physical method [(012) in this work versus (101) in Ref. [64]]. By subjecting the (012)-oriented nanowire arrays to 272°C for 6 hours, diffractions from the (101) and the (110) planes became stronger, indicating a thermodynamic driving force for these crystal planes to align in the radial directions.²

4.7 Electrical Characterization of the Electrodeposited Nanowire Arrays

Several studies were reported on the electrical properties of bismuth nanowire arrays. Review of these studies reveal several difficulties in the analysis of the results. Due

²In nanowires made by pressure injection, the preferred orientation along the main axis changed to (012) as the nanowire diameter was decreased below 50 nm.[13]

to the difficulties in making contacts to an individual nanowire[155], all but one[156] of the reported measurements have been carried out on arrays of nanowires embedded in a supporting matrix (in many cases, porous anodic alumina). This geometry allows only 2-point resistance measurements to be made, and the number of connected nanowires is unknown. The resistance values thus measured include both the intrinsic resistance of the nanowire array and the contact resistance. The resistance values cannot be accurately converted into resistivity values. Therefore, electrical characterization of the nanowires has focused on the dependence of the resistance on measurement conditions (i.e. temperature and magnetic field strength), and the dependence of these trends on nanowire diameter, microstructure and composition.

Measurements on bismuth nanowires prepared by the pressure injection and the vapor phase technique display very interesting electrical phenomena. As a function of wire diameter, the resistance can decrease monotonically with an increase in temperature (diameter < 50 nm) or can show a non-monotonic behavior with a broad maximum near 100 K (diameter > 50 nm).[15] Fig.4-11 shows the results of a collection of these measurements. These observations were ascribed to the theoretically predicted semimetal- to semiconductor transition in bismuth nanowires due to quantum confinement effects.[130] While this is the general trend, several exceptions were reported. For example, Zhang *et al.*[157] reported a monotonic behavior for 65 nm diameter bismuth nanowires, and a nearly-monotonic behavior for 60–110 nm diameter nanowires doped with tellurium. In the last example, the temperature dependence changed upon annealing. Huber *et al.* reported a resistance monotonically decreasing for 30 nm diameter nanowires[128], but a resistance monotonically increasing with temperature for 270 nm diameter nanowires with no maximum (up to 300 K).[131]

In contrast, measurements performed on bismuth nanowires prepared by electrochemical deposition in polymeric templates, all show a monotonic decrease of the resistance of the array with increasing temperature, even though the wire diameters were large (95 nm to 2 microns).[129, 132, 158] Examples of such results are shown in Fig. 4-12.

The differences between the sets of results obtained from samples prepared by the

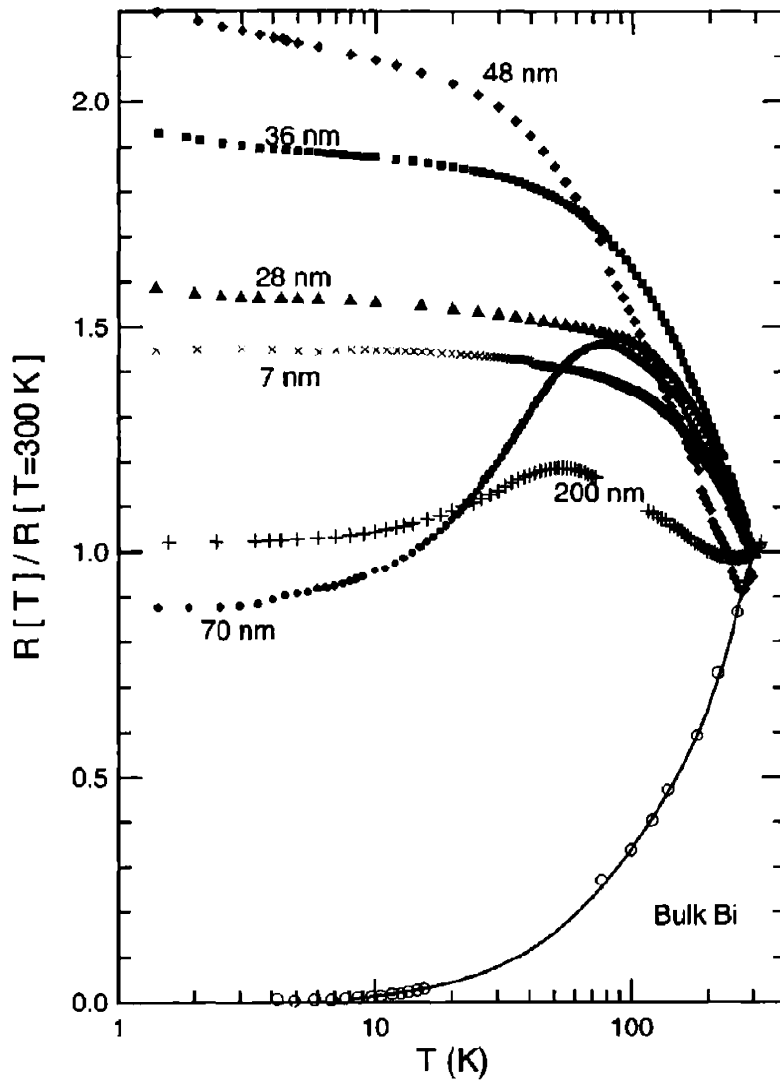


Figure 4-11: Temperature dependence of the normalized resistance $R(T)/R(300\text{ K})$ for bismuth nanowire arrays of various wire diameters prepared by the vapor deposition method, in comparison with the corresponding data for bulk bismuth.[15] These nanowires are crystallographically oriented, and appear to be single-crystals.

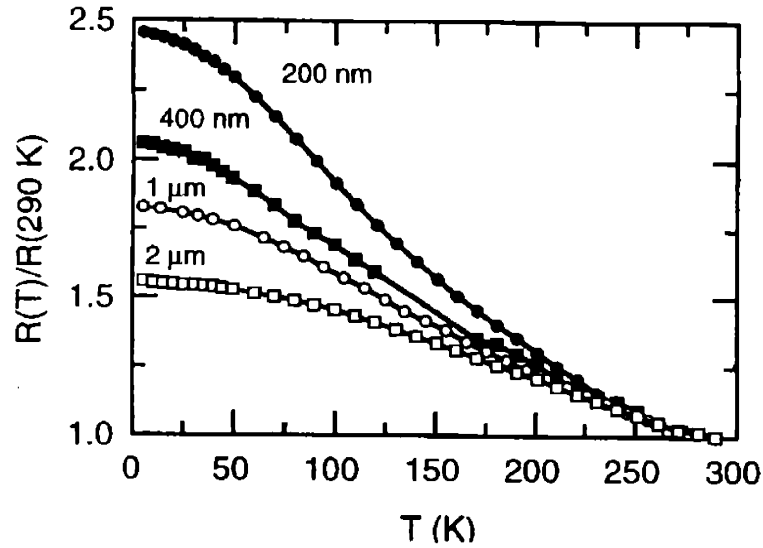


Figure 4-12: Temperature dependence of the normalized resistance $R(T)/R(300\text{ K})$ for bismuth nanowire arrays of various wire diameters prepared by electrochemical deposition.[158] These nanowires are polycrystalline.

different methods were explained in terms of the polycrystalline nature of the electrodeposited nanowires in comparison to the single-crystal nanowires of the physical methods. Model calculations for 70-nm diameter nanowires[130] have shown that the difference in behavior can be attributed to higher boundary scattering rates in the electrochemically deposited nanowires. Further discussion of this model will be presented below. Further indication for the reduced carrier mobilities in the electrodeposited bismuth nanowires was obtained by magnetoresistance studies. Measurements of the resistance vs. magnetic field in pressure injection samples show a maximum resistance at a threshold field strength, beyond which the resistance decreases.[157] The negative magnetoresistance at applied fields larger than the threshold field was explained as the confinement of the helical motion of the electrons into a diameter smaller than the nanowire diameter, so that the wire boundary scattering becomes less relevant.[11] Negative magnetoresistance was not observed in the electrodeposited nanowires[129, 158] or was observed at very high magnetic fields.[132] In these sam-

ples, the grain-boundary scattering is the dominant scattering process, limiting the mean free path of the carriers below the wire diameter. Therefore, boundary scattering at the wire boundary interface does not significantly affect the carrier mobilities and the sample resistance.

Magnetoresistance (MR) measurement on nanowire arrays prepared by electrodeposition from EDTA-containing electrolytes (see Sect. 4.3) in anodic alumina templates were performed in this work. Figs. 4-13 and 4-14 present the temperature and magnetic field dependence of the resistance of bismuth nanowire arrays of representative pore diameters, above and below the predicted threshold diameter for the semimetal-to-semiconductor transition. The results are similar to those reported for larger diameter electrodeposited nanowires, showing a monotonic decrease in resistance with increasing temperature. There is no clear dependence of the slope $\partial R/\partial T$ on the nanowire diameter, as suggested from the data on large diameter bismuth wires.[158] The longitudinal magnetoresistance data shows that the resistance levels off at high fields, but no negative magnetoresistance conditions were attained at $B < 5.5T$. Here again, there is no clear dependence on wire diameter. The non-monotonic dependence of transport properties on wire diameter was also reported by others.[129, 132] The magnetoresistance however indicates that the carrier mobility in the 70-nm diameter array is high (large MR), and this sample also gives the weakest temperature dependence. Such a connection will be seen again below, in the context of the improvement of the crystallinity. For the analysis of a collection of samples, it is evident that the slope $\partial R/\partial T$ and the MR of the nanowire arrays can vary between samples of the same diameter as much as between samples of different diameters. The electrical transport properties are effected by the age of the sample, by thermal treatments, and very significantly, by the quality of the top and bottom contacts. As a whole, these results indicate that the carrier mobilities in the electrodeposited bismuth nanowires are low due to the grain boundary scattering in the polycrystalline samples, and that the mean free path of the carriers is shorter than the wire diameter. In particular, the low mobility is noticeable in the low temperature regime ($4\text{ K} < T < 30\text{ K}$) where the resistance appears as a plateau. In this

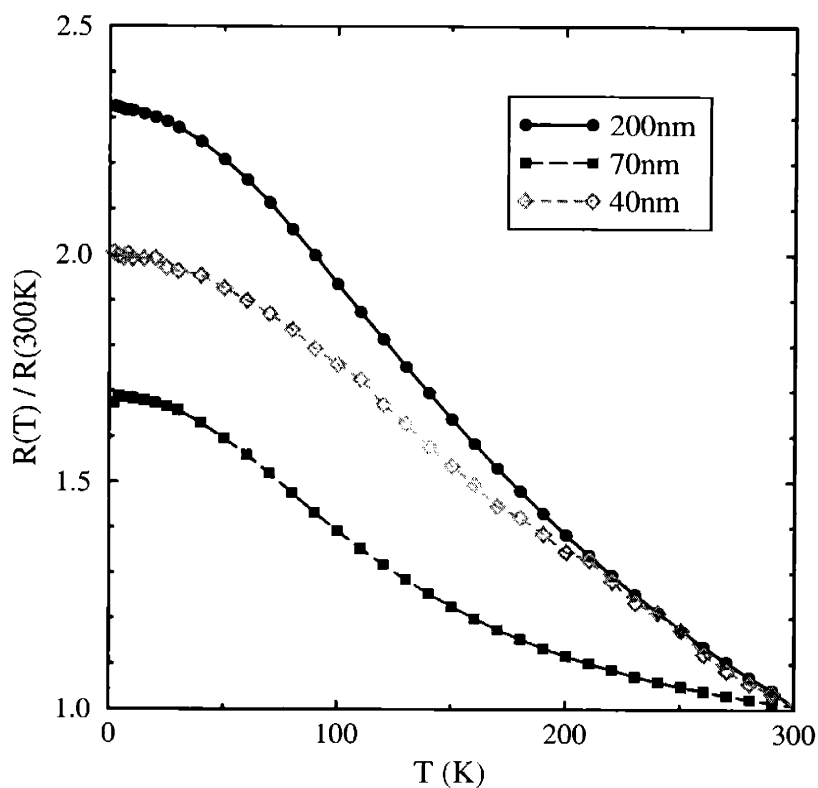


Figure 4-13: Temperature dependence of the normalized resistance $R(T)/R(300\text{ K})$ for bismuth nanowire arrays of various wire diameters prepared by electrochemical deposition.

temperature range, the carrier density in semimetallic bismuth is not strongly influenced by the temperature, while the mobilities have a strong temperature dependence (Hartman suggested a T^{-2} dependence[159]). Thus, observable changes in resistance are attributed to mobility changes. The plateau indicates the dominance of a scattering mechanism that is temperature independent and not found in single-crystal, bulk samples. Grain boundary scattering and nanowire boundary scattering satisfy these criteria. At higher temperatures, the overlap between the conduction band and the valence band increases exponentially[44], leading to an increase in carrier density and a decrease of the resistance. The plateau, however, is not a result of weak localization effects, which vanish at temperatures about $\sim 10\text{ K}$ and have distinguishable magnetoresistance signatures.

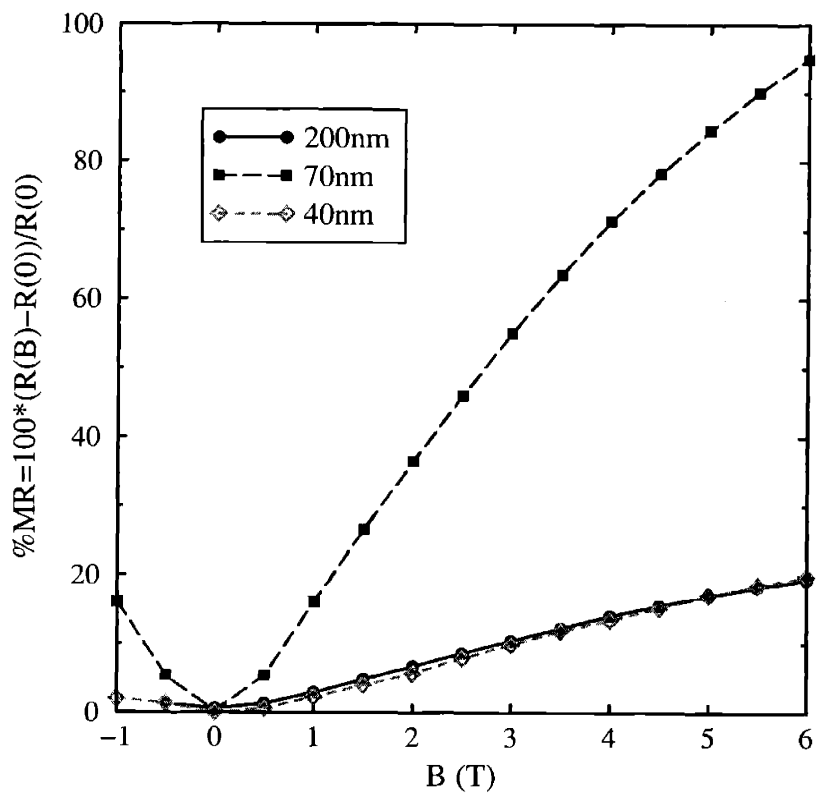


Figure 4-14: Magnetoresistance of bismuth nanowire arrays of various wire diameters prepared by electrochemical deposition measured at 4 K.

Comparison between the resistance of polycrystalline arrays and crystallographically-oriented arrays of bismuth nanowires prepared by the same synthetic method should be indicative of the effect of grain-boundary scattering on the electrical transport. Fig. 4-15 shows the temperature dependence of the resistance of bismuth nanowire arrays 200-nm in diameter. This diameter was chosen because dramatically different behaviors were found across the synthetic methods for this diameter (compare Figs. 4-11, 4-12, 4-13), no significant quantum effects are expected, and templates are readily available. A distinctive difference was found in the resistance of the (012) crystallographically oriented sample compared to that of polycrystalline samples of the same wire diameter, although the general trends were conserved. The slope $\partial R/\partial T$ in the vicinity of room temperature is lower in the crystallographically-oriented sample leading to a lower value of $R(4\text{ K})/R(30\text{ K})$. Different samples of varying absolute values of the resistance were tested to ensure that the difference is not due to the contact resistance. The crystallographically-oriented array shows a resistance saturation at $T < 30\text{ K}$ as well. The magnetoresistance of this array is high, but not exceptionally high (26% at 5 Tesla).

Model calculations were used to obtain fits to the experimental results. The resistivity of the bismuth nanowire was calculated according to

$$\rho(T) = [N_e(T)e\hat{\mu}_e(T) + N_h(T)e\hat{\mu}_h(T)]^{-1} \quad , \quad (4.1)$$

where N_i is the carrier density, e is the electron charge, $\hat{\mu}$ is the average carrier mobility, and the subscripts x_e and x_h indicate electrons and holes, respectively. The carrier density is calculated from the bulk band structure, the doping density, and the temperature. The average mobilities are calculated by adding the contributions of the different scattering mechanisms according to Matthiessen's rule:

$$\frac{1}{\mu_{\text{tot}}(T)} = \frac{1}{\mu_{\text{bulk}}(T)} + \frac{1}{\mu_{\text{bound}}} + \frac{1}{\mu_{\text{imp}}(T)} \quad , \quad (4.2)$$

where μ_{bulk} is the carrier mobility in bulk crystalline bismuth, and μ_{bound}^{-1} and μ_{imp}^{-1} account for boundary scattering and charged impurity scattering, respectively. The T dependence of $\mu_{\text{bulk}}(T)$ is mainly due to electron-phonon scattering, while μ_{bound} is assumed to be T -independent. For most bulk materials, impurity scattering contributes

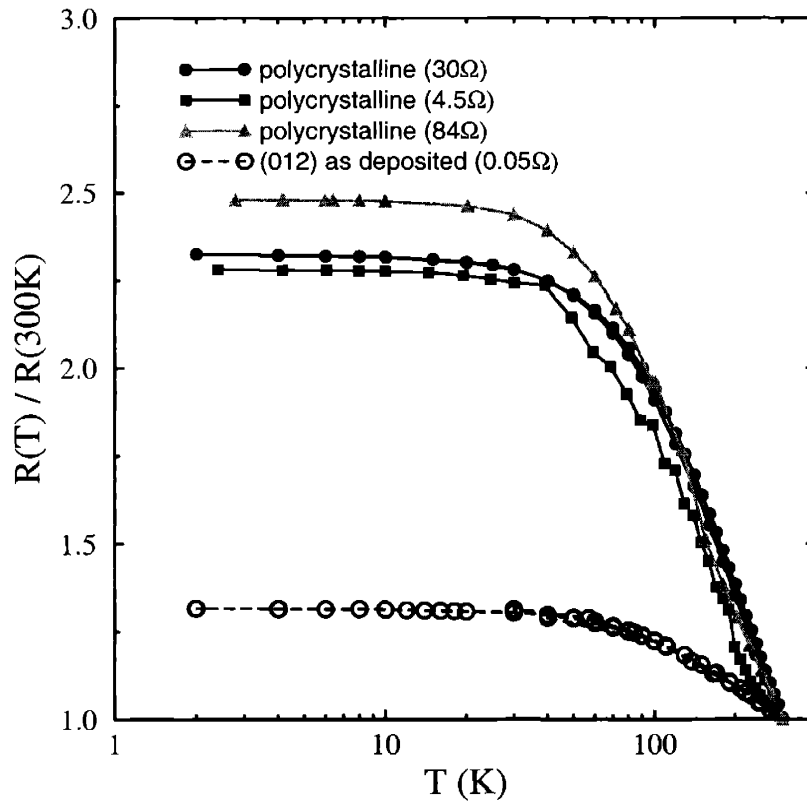


Figure 4-15: Comparison of the temperature dependence of the normalized resistance $R(T)/R(300\text{K})$ for electrodeposited bismuth nanowire arrays 200-nm in diameter with different microstructures. The values in parenthesis are the room temperature resistances of the samples.

to a temperature-dependent mobility $\mu_{\text{imp}} \sim T^{3/2}$, and the same temperature dependence is assumed for nanowires. Three fitting parameters were used: the extrinsic carrier concentration ($N_h - N_e$), and two parameters defining the absolute contributions of the boundary scattering and of the ionized impurity scattering to the total mobility. Fig. 4-16 shows the effect of the rate of the boundary scattering on the shape of the $R(T)$ curve. It is noticed that as the scattering rate is increased, the curves shift from non-monotonic curves to curves showing a plateau at low temperatures. While the model does not quantitatively fit the experimental results, it suggests that a temperature-independent mechanism dominates the mobilities of the carriers in electrodeposited nanowires, both for polycrystalline and crystallographically-oriented samples. The behavior observed in vapor impregnated and pressure injection samples suggests higher, bulk-like mobilities. The difference in the $R(T)$ curves for the two sets of electrodeposited samples could be obtained from the model by setting μ_{bound} to a low value and varying the carrier concentration. The best fits are shown in Fig. 4-17. The results indicate that the crystallographically-oriented samples have a higher dopant concentration. While this is a possibility, it is not the only interpretation of the results. Since the model uses an extremely simplified view of the transport in bismuth, many effects were not taken into account, and they are interpreted by the model as a change in doping or a change in mobility, while their true nature is likely to be more complex. For example, changes in the band structure of bismuth due to the polycrystalline nature of the deposit may occur. The more localized nature of the wavefunction in the polycrystalline system can result in a change in the overlap energy, similar to the quantum confinement effect by the nanowire boundary. In this case, the contribution of intrinsic carriers to transport will be reduced, and the model will interpret it as an increase in the contribution of extrinsic carriers, i.e. higher doping.

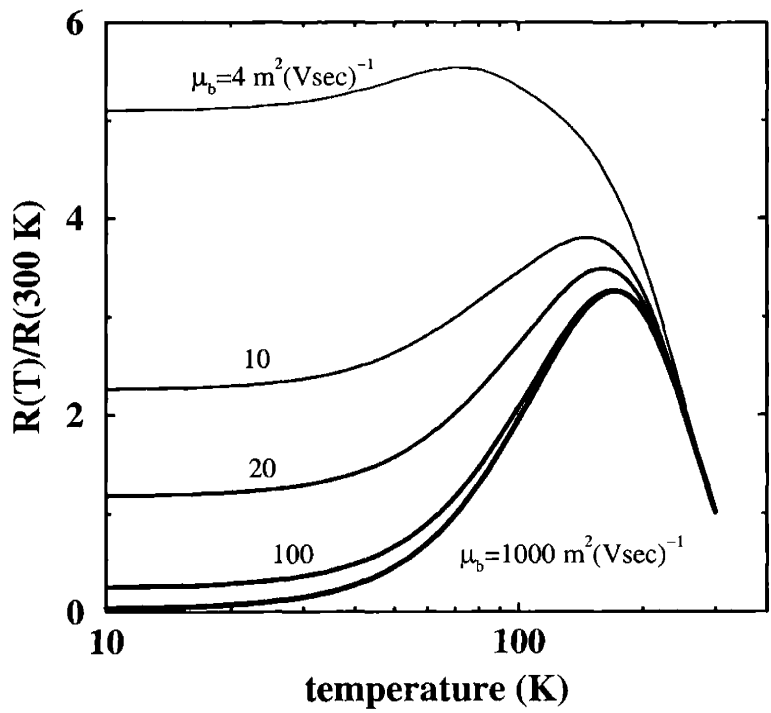


Figure 4-16: Calculated temperature dependence of the normalized resistance $R(T)/R(300\text{ K})$ for bismuth nanowires varying the contribution of the boundary scattering in Eq. 4.2, as indicated. The extrinsic carrier concentration was fixed at $2 \cdot 10^{17}\text{ cm}^{-3}$.

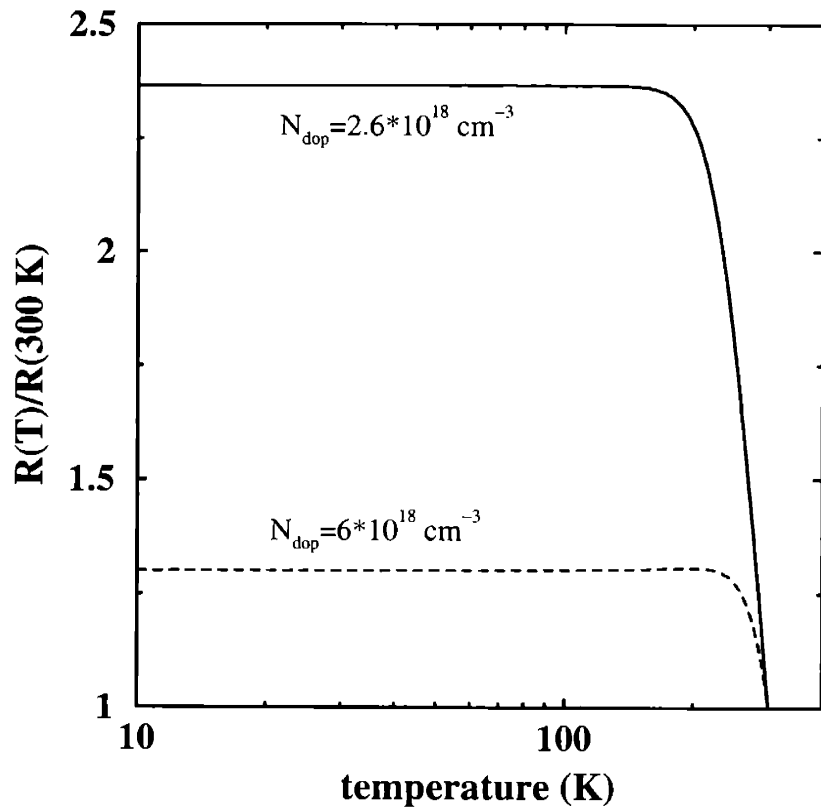


Figure 4-17: Calculated temperature dependence of the normalized resistance $R(T)/R(300\text{ K})$ for bismuth nanowires with large boundary scattering varying the extrinsic carrier concentration (N_{dop}). The indicated carrier concentration were chosen to simulate the data of Fig. 4-15.

4.8 Summary and Future Work

In summary, significant improvement has been made in the electrochemical synthesis of bismuth nanowires. New electrolytes were employed in conjunction with porous anodic alumina templates to fabricate bismuth, antimony, and $\text{Bi}_{1-x}\text{Sb}_x$ nanowire arrays. Dedicated efforts to obtain crystallographically oriented samples were successful. This provided a unique opportunity to compare the electrical properties of polycrystalline and oriented nanowires prepared by the same technique. The electrical transport characteristics of the oriented samples are similar to those of polycrystalline samples in the low temperature regime, but approximate the vapor-impregnation samples at high temperatures.

Model calculations for the temperature dependence of the resistance on temperature were employed to fit the experimental results. The model reveals that the carrier mobilities were apparently not improved by a significant amount. Similarly, no large increase in magnetoresistance was recorded. It is still unclear what is the mechanism that limits the carrier mobilities at low temperatures, and if it is intrinsic to the electrochemical growth process. Newly emerging synthetic methods, such as pressure-induced nanowire growth[160], may cast new light on these remaining questions.

It is imperative to find more ways to improve the measurement technique and sample fabrication. In the current arrangement, the overgrowth of bismuth is utilized to make a contact to the nanowire. The contact resistance, and the temperature and field dependence of the resistance of the bismuth film may not be negligible, as the filling factor of the samples was dramatically improved by the electrochemical deposition process, and the total resistance dropped to the $\text{m}\Omega$ range. An encouraging approach was demonstrated by Wegrowe *et al.*[161] to stop the growth of nanowire as they begin to emerge from the pores, but only few pores are fully filled by this method. If samples with contact layers of only several tenths of nanometers in thickness were produced, the thermoelectric quantities measured would truly reflect the properties of the array.

Chapter 5

Enhancement of Weak Anti-Localization Effects in Nanostructured Bismuth Thin Films

5.1 Introduction

5.1.1 Weak Localization

The weak localization effect is a quantum mechanical effect that is a manifestation of the wave-like nature of the conduction electrons in a solid. (For an excellent review of the physical interpretation of weak localization in thin films see Ref. [162]). The effect causes changes in the resistance of microscopically disordered materials: As the conduction electrons travel in the solid, they repeatedly collide with the randomly distributed defect sites. When elastic scattering is dominant, the scattered electron waves retain their energy and phase coherence, allowing for interference (constructive or destructive) to take place. Various scattering trajectories from electron state \mathbf{k} at time t to state \mathbf{k}' at time t' are possible (by different sequences and numbers of energy-conserving/momentum-modifying events). The electron wavefunction experiences a

different phase shift in each trajectory. The probability to find the electron at the final state \mathbf{k}' at time t' will depend on the amplitude and the phase relation between the scattered wavefunctions obtained from each of the scattering trajectories. In general, there is no correlation between the phase evolution in the different \mathbf{k} -to- \mathbf{k}' trajectories, and the interference effects average out. A special situation, however, occurs for electrons scattered from state \mathbf{k} at time t to state $-\mathbf{k}$ at time t' : Due to time-reversal symmetry, constructive interference is guaranteed from electrons scattered through the two sequences $\{\mathbf{k}, \mathbf{k}_1, \mathbf{k}_2, \dots, \mathbf{k}_{n-1}, \mathbf{k}_n = -\mathbf{k}\}$ and $\{\mathbf{k} = -\mathbf{k}_n, -\mathbf{k}_{n-1}, \dots, -\mathbf{k}_2, -\mathbf{k}_1, -\mathbf{k}\}$. Thus, the probability of scattering from state \mathbf{k} at time t to state $-\mathbf{k}$ at time t' , a process known as *back-scattering*, is twice as large as that expected in the absence of coherence effects (*i.e.*, a classical system). In real space, the enhanced back-scattering phenomenon is interpreted in a *slower-than-expected* motion of a collection of electrons in the direction of an applied field, and this effect will be detected as an increase in the resistance of the sample (compared to a hypothetical sample, in which quantum interference effects between the electrons do not exist).

Application of a magnetic field to the sample lifts the time-reversal symmetry, disturbing the interference mechanism responsible for the enhanced back-scattering. As a result, the resistance of the sample will decrease in the presence of the magnetic field. One way that the weak localization effect is detected is by studying the magnetic field dependence of the resistance. Depending on the dimensionality of the sample (wire, film, or bulk), the expression of the magnetic field dependence of the resistance takes a different functional form.[163] The present study focuses on two-dimensional thin film systems, where the diffusion length of the carriers is longer than the film thickness.

Since the weak localization effect depends on the coherent superposition of scattered waves, conservation of the phase of the traveling electrons is crucial for the observation of localization. Inelastic scattering events randomize the phase of the scattered wave. Elastic scattering events conserve the phase information. Thus, the magnitude of the weak-localization effect depends on the ratio between elastic and inelastic scattering rates in the sample. This ratio decreases with increasing temper-

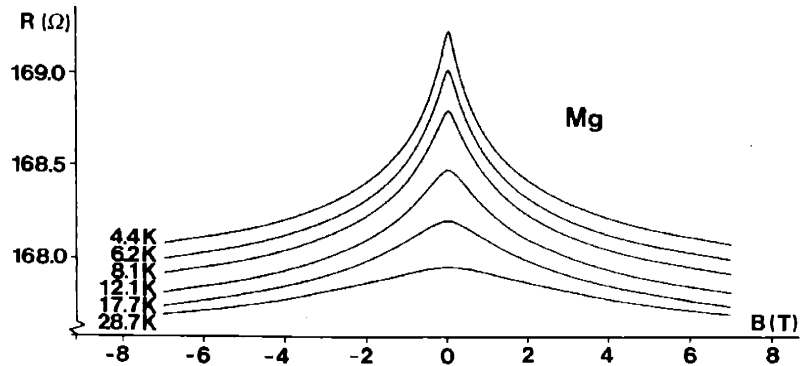


Figure 5-1: Magnetoconductance curves of a thin magnesium film as a function of temperature. Adapted from Ref. [162].

ature, leading to the weakening of the weak localization effect as the sample temperature is increased. Weak localization effects are significant only at temperatures below 10 K. Figure 5-1 shows the magnetic field dependence of the resistance taken at different temperatures for a thin magnesium film displaying typical weak localization characteristics.

5.1.2 Weak Anti-Localization

The weak localization effect was described as a result of the coherent interference between pairs of back-scattering ($\mathbf{k} \Rightarrow -\mathbf{k}$ transition) trajectories. In this discussion, it was assumed that the spin part of the wavefunction of the electrons does not change. However, in the presence of spin-orbit interaction, which is pronounced in large atomic mass materials, the electron spin will accumulate a different phase in each of the time-reversal symmetry-related scattering sequences. The probability of back-scattering decreases with an increase of the spin-orbit coupling; in fact, at large spin-orbit coupling, destructive interference reduces the probability of back scattering below the classical sum of the contributions of the various trajectories to the back-scattering probability amplitude. This phenomenon is referred to as *weak anti-localization*, since it is manifested in a *higher-than-expected* conductivity of the

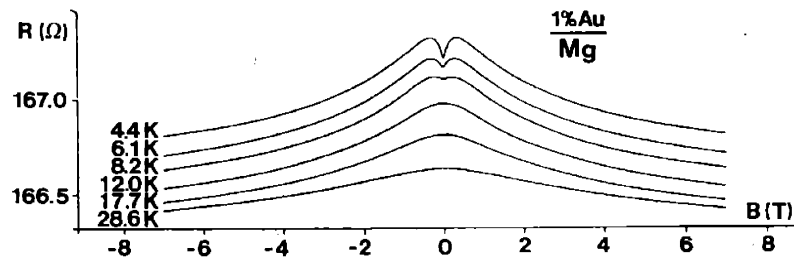


Figure 5-2: Magnetoconductance curves at various temperatures of a gold-doped thin magnesium film. Adapted from Ref. [162].

sample. Figures 5-2 and 5-3 show the weak anti-localization effect, as it is manifested in the magnetoconductance of gold-doped magnesium and gold thin films, respectively.

5.1.3 Motivation

In order to observe and study weak localization effects in thin films, a great effort is invested in engineering the structure of the film. In essence, films need to be prepared with a large density of randomly distributed scattering centers. This is commonly achieved by the deposition of the material to be investigated on a cold substrate using a low-pressure film deposition technique. The low temperature of the substrate reduces the mobility of the adsorbed atoms on the surface of the substrate, and thus prevents the relaxation of the structure and the annealing of defects. The introduction of oxygen during the deposition and the accurate variation of the film thickness near the percolation threshold were also used to modify the structure and the resistance of the films in an empirical way.

Here, a new approach for the enhancement of weak localization effects is presented, in which nano-structured substrates are utilized to induce the growth of nano-structured thin films. The surface of the nano-structured substrates contains an array of nano-sized pores, formed by self-assembly or patterning. The structure and weak anti-localization properties of the thin films grown on a nano-structured substrate and on a flat substrate are compared. Reproducible results were obtained, even though the temperature of deposition was not controlled.

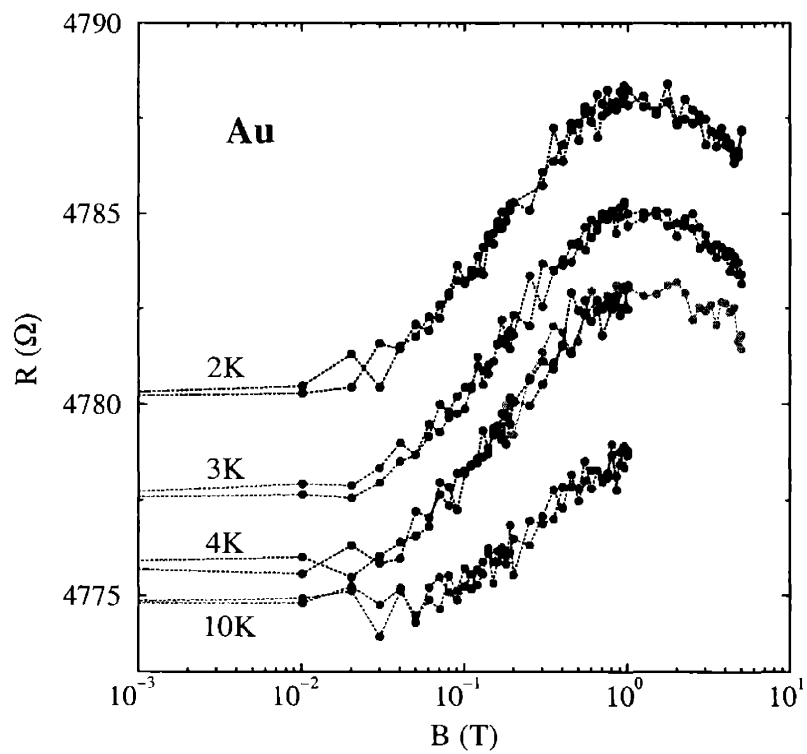


Figure 5-3: Magnetoresistance curves at various temperatures of a 6-nm thick gold film grown on glass. Film fabrication and data acquisition as described in Sects. 5.2 5.3.

5.2 Sample Fabrication and Structural Characterization

Thin films of bismuth and of gold were prepared. Thin films of bismuth were e-beam evaporated on nano-structured substrates or non-structured substrates at a rate of $2 \text{ \AA}\cdot\text{sec}^{-1}$ and a nominal final film thickness of 33–34 nm. Prior to bismuth deposition, chromium was evaporated in the chamber (but not allowed to deposit on the samples) to sequester oxygen, and to prevent the incorporation of oxides in the bismuth deposit. Thin films of gold were e-beam evaporated at a rate of $0.2 \text{ \AA}\cdot\text{sec}^{-1}$ to yield nominal final film thicknesses of 6 nm or 12 nm. The samples were handled in air, and were stored in a nitrogen box or a desiccator.

Three types of porous films were used as the nano-structured substrates:

1. Whatman filters (Anodisc13, Whatman International Ltd, nominal pore diameter: 200 nm). Note that the two surfaces of the Whatman filter are not identical in morphology, providing two types of surfaces: the porous surface and the “barrier layer”-type surface (see below).
2. Films obtained by the anodization of a thermally evaporated layer of aluminum on a thermally oxidized silicon wafer in an oxalic acid bath, as described in Chap. 3.
3. Silicon wafers patterned with a square array of inverted pyramids, obtained by interferometric lithography[164, 165] and anisotropic etching. These substrates were provided by Dr. Kornelius Nielsch and Prof. Caroline Ross (M.I.T.).

Glass cover slides (VWR Scientific) were used as the non-structured substrates. These serve as reference samples for comparison to the nano-structured substrates.

The bismuth and gold thin films were analyzed by scanning electron microscopy (SEM) and x-ray diffractometry (XRD).

The SEM images from the bismuth thin films deposited on glass, porous alumina, and patterned silicon substrates are shown in Figs. 5-4, 5-5, and 5-6, respectively.

In Figs. 5-4 and 5-5, the insets show low-magnification/large field-of-view images of the bismuth thin films on the substrates. The inset Fig. 5-6 shows the substrate *before* the e-beam evaporation of bismuth. The images show that the thin films are polycrystalline, with a grain size on the order of 100 nm. In the case of the nano-structured substrates (porous anodic alumina and silicon), the deposited film adopted the same microstructure as the underlying substrate, showing an array of nanopores with the same geometry as in the substrate. It is noted, that the pore diameters in the films are smaller than in the substrate as a result of material accumulation at the pore edges during the deposition. It is also expected that some amount of bismuth is lining the facets of the inverted pyramid indentations in the silicon substrate. The bismuth thin films on the Whatman filters have pores with 150–300-nm diameters, and constrictions of 70–200-nm in width. The bismuth thin films on the patterned silicon have pores with 95-nm diameters, and constrictions of 90–100-nm in width. Thin films on the “barrier-layer” surface of the Whatman filters with constrictions of 40-nm in width (Fig. 5-7) were obtained, but showed no detectable electrical conductivity. The gold thin films grown on the nano-structured substrates also reproduced the nano-structure of the underlying substrates, but were highly resistive. Gold films deposited on glass non-structured substrates were suitable for electrical characterization. Films evaporated on glass substrates will be referred to as *continuous films*, while films evaporated on nano-structured substrates will be referred to as *antidot array films*. The morphology of the two types of films is schematically presented in Fig. 5-8.

The XRD diffraction patterns from the bismuth 33 nm-thick thin films on glass, porous alumina, and patterned silicon are shown in Figs. 5-9(a)–(c), respectively. The glass substrate induces a preferred growth orientation of the crystals of the thin bismuth film perpendicular to the glass substrates. Only $(00l)$ diffraction peaks are observed. The porous anodic alumina substrate does not orient the growth of bismuth, and a powder diffraction pattern is obtained (at least 6 diffraction lines are discernible). The result from the bismuth film on the silicon substrate is interesting: two sets of planes are found parallel to the substrate, the $(00l)$ planes and the $(0k2k)$ planes. One hypothesis is that the silicon substrate also aligns the bismuth growth

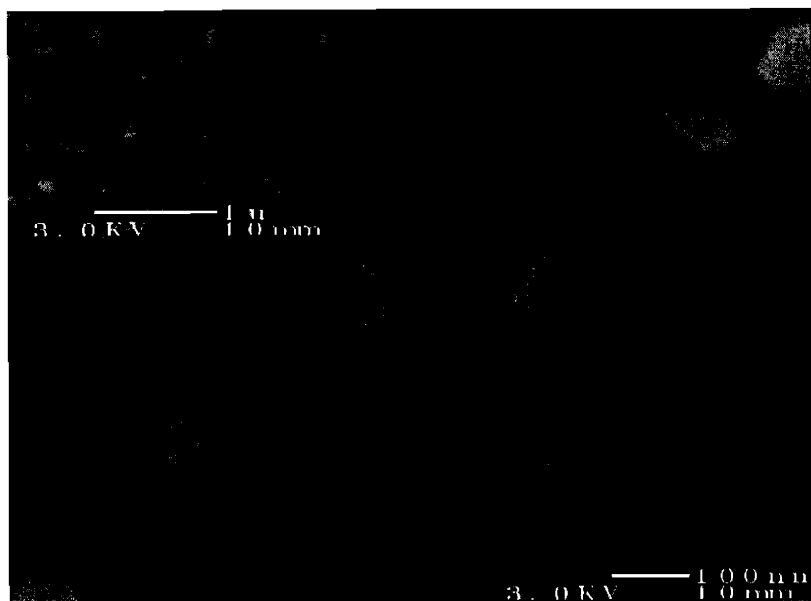


Figure 5-4: SEM image of the bismuth-coated glass slide. The inset shows a low-magnification image of the polycrystalline bismuth film.

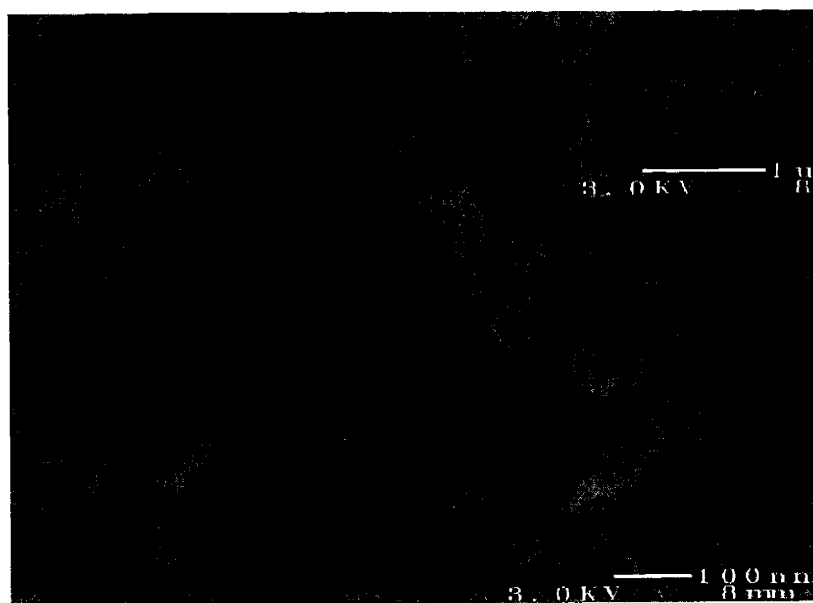


Figure 5-5: SEM image of the bismuth-coated Whatman filter. The inset shows a low-magnification image of the polycrystalline bismuth film.

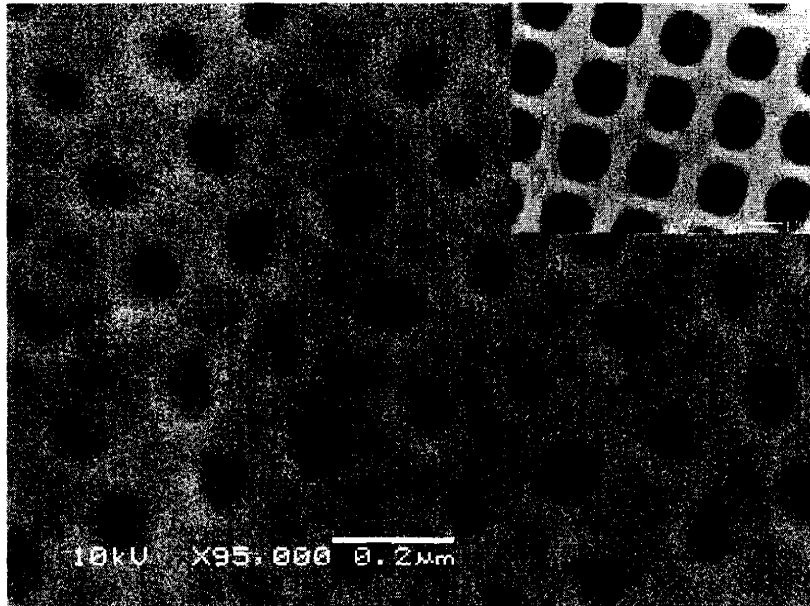


Figure 5-6: SEM image of the bismuth-coated silicon wafer patterned with an array of inverted pyramids. The inset shows the surface before the evaporation of bismuth.

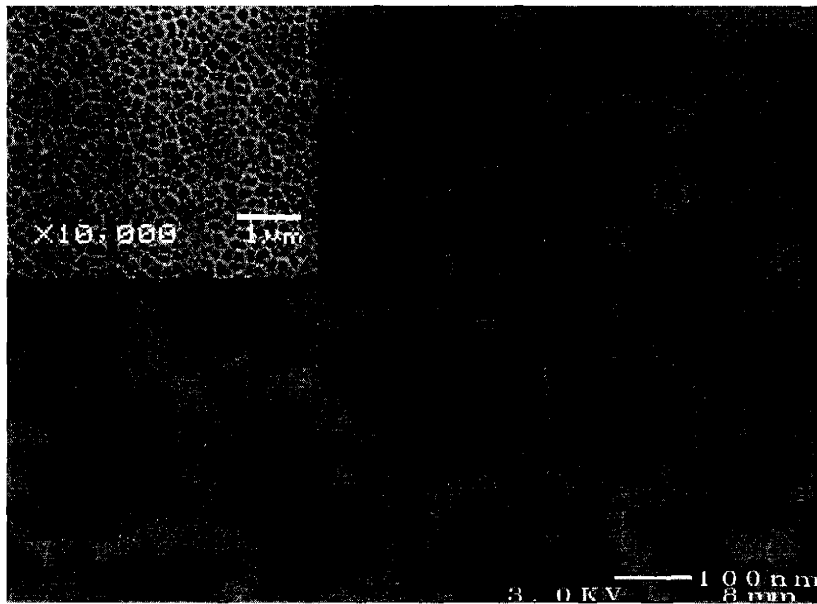


Figure 5-7: SEM image of the bismuth-coated barrier-layer surface of a Whatman filter. The inset shows a low-magnification image of the polycrystalline film.

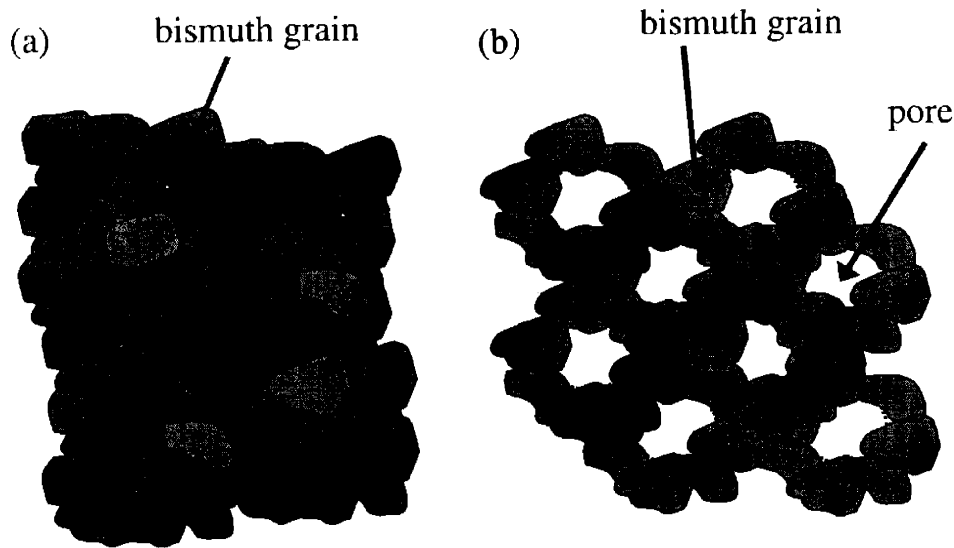


Figure 5-8: Schematic representation of the morphology of (a) a polycrystalline continuous film and (b) a polycrystalline antidot array film.

with the $(00l)$ planes parallel to the surface, and the signal for the $(0k2k)$ planes is obtained from bismuth deposited on the surfaces of the inverted pyramids. The peak lineshapes were analyzed to obtain an estimate of the crystal size in the perpendicular direction. The (012) peak width suggested a crystal size of 36.3 nm for the film on anodic alumina, and 38.5 nm for the film on silicon. The (003) peak width suggested a crystal size of 40.3 nm for the film on glass, 49.7 nm for the film on anodic alumina, and 47.7 nm for the film on silicon. The above values are similar to the nominal layer thickness of 33–34 nm obtained from the e-beam evaporator thickness monitor, but the values from the peak lineshape analysis over-estimate the film thickness. The main conclusion is that there are no grain boundaries in the direction perpendicular to the surface other than the film boundaries, and the bismuth crystals appear to have a flat-barrel shape (34 nm in height, 100 nm in diameter). In contrast, the XRD diffraction patterns from 6-nm thick gold thin films on glass and on porous alumina did not show a preferred crystal growth orientation. The grain size estimated from the peak lineshape was again similar to the film thickness.

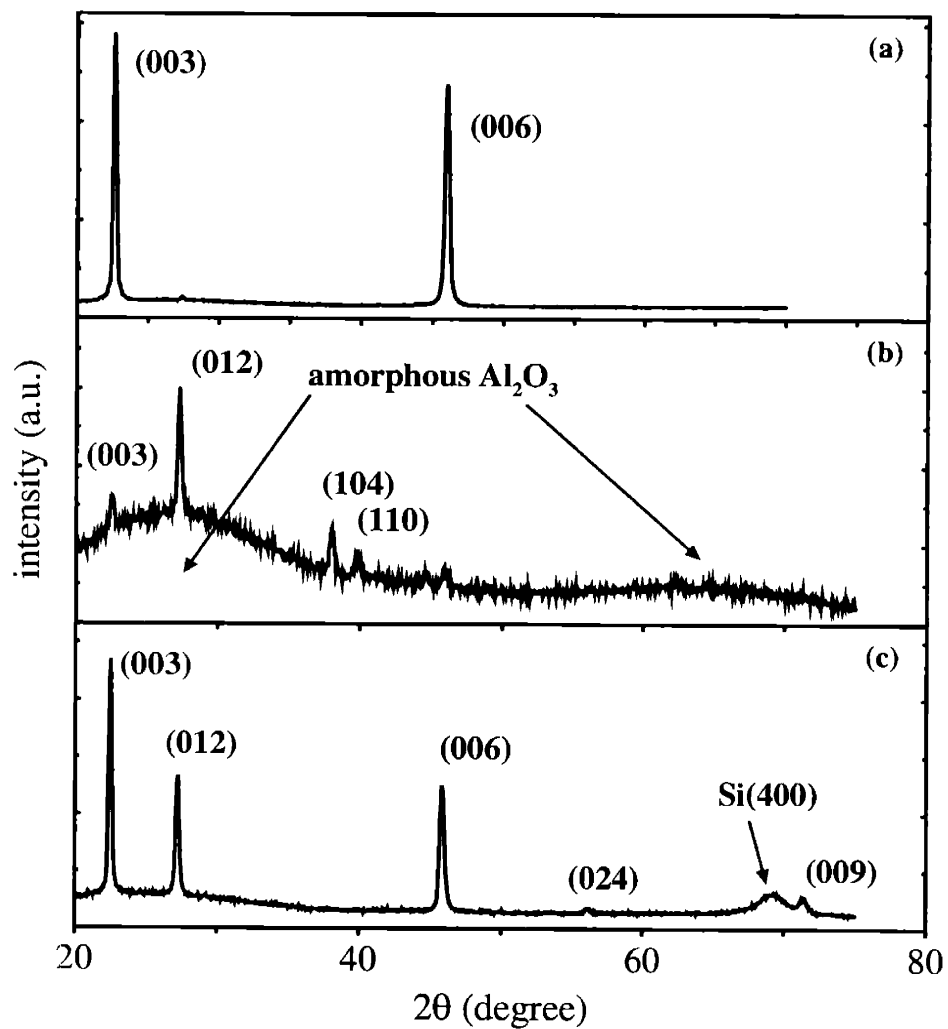


Figure 5-9: Diffraction patterns from 33-nm thick bismuth thin films deposited on (a) a glass cover slide, (b) a Whatman filter (porous anodic alumina), and (c) a silicon wafer patterned with an array of inverted pyramids. All the peaks correspond to diffractions lines from bulk bismuth, except where indicated.

5.3 Electrical Characterization

Measurements of the electrical properties of the continuous and the antidot array films were carried out in collaboration with Dr. J. S. Moodera and Dr. A. Thomas (Magnet Lab, M.I.T.). The measurements were conducted with a commercial Magnetic Property Measurement System SQUID magnetometer (MPMS-5, Quantum Design) equipped with a Manual Insertion Utility Probe for transverse magnetoresistance measurements, operating at 2–300 K and 0–5 Tesla, or with a custom-built ^3He probe and a superconducting magnet for measurements at lower temperatures, 0.45–4.18 K, and with a magnetic field of 0–7 Tesla applied parallel or perpendicular to the film surface. Longitudinal (field parallel to current) and transverse (field perpendicular to surface) magnetoresistance of the films were measured in a 4-probe configuration, and Hall effect measurements were carried out in a 6-probe configuration, on films with a nearly rectangular geometry.

5.3.1 Temperature Dependence of the Magnetoresistance of the Films

The theory of two-dimensional (2D) weak localization predicts a correction to the film conductance

$$\Delta G = -\frac{\Delta R}{R^2} = -\frac{e^2}{2\pi^2\hbar} \ln(\tau_i/\tau_0) \quad , \quad (5.1)$$

where τ_i and τ_0 are the inelastic and elastic scattering lifetimes of the electrons, respectively.[163] Since τ_i depends on temperature as T^{-p} (p is a positive constant) and τ_0 can be regarded as temperature independent, the dependence of the film conductance on temperature should bear a signature of weak localization, and should provide a value for p . For 2D weak localization $\Delta G/\ln(T) > 0$, but for 2D weak anti-localization $\Delta G(T)$ has an additional factor of (-0.5) , so that $\Delta G/\ln(T) < 0$.

Figure 5-10 presents the temperature dependence of the normalized resistance of 33 nm thick bismuth films on various substrates (one continuous film and three antidot array films), while Fig. 5-11 presents the temperature-dependent resistance of

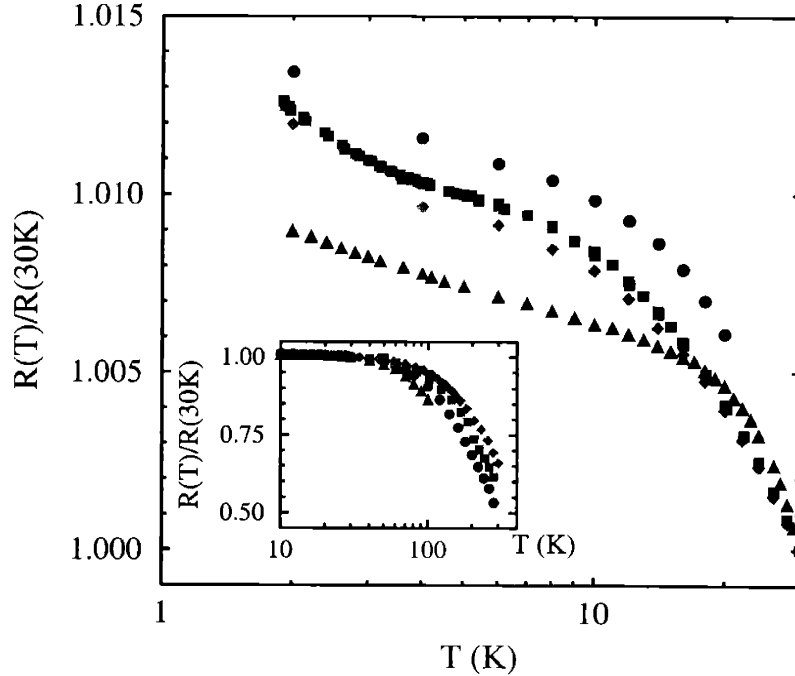


Figure 5-10: Temperature dependence of the resistance, normalized to the resistance at 30 K, of 33-nm thick bismuth films on various substrates: (●) patterned silicon, (■) Whatman filter, (◆) PAA on an oxidized wafer, and (▲) glass (continuous). The inset shows data for temperatures up to 300 K.

a 6 nm thick continuous gold film, with no magnetic field applied. For both materials, Figs. 5-10 and 5-11 show that the resistance (R) decreases with temperature in the temperature range relevant to weak localization. For continuous films, ΔR is proportional to $-\ln(T)$. For antidot array films, $\Delta R(T)$ is seen to be more complex. Both materials have strong spin-orbit coupling, so that weak anti-localization effects are expected to occur. The observed behavior is, however, opposite in sign to the predictions for weak anti-localization. This discrepancy was observed previously[163, 166–169], and was explained in terms of the dominance of electron-electron interactions in the temperature dependence of the resistance in the low temperature-range where localization effects are relevant.

To get more insight into the localization effects in the thin films, magnetoresistance studies were carried out. Figure 5-12 presents the temperature dependence of the

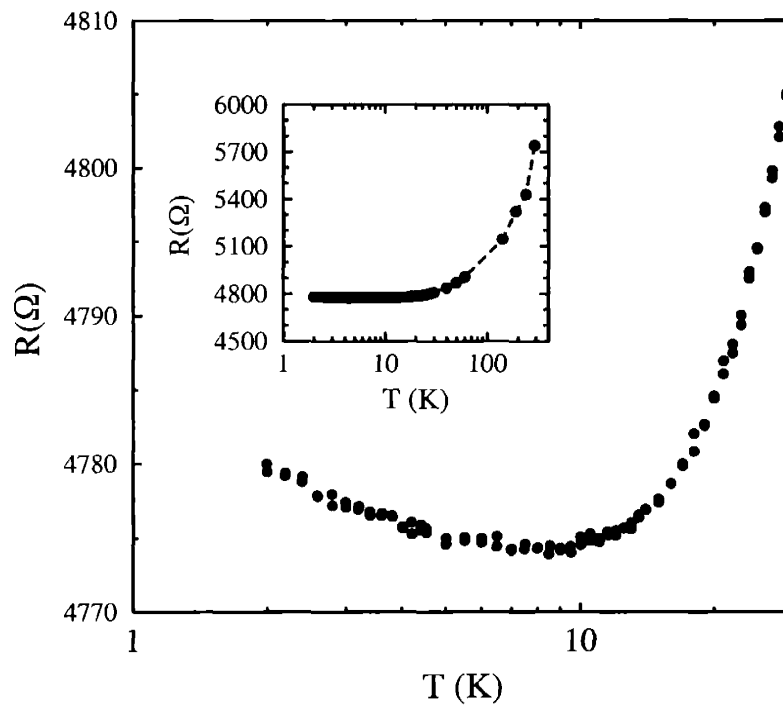


Figure 5-11: Temperature dependence of the resistance of a 6-nm thick continuous gold film on a glass substrate ($2\text{ K} < T < 30\text{ K}$). The inset shows data for temperatures up to 270 K.

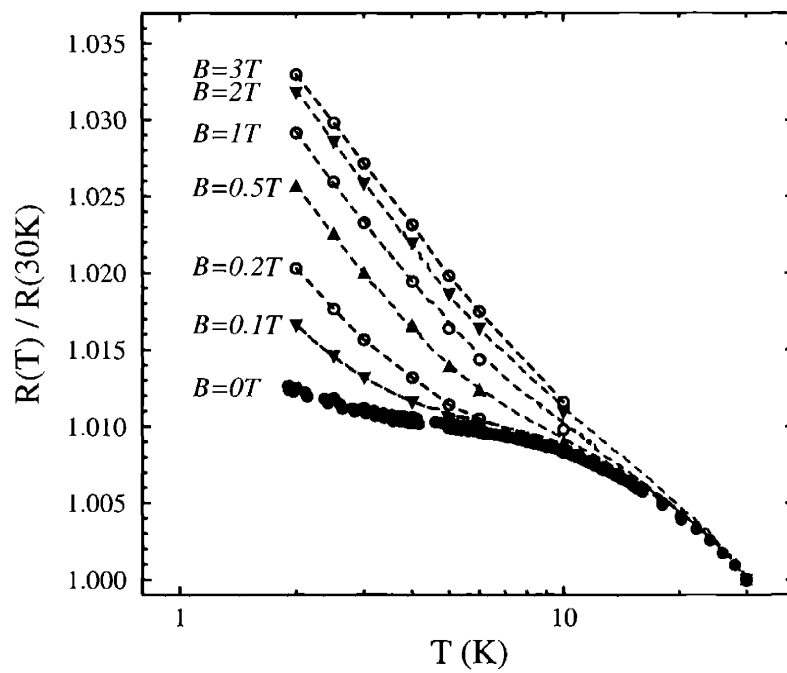


Figure 5-12: Temperature dependence of the resistance, normalized to the resistance at 30 K, of a 33-nm thick bismuth film on a Whatman filter, at various magnetic field strengths.

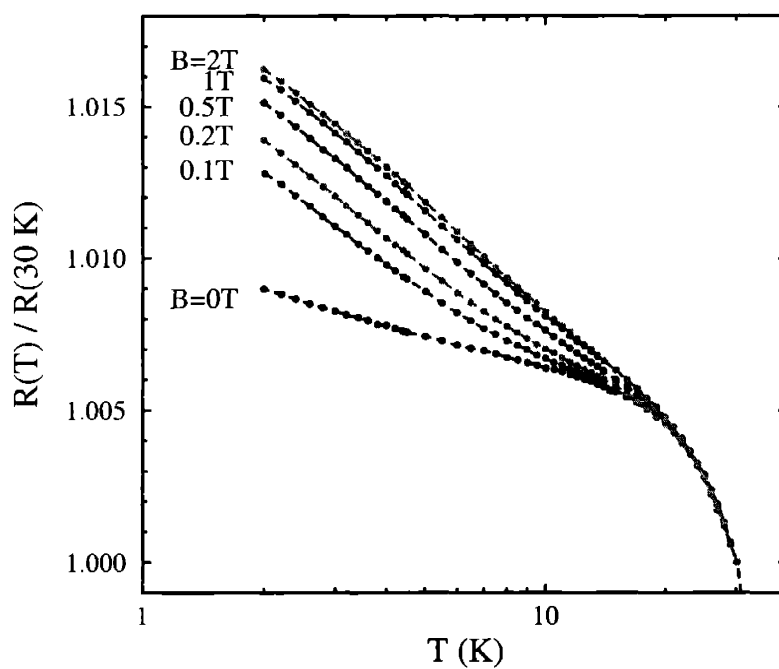


Figure 5-13: Temperature dependence of the resistance, normalized to the resistance at 30 K, of a 33-nm thick bismuth film on a glass cover slide, at various magnetic field strengths.

normalized resistance of a 33 nm thick antidot array bismuth film with a magnetic field applied perpendicular to the film, while Fig. 5-13 shows the corresponding data for a continuous bismuth film. The measurements show that the magnetic field increases the film resistance, as expected from the weak anti-localization effect and from the classical magnetoresistance effect in bismuth. Interestingly, at high magnetic field the lineshape of the curve of resistance *vs.* $\ln(T)$ is linear in the low temperature region, as is also observed for continuous films. Both the temperature dependence and the magnetic field dependence of the normalized resistance are more pronounced in the antidot array film than in the continuous film.

The temperature dependence studies indicate that both electron-electron interactions and weak anti-localization effects are relevant to the transport in the thin films. The weak anti-localization effect thus is studied through the analysis of the magnetoresistance, since the electron-electron interaction is not affected by the external magnetic field.

5.3.2 Low-Temperature ($0.45 \leq T \leq 4.2$ K) Magnetoresistance Measurements with the ^3He Setup

The transverse magnetoresistance of continuous and antidot array bismuth films, 33 nm in thickness, was recorded at several temperatures in the range of 0.45–4.2 K (1.3 K, 1.8 K, 2 K, and 4.2 K for the antidot film and 0.45 K and 1.8 K for the continuous film) and magnetic fields up to 7 Tesla. The results for a Whatman filter substrate are shown in Fig. 5-14. The results for a glass substrate are shown in Fig. 5-15. The oscillations observed in the data are an artifact originating from the current-loading mechanism of the superconducting magnet, and their oscillation period changes with the ramping rate of the magnetic field strength. Indicated in the figures by a vertical dashed line is the magnetic field at which the magnetic length $L_H = \sqrt{\hbar/4eB}$ equals the film thickness of 33 nm.

Comparison between the two sets of results again shows that the weak anti-localization effect is more dominant in the antidot array film than in the continu-

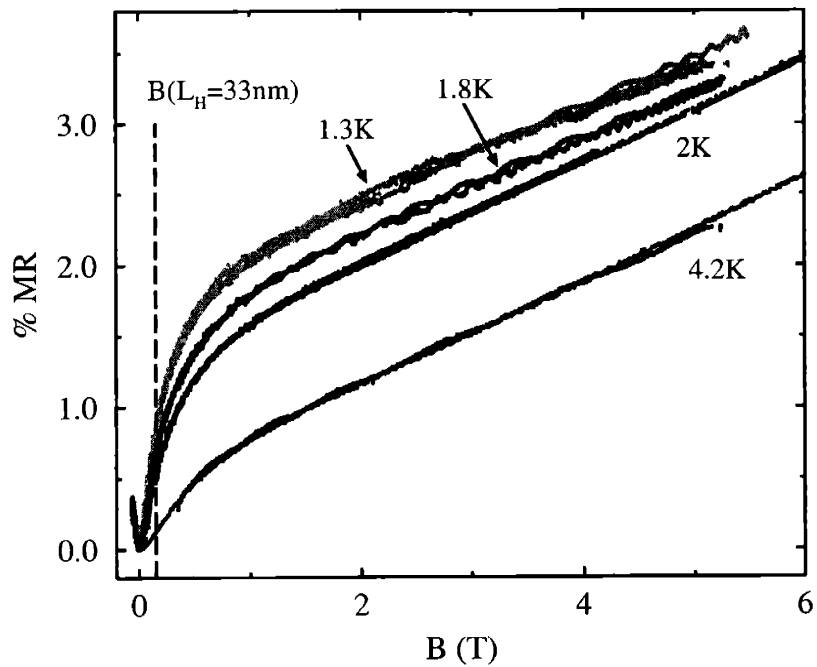


Figure 5-14: Transverse magnetoresistance of a 33-nm thick antidot array bismuth film on a Whatman filter substrate at various operating temperatures. The vertical dashed line corresponds to the field strength at which the magnetic length is equal to the nominal film thickness.

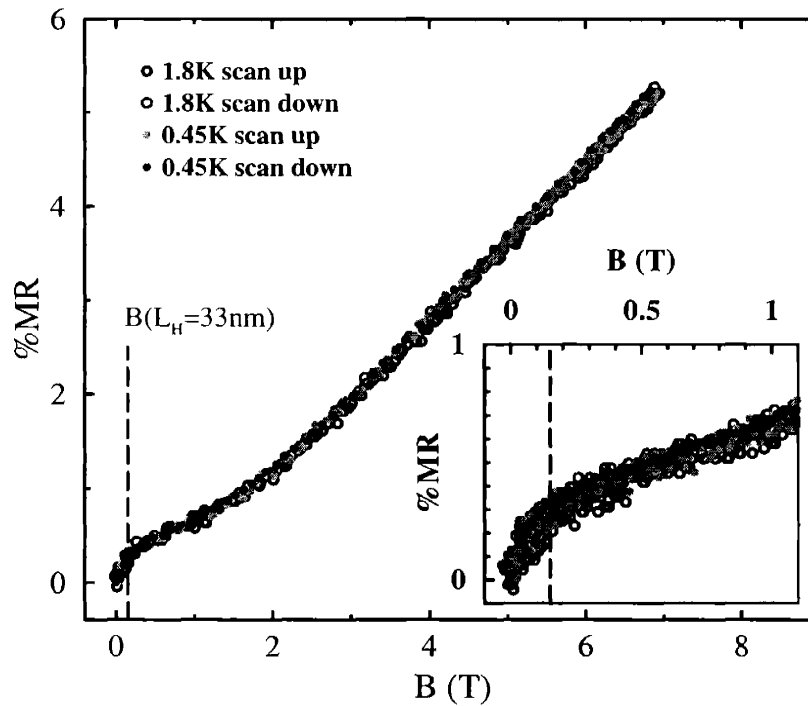


Figure 5-15: Transverse magnetoresistance of a 33-nm thick continuous bismuth film on a glass substrate at two operating temperatures. The vertical dashed line corresponds to the field strength at which the magnetic length is equal to the nominal film thickness. The inset is a magnification of the low-field region.

ous film. For instance, at 1.8 K and 1 Tesla, a magnetoresistance of only 0.5% is observed in the continuous film, while a magnetoresistance of 1.75% was recorded for the antidot array film. Moreover, there is little temperature dependence in the magnetoresistance of the continuous film between 0.45 K and 1.8 K, while the antidot array film shows a clear temperature dependence of the magnetoresistance at low magnetic field strengths. At large magnetic fields, where classical effects dominate the magnetoresistance, there is no significant temperature dependence (i.e. the curves become parallel). Since the maximum temperature of operation of the ^3He probe-electromagnet setup is 4.2 K, no measurements could be made at temperatures in which the weak anti-localization is negligible ($T > 15$ K). As a result, an estimation of the relative contributions of the classical and the weak anti-localization effects to the magnetoresistance could not be made. Without a good estimate for these relative contributions, quantitative lineshape analyses of the magnetoresistance curves, that provide information regarding the different scattering rates in the films, could not be made. There is no noticeable anomaly in the longitudinal or transverse magnetoresistance data at $L_H = 33$ nm ($B = 0.15$ Tesla). This value corresponds to a single fluxon fitting in the thickness of the film, and is material independent. Such anomalies have been observed in bismuth nanowires.[170] Lower values of the magnetic field below the measurement resolution (60–100 mTesla) correspond to a fluxon fitting in the rings formed around the pores or in a bismuth constriction between pores. A sharp change in slope in the magnetoresistance was only observed in the low temperature data from continuous bismuth films (see Fig. 5-16) at 200–350 mTesla, which, as will be shown here, might correspond to the elastic scattering rate of the carriers. It is not likely that the knee at ~ 300 mTesla indicates that the true film thickness was reduced to 23 nm (due to oxidation, for example).

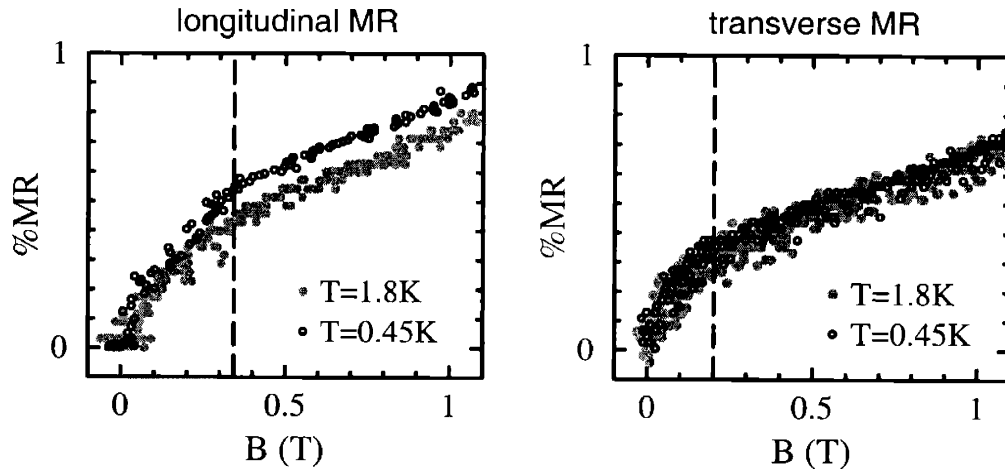


Figure 5-16: (a) Longitudinal magnetoresistance and (b) transverse magnetoresistance of a 33-nm thick continuous bismuth film on a glass substrate, showing a change in slope at 340 and 200 mTesla, respectively.

5.3.3 Low-Temperature ($2\text{ K} \leq T \leq 30\text{ K}$) Magnetoresistance Measurements with the MPMS Magnetometer Setup

The transverse magnetoresistance of continuous and antidot array bismuth films, 33 nm in thickness, was recorded in the temperature range of 2–30 K and in magnetic fields up to 5 Tesla. The results for an antidot array bismuth film on a Whatman filter substrate are shown in Fig. 5-17. The results for an antidot array bismuth film on a patterned silicon substrate are shown in Fig. 5-18. The results for a continuous bismuth film on a glass substrate are shown in Figs. 5-19.¹

Comparison between the two sets of results again shows that the weak anti-localization effect is more dominant in the antidot array film than in the continuous film. Moreover, the temperature dependence in the magnetoresistance of the continuous film is weak, while the antidot array film shows a more pronounced tem-

¹Aging affects the electrical properties of the bismuth film in two ways: the resistivity of the film increases, indicative of the progression of ambient oxidation, and the magnetoresistance of the film also increases, indicating that annealing occurs at room temperature and the mobility increases with time.

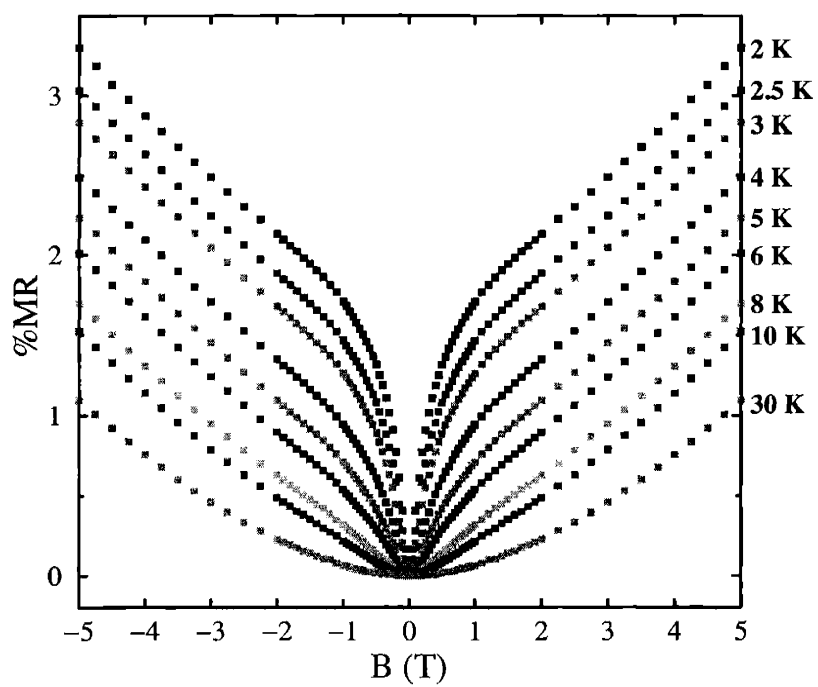


Figure 5-17: Transverse magnetoresistance of a 33-nm thick antidot array bismuth film on a Whatman filter substrate at various operating temperatures.

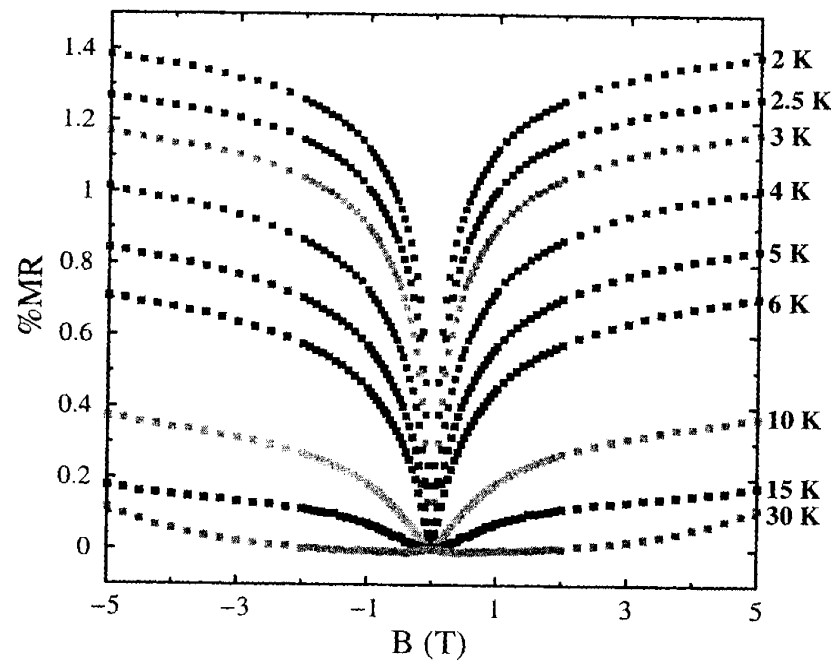


Figure 5-18: Transverse magnetoresistance of a 33-nm thick antidot array bismuth film on a silicon substrate at various operating temperatures.

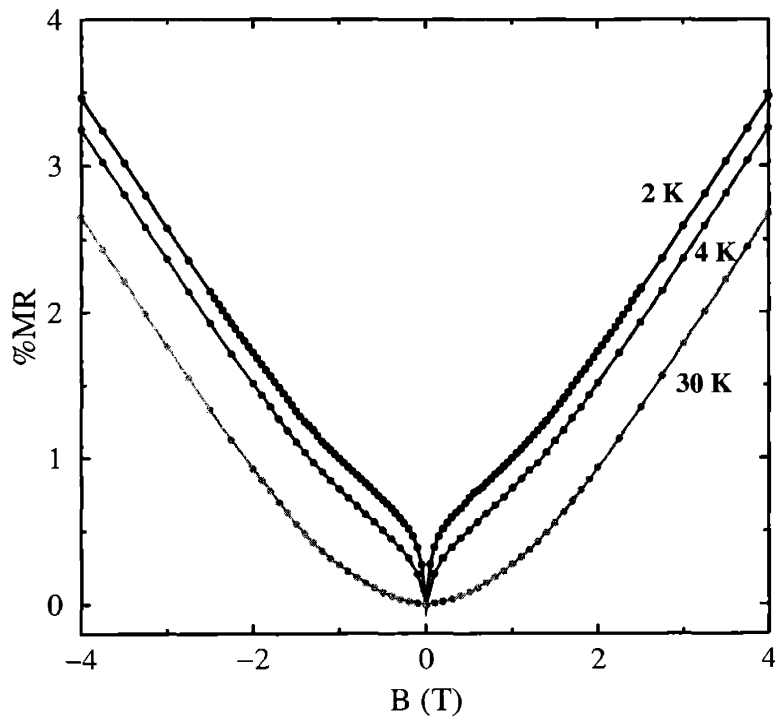
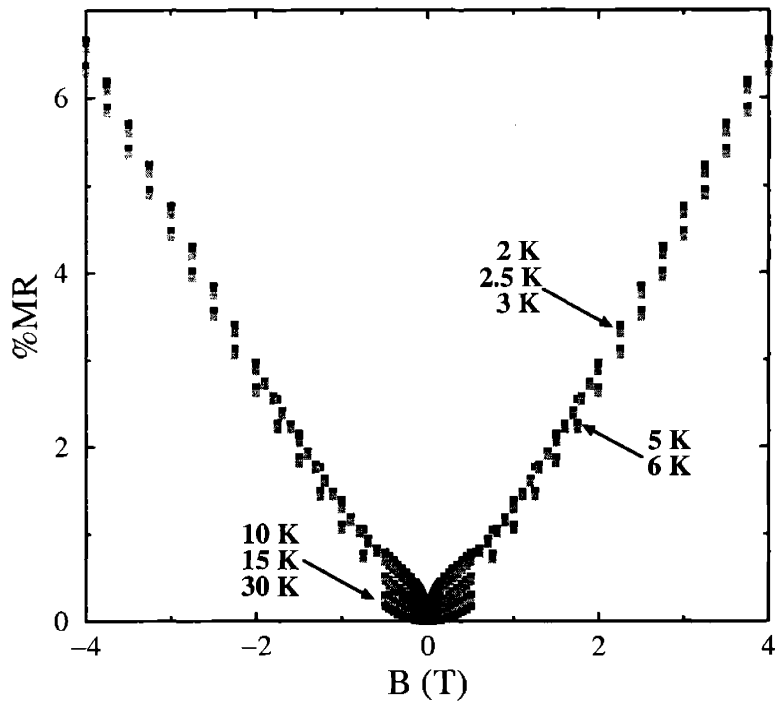


Figure 5-19: Transverse magnetoresistance of a 33-nm thick continuous bismuth film on a glass substrate at various operating temperatures. The lower set of results was obtained from the same sample two months earlier.

perature dependence of the magnetoresistance at low magnetic field strengths. At large magnetic fields, where classical effects dominate the magnetoresistance, there is no significant temperature dependence in any of the data sets (i.e. the curves become parallel). The slope of the curves at large fields is larger for the continuous films, indicating that the carrier mobility is higher in these samples. This is understood in terms of the superior crystal quality of the continuous samples grown on glass, in which the carriers follow parallel to the (001) planes. In the antidot array films, the carrier trajectories are interrupted by the pores, and by the higher misorientation of the bismuth crystallites. Furthermore, the glass surface is flat, while the anodic alumina surface is rough on the nanometer scale.

The results were analyzed according to the weak localization theory predictions [162, 163] to obtain the effective scattering rates of the carriers in the films. The correction to the conductivity $\Delta G(B)$ due the weak anti-localization (relative to a hypothetical sample with no weak localization) is given by

$$\Delta G(B) = -\frac{e^2 A}{2\pi^2 \hbar} \left[\Psi\left(\frac{1}{2} + \frac{H_1}{B}\right) - \frac{3}{2} \Psi\left(\frac{1}{2} + \frac{H_2}{B}\right) + \frac{1}{2} \Psi\left(\frac{1}{2} + \frac{H_3}{B}\right) \right], \quad (5.2)$$

where A is a constant factor related to the geometry of the film, Ψ is the Digamma function, and H_1, H_2, H_3 are scattering fields given by (assuming no magnetic scattering):

$$H_1 = H_0 + H_{so} \quad , \quad (5.3)$$

$$H_2 = H_i + \frac{4}{3} H_{so} \quad , \quad (5.4)$$

$$H_3 = H_i \quad . \quad (5.5)$$

Here the indexes (subscripts) stand for the following scattering processes: 0 – elastic scattering; i – inelastic scattering; so – spin-orbit scattering. The scattering fields H_x are related to the scattering rate constants τ_x through the carrier diffusion constant $D = v_F^2 \tau_{eff} / 2$ by

$$H_x \cdot \tau_x = \frac{\hbar}{4eD} \quad . \quad (5.6)$$

In many materials the main contribution to the magnetoresistance is from the weak localization effects (see, for example, our measurements on gold in Fig. 5-3),

but in bismuth the large carrier mobilities, the large anisotropy of the carrier effective mass, and the substantial non-parabolicity in the $E(\mathbf{k})$ dispersion relation, lead to large classical magnetoresistance effects. Thus, for the analysis by Eq. 5.2, it is necessary to approximate the magnetoresistance curve baseline which includes the classical effect but not the localization effect. For this purpose it was assumed that the experimental magnetoresistance curve at 30 K does not contain localization contributions. However, the resistance of bismuth and the classical magnetoresistance are also temperature dependent, so the $T=30$ K curve cannot be used as a baseline for any other temperature without modifications. The functional shape of the magnetoresistance baseline curve was defined as a second degree polynomial, but different coefficients of the polynomial were chosen for the low-field range ($B=0-0.5$ Tesla), in which the magnetoresistance is approximately parabolic with respect to the field, and the high-field range ($B=2-5$ Tesla), in which the magnetoresistance is approximately linear with respect to the field. The high field coefficients were found by a least-squares fit to the experimental data, as it is assumed that no contribution of localization remains at high fields. The low-field coefficients were found for the 30 K data by a least-squares fit, and for the 2 K data (the lowest temperature of measurement) by factoring the 30 K fitted curve so that the curve fits the 2 K high-field data. The low-field coefficients for the intermediate temperatures (2.5–10 K) data were obtained by assuming the magnetoresistance coefficient (α in $R(B)=R_0 + \alpha B^2$) depends on temperature as T^{-2} , as was previously reported for single crystal bismuth in the temperature range $T=4-16$ K[159]; however, for the silicon substrate the magnetoresistance coefficient α was found to be practically temperature independent. The transition between the two sets of parameter was smoothed by hyperbolic tangent functions in the form:

$$\begin{aligned}
R(B, T)_{baseline} = & \left(\frac{1}{2} - \frac{1}{2} \tanh\left(\frac{x - x_0}{r}\right) \right) * (R_0(T) + \alpha(T)B^2) \\
& + \left(\frac{1}{2} + \frac{1}{2} \tanh\left(\frac{x - x_0}{r}\right) \right) * (c_1(T) + c_2(T) * B + c_3(T) * B^2) \quad , \\
\end{aligned} \tag{5.7}$$

where x_0 is the transition point, r is the transition width, and $\{c_1, c_2, c_3\}$ are the high-field second-order polynomial coefficients. In order to fit the experimental results

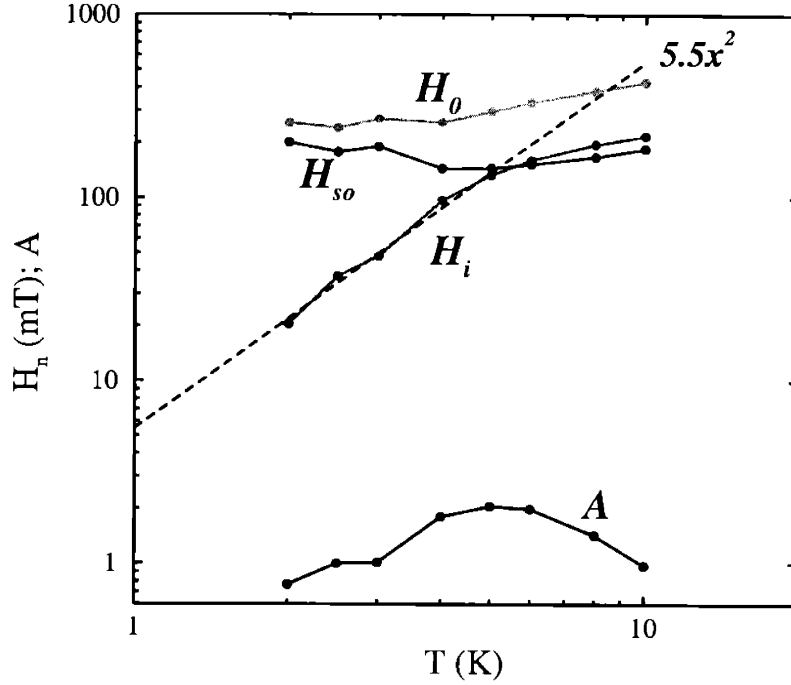


Figure 5-20: Log-log plot of the temperature dependence of the fitted scattering field values H_i , H_0 , and H_{so} and of the value of fitting parameter A for the magnetoresistance data from a Whatman supported antidot array thin bismuth film. The dashed line is the best fit of the temperature dependence of the values for H_i to a power law T^p .

to Eq. 5.2, the experimental $\Delta G(B)$ at a given temperature was calculated as the difference

$$\Delta G(B, T)_{exp} = \frac{1}{R(B, T)_{exp}} - \frac{1}{R(B, T)_{baseline}} \quad (5.8)$$

The fit was carried out by repeatedly adjusting the values of A , H_0 , H_i , and H_{so} in Eq. 5.2, to reduce the square-differences between the ΔG_{exp} data points from Eq. 5.8 and the values calculated by Eq. 5.2.

Figures 5-20, 5-21 and 5-22 show the fitted values of A , H_0 , H_i , and H_{so} thus obtained as a function of temperature for a bismuth antidot array film on alumina and on silicon, and a continuous film on glass, respectively.

The fitted values for the coefficient A , which were expected to be constant and

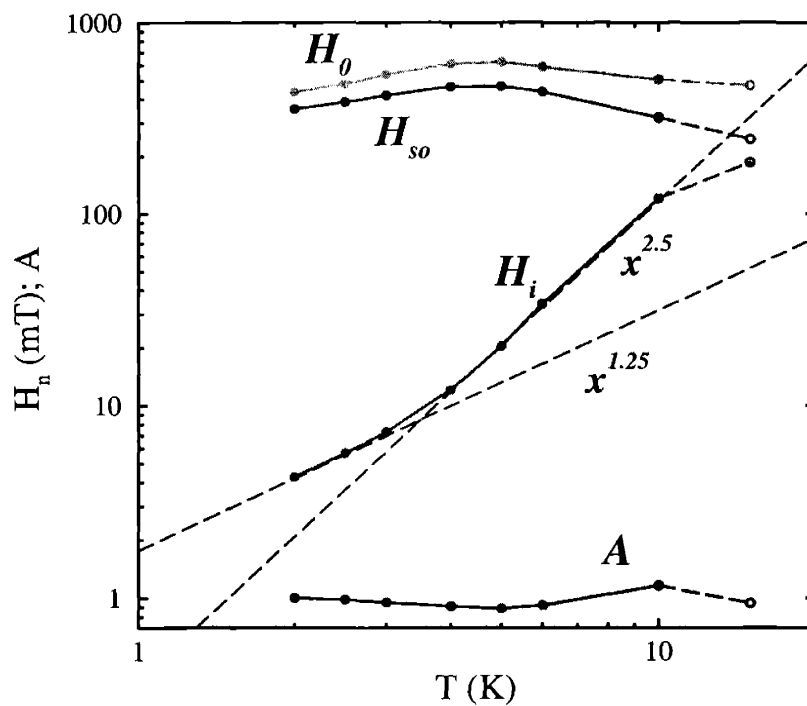


Figure 5-21: Log-log plot of the temperature dependence of the fitted scattering field values H_i , H_0 , and H_{so} and of the value of fitting parameter A for the magnetoresistance data from an antidot array thin bismuth film on a patterned silicon substrate. The dashed lines are fits of the temperature dependence of the values for H_i to a power law T^p .

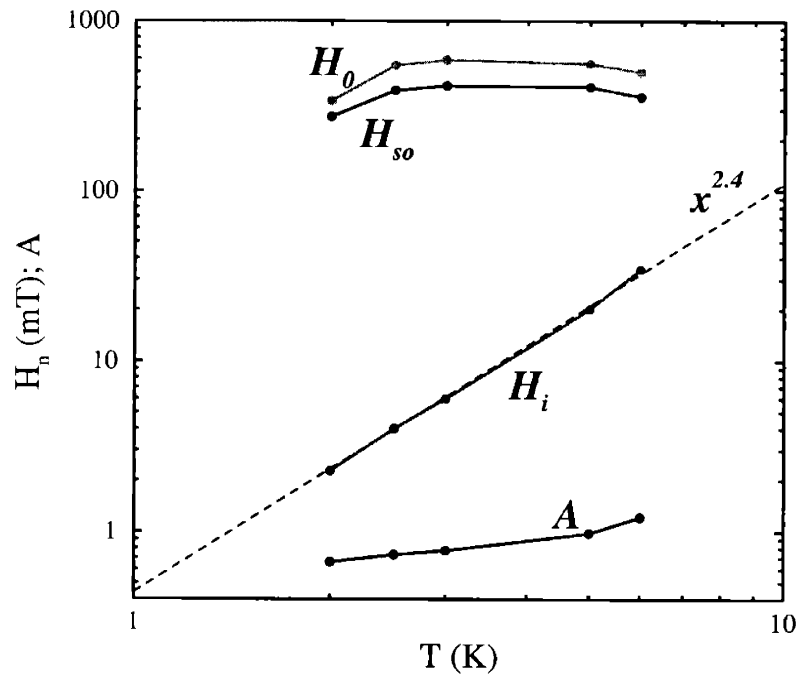


Figure 5-22: Log-log plot of the temperature dependence of the fitted scattering field values H_i , H_0 , and H_{so} and of the value of fitting parameter A for the magnetoresistance data from a glass supported continuous thin bismuth film. The dashed line is the best fit of the temperature dependence of the values for H_i to a power law T^p .

equal to the sample's width-to-length ratio (1 ± 0.2 for the samples analyzed here), are in relatively good agreement with that expectation. The values for H_0 and H_{so} are practically temperature independent, again in good agreement with the expectations. The fitted values of H_i show a clear temperature dependence, which was approximated as T^2 for the antidot array film on the Whatman substrate, and as $T^{2.4}$ for the continuous film. In the case of the antidot array film on silicon, the temperature dependence of H_i does not follow a simple power-law. At high temperatures ($4 < T < 10$ K) the behavior was approximated as $T^{2.5}$, while at lower temperatures the power is smaller than 1.25. When the value of H_i reaches 150 mTesla at high temperatures, a strong deviation from the power law describing the low temperature behavior is observed. This deviation is attributed to the transition from a two-dimensional to a three-dimensional weak anti-localization system, as the phase-breaking length, L_ϕ given by

$$L_\phi = \sqrt{\frac{\hbar}{4eH_\phi}} \approx \sqrt{\frac{\hbar}{4eH_i}} \quad , \quad (5.9)$$

becomes comparable to the film thickness of 33 nm. In the three-dimensional weak anti-localization regime, Eq. 5.2 is no longer applicable. Also, as the temperature increases, and the inelastic scattering rate becomes comparable with the other scattering processes, the weak anti-localization contribution to the magnetoresistance diminishes and the significance of the fitted values becomes questionable. The values of H_i for the different samples are in accordance with the experimental values of the sheet resistivities: The lowest sheet resistivity of 476Ω was measured for the film on the glass substrate, for which H_i at 2 K has the value of 2 mTesla. The film on silicon had a sheet resistivity of 549Ω and H_i of 4 mTesla. The highest sheet resistivity was recorded for the film on the Whatman substrate (1921Ω) with H_i values starting at 20 mTesla. Thus, the fitting procedure correctly assigned higher inelastic scattering rates to the more resistive films. The values of the other scattering fields do not change as much from sample to sample, although the average value of H_0 and H_{so} for the film on the Whatman substrate were lower by a factor of 2 compared to the other samples.

Earlier works on the weak anti-localization effect in bismuth thin films have also investigated the temperature dependence of H_i , or τ_i . Beutler and Giordano[163] reported that $\tau_i(T)$ is proportional to T^{-p} , where $p=1.45\pm 0.1$ at $T=0.1-5$ K. Komori *et al.*[167] found $\tau_i(T)$ is proportional to T^{-1} below 1 K and to T^{-2} between 2–10 K. However, from their conductivity *vs.* temperature analysis, both works obtained $p \approx 1$. Woerlee *et al.*[171] obtained from the magnetoresistance analysis an increase in the power value, from 0.7 at 0.1 K to 1.8 at 4.2 K. White and McLachlan[169] also obtained that $\tau_i(T)$ is proportional to T^{-1} and T^{-2} , except that they determined the cross-over temperature to be 3 K. Interestingly, for films evaporated on heated substrates (323 K) they reported a single power law of $\tau_i(T) = T^{-1.5}$ for the entire temperature range of 1.4–15 K.

The observed temperature dependence effects in our films are explained by considering the various possible electron scattering mechanisms in the films and their temperature dependence. The inelastic electron-electron scattering (for non-interacting electrons) is proportional to kT^2/ε_F . [172] However, it can be lower in disordered systems ($T^{1.5}$ in 3-D, $T^{\sim 1}$ in 2-D). [173] The inelastic electron-phonon scattering is proportional to T^3 in 3-D below the Debye temperature, but might change to T^2 in a 2-D system. [174] The electron-electron interaction gives rise to a $\ln(T)$ dependence of the conductivity, with a prefactor showing a magnetic field dependence [175]. This factor, however, was not taken into account by Eq. 5.2. Thus, it has been suggested that the results of the analysis of the weak anti-localization effect in the magnetoresistance describe a transition in the dominant scattering mechanism in bismuth films, from an inelastic electron-electron scattering mechanism proportional to T^{-1} to an electron-phonon scattering mechanism proportional to T^{-2} or T^{-3} , at higher temperatures. It is interesting to note that the mobilities in bismuth depend on temperature as T^{-2} in this temperature range ($T=4-16$ K) [159], but the correlation between mobilities and scattering rates (i.e. between mean-free path and phase-coherence length) is not straight forward because small-angle scattering is prevalent at low temperatures. [174] Due to possible errors associated with the fitting procedure and to the narrow temperature window available for the measurements (2–10 K), it is risky to

speculate whether real differences exist in the temperature dependence of the inelastic scattering processes in films with different morphologies. The more disordered nature of the film on the Whatman substrate might be the reason for the lower value of the power p in T^{-p} observed in this sample. Hall measurements also suggest a modest reduction in the carrier density in this film compared to the film grown on glass. This difference would shift the cross-over temperature to higher values.

One possible explanation for the enhancement of the weak localization effect in the antidot array films compared to the continuous films is the selective enhancement of the elastic scattering rate over the inelastic scattering rate in the antidot array films. The antidot morphology could alter the scattering rates in that fashion, since it introduces a “hard-wall” scattering potential at the bismuth-pore interfaces in addition to the weak, fluctuating potential due to grain boundaries in the films. A larger H_0/H_i ratio in the antidot films would result in a larger magnetoresistance correction $\Delta G(B)$. However, the above analysis of the experimental results does not seem to indicate such an increase in the H_0/H_i ratio.

It was found, however, that the fitted results depend significantly on the details of the baseline and the fitting procedure that were chosen. In particular, the values of H_{so} and H_0 appeared to have a relatively weak effect on the convergence of the fitting procedure. Thus the error in these values is expected to be high. Significantly different values for H_i were obtained depending on the values set for $R_0(T)$ and $\alpha(T)$. There was no rigorous method to improve the estimate of these two low-field parameters.

Finally, fits were carried out simultaneously for curves obtained from an individual sample at different temperatures. For each sample, the values of $A = w/L$ and $\varepsilon = H_{so}/H_0$ [176, 177] were set to be temperature independent. The values of $\Delta G(B, T)_{exp}$ were set to zero at high fields, as an additional constraint to improve the fits. By this procedure, smaller ranges of temperature could be properly fitted to Eq. 5.2 as compared to the results shown in the previous figures, where A and ε were allowed to be temperature dependent, because of the lower number of degrees of freedom ($2n+2$ parameters *vs.* $4n$, where n is the number of curves to be fitted). The inability of

the simultaneous-fitting procedure to account for the higher temperature results, in most cases, was related to the transition to a three-dimensional localization regime and to the breakdown of the condition $H_i \ll H_{so}, H_0$. In few other cases, the false results from the fitting indicated improper background subtraction. The parameters obtained from the simultaneous-fitting are presented in Table 5.1. The simultaneous-curve fitting differs significantly from the individual-curve fitting in the temperature dependence of H_i (except for the case of the sample on the silicon substrate). The calculated values for A are again close to the experimental values. The ratio H_{so}/H_0 , which corresponds to the efficiency of momentum-scattering events to scatter spin, and is estimated to be equal to 0.5–1 for bismuth[177], was found to be uniform across the samples. This, together with the values calculated for the elastic scattering rates, indicates that the carrier scattering in the bulk of the material is the dominant scattering mechanism regardless of morphology, and the porous structure does not play a significant role. It is estimated that the constrictions between the pores need to be reduced below 20 nm in width for the porous structure to alter the elastic scattering rate. The morphology did affect the inelastic scattering rate, and correspondingly the films on a porous anodic alumina substrate show a lower sheet conductivity.

One condition that was not obeyed in our fitting procedure is that the magnetic length $L_H = \sqrt{\hbar/4eB}$ should be larger than the film thickness. This condition restricts the analysis to data from magnetic fields below 0.15 Tesla. However, we see in the data that the weak-localization effect is significant at much higher values of magnetic field strengths. While the condition of two-dimensionality of the films with respect to the coherence length L_ϕ was taken into account (Eq. 5.9), a second coherence length results from the inclusion of spin-orbit interactions[178]

$$L_{\phi 2} = \sqrt{\frac{\hbar}{4e(H_i + 4H_{so}/3)}} \quad , \quad (5.10)$$

which for our samples is at most ~ 24 nm. Therefore, for some coherence processes involving spin-orbit scattering, our samples lay in the three-dimensional regime, which might require a modified version of Eq. 5.2 for mixed-dimensional systems.[178] The theoretical development of these corrections is beyond the scope of this work.

Table 5.1: Transport parameters obtained from the analysis of the magnetoresistance measurements of 33-nm bismuth films in terms of the weak anti-localization effect.

properties	continuous film on glass	antidot array film on porous alumina	antidot array film on patterned silicon
G_{sq} (exp. T=30 K) [$10^{-3} \Omega^{-1}$]	2.1	0.52	1.82
H_0 (calc.) [Tesla]	0.24–0.52	0.25–0.41	0.45
H_{so} (calc.) [Tesla]	0.19–0.42	0.19–0.32	0.37
$\varepsilon = H_{so}/H_0$	0.808	0.77	0.815
A (exp.)	1	0.8 ± 0.1	1
A (calc.)	0.82	0.69	0.985
$p = \frac{\partial \ln(H_i)}{\partial \ln(T)}$ (calc.)	1.22	1.35 ± 0.15	varies (1.6–2.6)
H_i (calc. T=2 K) [Tesla]	0.005	0.019	0.004
valid temp. range [K]	2–6	2–5	2–6

5.4 Weak Anti-Localization and Electron-Electron Interaction Effects in the Conductivity of Bismuth Thin Films

It was shown in Sect. 5.3.1 that the temperature dependence of the resistance of the films shows fingerprints of the Coulomb interaction, while the magnetoresistance studies show the presence of weak anti-localization. Both these processes contribute simultaneously to the observed electrical behavior of the films.

It has been noted that theory[162, 163, 175] predicts a $\ln(T)$ dependence in the temperature-dependent conductivity in two-dimensional systems. The weak anti-localization correction is

$$\Delta G_{WAL} = -\frac{\Delta R}{R^2} = \frac{e^2}{4\pi^2\hbar} \ln(\tau_i/\tau_0) = -\frac{e^2 p}{4\pi^2\hbar} \ln(T/\tau_0) \quad , \quad (5.11)$$

and the electron-electron interaction correction is

$$\Delta G_{EEI} = -\frac{e^2 g^*}{2\pi^2\hbar} \ln(4\pi\tau_0 T) \quad . \quad (5.12)$$

In the above equations $\tau_i = T^{-p}$, and $g^* = (1 - 3F/4)$ at zero field and $(1 - F/4)$ at high field, where F has a value between 0 and 1. The value of the conductance quanta appearing in the coefficient in Eqs. 5.11-5.12 is

$$g_0 \equiv \frac{e^2}{2\pi^2\hbar} = 1.235 * 10^{-5} ohm^{-1} \quad . \quad (5.13)$$

Since the conductivity is the natural quantity for describing the electrical properties in this context, the data from Figs. 5-10, 5-12, and 5-13 are depicted again in Figs. 5-23-5-25 in terms of the sheet conductivity of the films.

Figure 5-23 shows that the linear dependence on $\ln(T)$ is only valid for the glass-supported continuous film, and only for a small temperature range ($T < 4$ K). The linear relation with $\ln(T)$, however, is only expected within a temperature range of a fixed power law in the temperature dependence of τ_i . As it was shown in Sect. 5.3.3, this is not the case for at least one of the films. Figure 5-23 suggests there should be a variation in the values of p in the temperature range under examination. The inset in

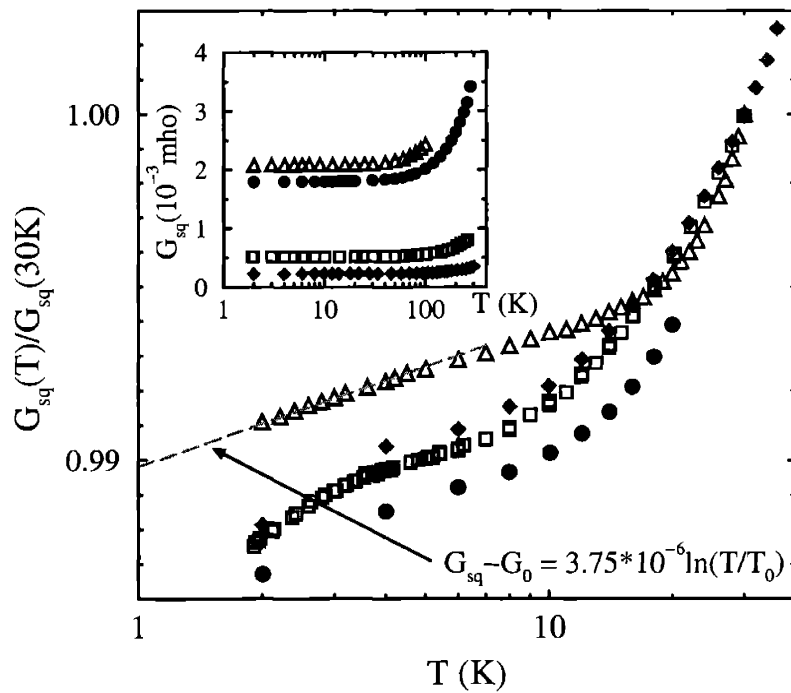


Figure 5-23: Temperature dependence of the sheet conductivity, normalized to the sheet conductivity at 30 K, of 33-nm thick bismuth films on various substrates: (●) patterned silicon, (□) Whatman filter, (◆) PAA on an oxidized wafer, and (△) glass (continuous). Inset: The absolute sheet conductivity of the various films in the temperature range 2-300 K.

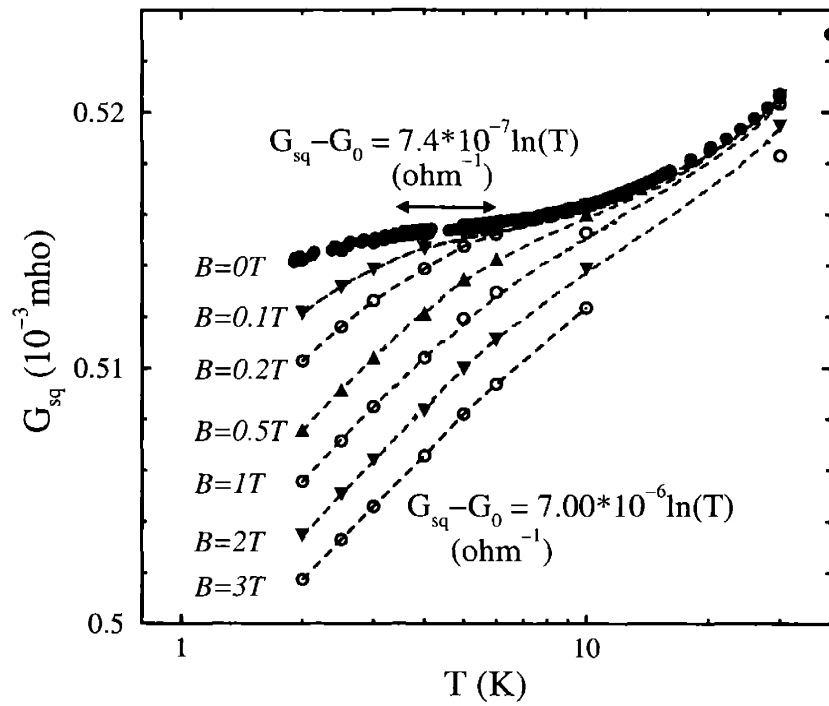


Figure 5-24: Temperature dependence of the sheet conductivity of a 33-nm thick bismuth film on a Whatman filter, at various magnetic field strengths.

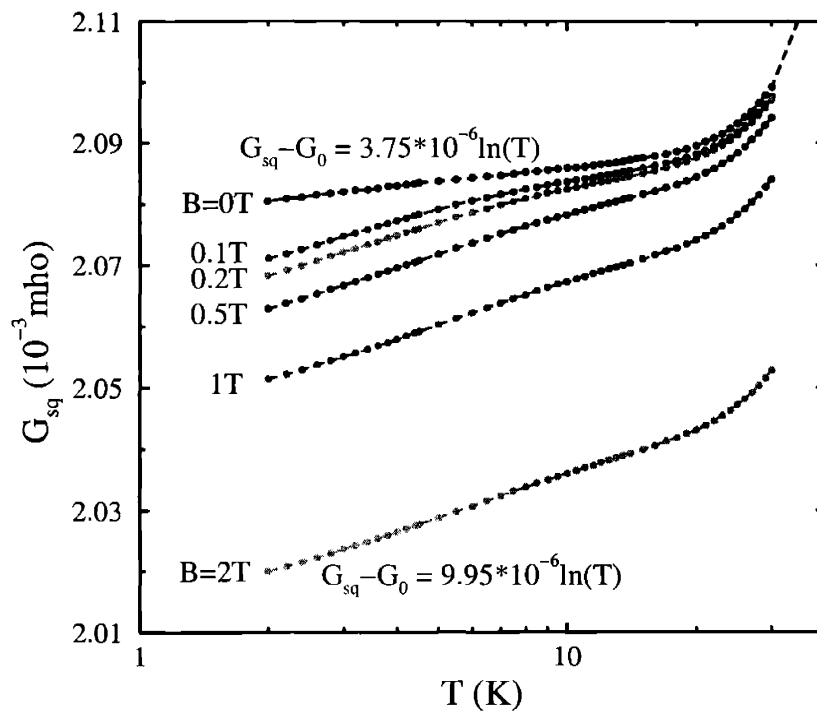


Figure 5-25: Temperature dependence of the sheet conductivity of a 33-nm thick bismuth film on a glass cover slide, at various magnetic field strengths.

Fig. 5-23 also indicates that the conductivities of the films vary largely from substrate to substrate. The implications of this difference will be discussed in Sect. 5.5.

Figure 5-24 shows the sheet conductivity of an antidot array bismuth film on a Whatman substrate. Fitting to the linear portions of the curves provided values of $7.00 \cdot 10^{-6} \Omega^{-1}$ and $7.4 \cdot 10^{-7} \Omega^{-1}$ for the high field and zero field slopes, respectively. Figure 5-25 shows the sheet conductivity of a continuous bismuth film on a glass substrate. Here, the slopes are $9.95 \cdot 10^{-6} \Omega^{-1}$ and $3.75 \cdot 10^{-7} \Omega^{-1}$ for the high field and zero field slopes, respectively. It is immediately noticed that the difference in the slopes is $6.2 \cdot 10^{-6} \Omega^{-1}$ in both cases, or $0.5g_0$. From Eqs. 5.11 and 5.12 it follows that

$$\frac{\partial \Delta G(B \gg H_i) - \Delta G(B = 0)}{\partial \ln(T)} = \frac{e^2}{2\pi^2 \hbar} \left(\frac{p}{2} + \frac{F}{2} \right) = 0.5g_0 \cdot (p + F) \quad . \quad (5.14)$$

By subtracting the slopes, the contributions of field-independent processes, such as thermal carrier excitation, to the conductivity were canceled, and the relation

$$(p + F) = 1$$

obtained by others[163, 167] was recovered.

5.5 Analysis of the Magnetoconductance

So far, there has been no evidence for a significant dependence of the transport mechanisms on film morphology (antidot array *vs.* continuous): The temperature dependence of τ_i , the values of H_0 and H_{so} , and the sum $p + F$ appear to be similar for bismuth films on glass, on alumina, and on silicon. The ratio τ_i/τ_0 is actually more favorable for the continuous film. Yet the effect of the weak anti-localization in the magnetoresistance is distinctively more prominent in the antidot array films. It is necessary, however, to analyze the results in terms of, not the magnetoresistance, but the natural variable: the absolute sheet conductivity. Figure 5-23 has already indicated that large differences in the absolute conductivity of the films exist.

Figure 5-26 shows the magnetic field dependence of the sheet conductivity of the various 33-nm thick bismuth films. The sets of curves in each graph correspond to measurements at various temperatures between 2 K and 30 K showing a monotonic increase in conductivity with increase in temperature. For the sake of comparison, the scale of the y -axis in all the graphs is uniform (full range= $10^{-4} \Omega^{-1}$). Clearly, the classical magnetoresistance effect dominates the behavior of the high conductivity samples on glass, while weak anti-localization dominates the behavior of the more resistive antidot array films. Figure 5-27 zooms in on the low field region of each graph, where classical magnetoresistance effects are weak. The data are plotted with respect to the zero field conductivity, the natural variable by Eq. 5.2, for comparison. This representation shows that the magnitudes of the weak anti-localization effect in the films are comparable with each other. The weakest effect is observed for the film on alumina, for which a low τ_i/τ_0 ratio was calculated. This picture is consistent with the results for H_x obtained from the fittings.

The effect of film morphology on the weak anti-localization effect is suggested to be indirect. The antidot array film morphology is responsible for a decrease in the film *sheet conductivity*, through the decrease of the film volume, and effectively its cross-section. The antidot array morphology also introduces a moderate increase in scattering rates due to grain boundaries (particularly with the alumina substrate). This is advantageous for reducing the magnitude of the classical magnetoresistance, and thus emphasizing the weak anti-localization effects, which in the case of bismuth, are weaker in magnitude. As a result, the contributions from weak anti-localization effects to the conductivity can be observed and analyzed over a wider range of magnetic field strengths (and temperatures). Furthermore, in the natural variable for measurements and applications, the magnetoresistance (MR), the change in resistance is magnified compared to the change in conductance proportionally to the sheet resistance:

$$MR \equiv \Delta R/R = \Delta G \cdot R \quad . \quad (5.15)$$

The antidot array, thus, augments the weak anti-localization effects for detection

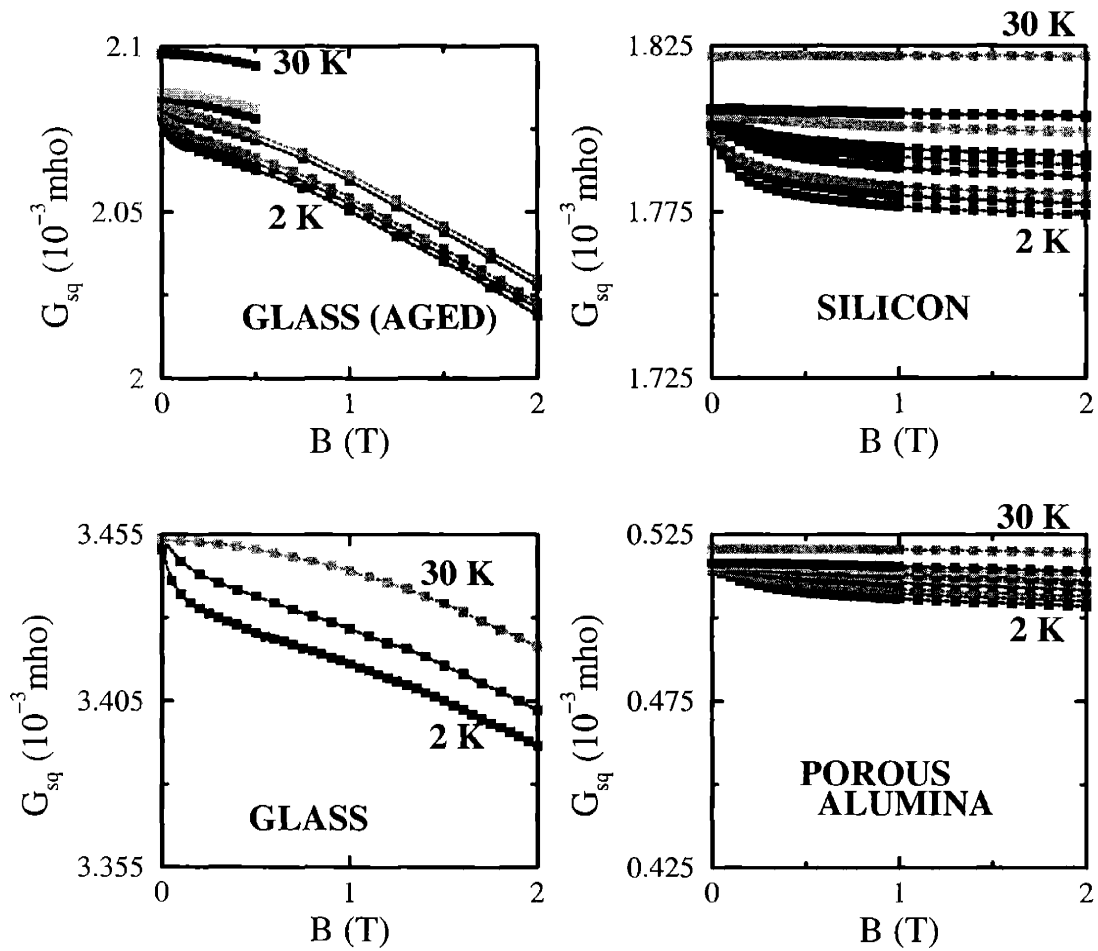


Figure 5-26: Field dependence of the sheet conductivity of 33-nm thick bismuth films on various substrates, at various operating temperatures between 2–30 K.

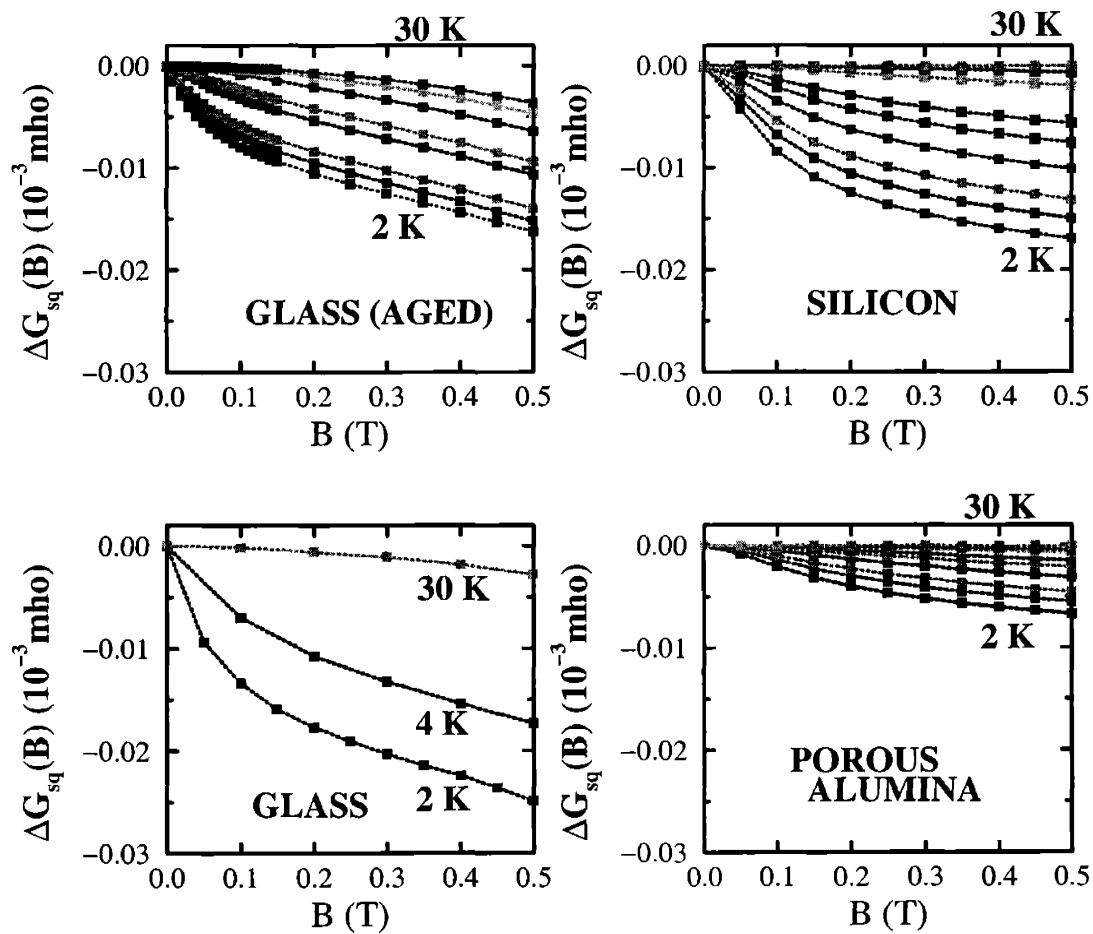


Figure 5-27: Sheet conductivity changes (with respect to the zero-field conductivity) as a function of magnetic field of 33-nm thick bismuth films on various substrates, at various operating temperatures between 2–30 K, zooming in the low field region, where the conductivity is dominated by weak anti-localization effects.

through the magnetoresistance, but does not alter it. Thus, the original properties of the continuous metallic film can be studied with more ease through the nanostructured film. With a reduced contribution of the classical magnetoresistance, the fits to Eq. 5.2 are more accurate, and the determination of the scattering rates is improved. This was best demonstrated in the case of the film on the silicon substrate: The weak anti-localization effects are as strong as in the continuous films, but the classical magnetoresistance contribution is weaker. Thus, the change in the temperature dependence of H_i near 3 K could be clearly resolved. In the other films, this complex temperature dependence seems to have been blurred by the errors introduced by the fitting procedure (due to a large classical magnetoresistance in the glass substrate film, and a small weak anti-localization effect contribution in the alumina substrate film).

5.6 Summary

The magnetoresistance properties of thin bismuth films, lacking or possessing nanoscale porosity, were analyzed. Both classical and interference effects (weak anti-localization) were observed. The films with antidot array morphologies had higher sheet resistances, but similar weak anti-localization characteristics, compared to continuous films. The change in resistance in the magnetic field $\Delta R(B)$ from the classical magnetoresistance is proportional to R , and from the weak anti-localization is proportional to R^2 . As a result, in the antidot array films, the weak anti-localization effect appears more pronounced. The nanoscale porosity thus can be used to facilitate the determination of scattering rates in system with high mobilities, such as bismuth and 2-DEG in semiconductor inversion layers.

From the scattering rates that were calculated from this work, it is suggested that the width of the constrictions between the pores need to be comparable in size to the film thickness in order to substantially affect the scattering rates. The film thickness needs to be reduced in order to investigate a wider temperature range and verify the cross-over in the inelastic scattering mechanism. A transition between one-

dimensional and two-dimensional weak localization should be expected as well. To achieve that, special care will be necessary to prevent the oxidation of the film.

Bibliography

- [1] *Springer Handbook of Nanotechnology*, edited by B. Bhushan, Springer-Verlag, Heidelberg, Germany, 2004.
- [2] H. J. Goldsmid, in *Applications of Thermoelectricity*, chapter 1, Methuen & Co. Ltd., London, 1960.
- [3] H. J. Goldsmid, in *Applications of Thermoelectricity*, chapter 2, Methuen & Co. Ltd., London, 1960.
- [4] H. J. Goldsmid, in *CRC Handbook of Thermoelectrics*, edited by D. M. Rowe, pp. 19–25, CRC Press, Boca Raton, 1995.
- [5] *CRC Handbook of Thermoelectrics*, edited by D. M. Rowe, CRC Press, Boca Raton, 1995.
- [6] L. D. Hicks, T. C. Harman, and M. S. Dresselhaus, *Appl. Phys. Lett.* **63**, 3230–3232 (1993).
- [7] R. Venkatasubramanian, E. Siivola, T. Colpitts, and B. O’Quinn, *Nature (London)* **413**, 597–602 (2001).
- [8] T. C. Harman, P. J. Taylor, M. P. Walsh, and B. E. LaForge, *Science* **297**, 2229–2232 (2002).
- [9] K. F. Hsu, S. Loo, F. Guo, W. Chen, J. S. Dyck, C. Uher, T. Hogan, E. K. Polychroniadis, , and M. G. Kanatzidis, *Science* **303**, 818–821 (2004).

- [10] L. D. Hicks. *The effect of quantum-well superlattices on the thermo-electric figure of merit*. Ph.D. thesis, Massachusetts Institute of Technology, Department of Physics, June 1996.
- [11] Z. B. Zhang. *Fabrication, characterization and transport properties of bismuth nanowire systems*. Ph. D. thesis, Massachusetts Institute of Technology, Department of Physics, February 1999.
- [12] X. Sun. *The effect of quantum confinement on the thermoelectric figure of merit*. Ph.D. thesis, Massachusetts Institute of Technology, Department of Physics, June 1999.
- [13] Y.-M. Lin. *Fabrication, Characterization, and Theoretical Modeling of the Te-doped Bi nanowire system for thermoelectric applications*. Master's thesis, Massachusetts Institute of Technology, Department of Electrical Engineering and Computer Science, June 2000.
- [14] Y.-M. Lin. *Thermoelectric Properties of $Bi_{1-x}Sb_x$ and Superlattice Nanowires*. Ph.D. thesis, Massachusetts Institute of Technology, Department of Electrical Engineering and Computer Science, June 2003.
- [15] J. Heremans, C. M. Thrush, Y.-M. Lin, S. Cronin, Z. Zhang, M. S. Dresselhaus, and J. F. Mansfield, *Phys. Rev. B* **61**, 2921–2930 (2000).
- [16] Y.-M. Lin, X. Sun, and M. S. Dresselhaus, *Phys. Rev. B* **62**, 4610–4623 (2000).
- [17] A. F. Ioffe, *Semiconductor Thermoelements and Thermoelectrics Cooling*, Infosearch Ltd., London, 1957.
- [18] T. Tritt, *Science* **283**, 804–805 (1999).
- [19] N. W. Ashcroft and N. D. Mermin, *Solid State Physics*, appendix E, Holt, Rinehart and Winston, New York, 1976.
- [20] C. M. Bhandari and D. M. Rowe, in *CRC Handbook of Thermoelectrics*, edited by D. M. Rowe, pp. 43–53, CRC Press, Boca Raton, 1995.

- [21] C. Kittel, *Introduction to solid state physics*, 5th ed., chapter 6, John Wiley & Sons Inc., New York, 1976.
- [22] D. Schiferl and C. S. Barrett, *J. Appl. Crystallogr.* **2**, 30 (1969).
- [23] W. B. Pearson, *The crystal chemistry and physics of metals and alloys*, Wiley-Interscience, New York, 1972.
- [24] R. W. G. Wyckoff, *Crystal Structures*, vol. 1, Interscience, New York, 1964.
- [25] *PDF-2 Powder Diffraction File*. JCPDS - The International Center for Diffraction Data, Newton Square, PA.
- [26] *Landolt-Börnstein Numerical Data and Functional Relationships in Science and Technology*, edited by K.-H. Hellwege, O. Madelung and M. Schultz, New Series, Springer-Verlag, Berlin, 1987.
- [27] A. L. Jain, *Phys. Rev.* **114**, 1518–1528 (1959).
- [28] M. S. Dresselhaus, in *Proceedings of the Conference on the Physics of Semimetals and Narrow Gap Semiconductors*, edited by D. L. Carter and R. T. Bate, pp. 3–33, Pergamon Press, New York, NY, 1970.
- [29] E. J. Tichovolsky and J. G. Mavroides, *Solid State Comm.* **7**, 927–931 (1969).
- [30] B. Lenoir, M. Cassart, J. P. Michenaud, H. Scherrer, and S. Scherrer, *J. Phys. Chem. Solids* **57**, 89–99 (1996).
- [31] J. J. Hall and S. H. Koenig, *IBM J. Res. Develop.* **8**, 241–246 (1964).
- [32] R. D. Brown, R. L. Hartman, and S. H. Koenig, *Phys. Rev.* **172**, 598–602 (1968).
- [33] L. M. Falicov and P. J. Lin, *Phys. Rev.* **141**, 562–567 (1966).
- [34] H. J. Goldsmid, *Phys. Stat. Sol. A* **1**, 7–28 (1970).
- [35] S. Golin, *Phys. Rev.* **176**, 830–832 (1968).

- [36] T. Yazaki and Y. Abe, *J. Phys. Soc. Jpn.* **24**, 290–295 (1968).
- [37] R. Kuhl, W. Kraak, H. Haefner, and R. Herrmann, *Phys. Stat. Sol. B* **77**, 109–111 (1976).
- [38] M. P. Vecchi, E. Mendez, and M. S. Dresselhaus, in *Proceedings of the 13th International Conference on the Physics of Semiconductors*, edited by F. G. Fumi, p. 459, 1976. Rome, Italy.
- [39] W. M. Yim and A. Amith, *Solid State Electronics* **15**, 1141–1165 (1972).
- [40] N. B. Brandt, Y. G. Ponomarev, and S. M. Chudinov, *J. Low Temp. Phys.* **8**, 369–419 (1972).
- [41] B. Lenoir, A. Dauscher, M. Cassart, Yu. I. Ravich, and H. Scherrer, *J. Phys. Chem. Solids* **59**, 129–134 (1998).
- [42] L. D. Hicks and M. S. Dresselhaus, *Phys. Rev. B* **47**, 16631–16634 (1993).
- [43] X. Sun, Y.-M. Lin, S. B. Cronin, M. S. Dresselhaus, J. Y. Ying, and G. Chen, in *The 18th International Conference on Thermoelectrics: ICT Symposium Proceedings, Baltimore*, edited by G. Chen, pp. 394–397, IEEE Inc., Piscataway, NJ, 1999.
- [44] C. F. Gallo, B. S. Chandrasekhar, and P. H. Sutter, *J. Appl. Phys.* **34**, 144–152 (1963).
- [45] M. P. Vecchi and M. S. Dresselhaus, *Phys. Rev. B* **10**, 771–774 (1974).
- [46] B. Lenoir, A. Dauscher, X. Devaux, R. Martin-Lopez, Yu. I. Ravich, H. Scherrer, and S. Scherrer, in *Proceedings of the 15th International Conference on Thermoelectrics*, edited by T. Caillat, A. Borshchevsky, and J.-P. Fleurial, pp. 1–13, IEEE Inc., Piscataway, NJ, 1996.
- [47] R. J. Dinger and A. W. Lawson, *Phys. Rev. B* **7**, 5215–5227 (1973).
- [48] R. T. Isaacson and G. A. Williams, *Phys. Rev.* **185**, 682–688 (1969).

- [49] W. R. Datars and J. Vanderkooy, IBM J. Res. Develop. **8**, 247–252 (1964).
- [50] G. E. Smith, Phys. Rev. Lett. **9**, 487–489 (1962).
- [51] G. Oelgart and R. Hermann, Phys. Stat. Sol. B **58**, 181–187 (1973).
- [52] G. Oelgart and R. Hermann, Phys. Stat. Sol. B **61**, 137–146 (1974).
- [53] B. Lax, Bull. Am. Phys. Soc. **5**, 167 (1960).
- [54] K. Miki, J. H. G. Owen, D. R. Bowler, G. A. D. Briggs, and K. Sakamoto, Surface Science **421**, 397–418 (1999).
- [55] C. A. Hoffman, J. R. Meyer, F. J. Bartoli, A. Di Venere, X. J. Yi, C. L. Hou, H. C. Wang, J. B. Ketterson, and G. K. Wong, Phys. Rev. B **48**, 11431–11434 (1993).
- [56] O. Rabin, Y.-M. Lin, and M. S. Dresselhaus, Appl. Phys. Lett. **79**, 81–83 (2001).
- [57] Marcie R. Black. *The Optical Properties of Bi Nanowires*. Ph. D. thesis, Massachusetts Institute of Technology, Department of Electrical Engineering and Computer Science, June 2003.
- [58] S. Golin, Phys. Rev. **166**, 643–651 (1968).
- [59] J. Rose and R. Schuchardt, Phys. Stat. Sol. B **139**, 499–518 (1987).
- [60] Y. Liu and R. E. Allen, Phys. Rev. B **52**, 1566–1577 (1995).
- [61] N. W. Ashcroft and N. D. Mermin, *Solid State Physics*, chapters 12-13, Holt, Rinehart and Winston, New York, 1976.
- [62] A. Demouge, B. Lenoir, Yu. Ravich, H. Scherrer, and S. Scherrer, J. Phys. Chem. Solids **56**, 1155–1164 (1995).
- [63] V. D. Kagan and N. A. Red’ko, in *Fourteenth International Conference on Thermoelectrics: Proceedings, ICT’95; St. Petersburg, Russia*, pp. 78–81, IEEE Inc., Piscataway, NJ, 1995.

- [64] Z. Zhang, D. Gekhtman, M. S. Dresselhaus, and J. Y. Ying, *Chem. Mater.* **11**, 1659–1665 (1999).
- [65] Y.-M. Lin, S. B. Cronin, O. Rabin, J. Y. Ying, and M. S. Dresselhaus, *Appl. Phys. Lett.* **79**, 677–679 (2001).
- [66] Y.-M. Lin, O. Rabin, S. B. Cronin, J. Y. Ying, and M. S. Dresselhaus, *Appl. Phys. Lett.* **81**, 2403–2405 (2002).
- [67] *The anodic behavior of metal and semiconductors series*, edited by J. W. Diggle and A. K. Vijh, vols. 1–5, Marcel Dekker, Inc., New York, 1972.
- [68] L. Young, *Anodic oxide films*, Academic Press, London, 1961.
- [69] M. M. Lohrengel, *Mater. Sci. Eng. R: Reports* **11**, 243–294 (1993).
- [70] J. W. Diggle, T. C. Downie, and C. W. Goulding, *Chem. Rev.* **69**, 365–405 (1969).
- [71] J. P. O’Sullivan and G. C. Wood, *Proc. Roy. Soc. Lond. A.* **317**, 511–543 (1970).
- [72] G. H. Kissin, in *Anodized Aluminum*, pp. 34–61, Am. Soc. Testing Mats., 1965.
- [73] K. Shimizu, K. Kobayashi, G. E. Thompson, and G. C. Wood, *Phil. Mag. A* **66**, 643–652 (1992).
- [74] F. Li, L. Zhang, and R.M. Metzger, *Chem. Mater.* **10**, 2470–2480 (1998).
- [75] A. P. Li, F. Müller, A. Birner, K. Nielsch, and U. Gösele, *J. Appl. Phys.* **84**, 6023–6026 (1998).
- [76] H. Masuda, K. Yada, and A. Osaka, *Jpn. J. Appl. Phys.* **37**, L1340–L1342 (1998).
- [77] C. Y. Liu, A. Datta, and Y. L. Wang, *Appl. Phys. Lett.* **78**, 120–122 (2001).
- [78] A. P. Li, F. Müller, and U. Gösele, *Electrochem. and Solid-State Lett.* **3**, 131–134 (2000).

- [79] H. Masuda, H. Yamada, M. Satoh, H. Asoh, M. Nakao, and T. Tamamura, *Appl. Phys. Lett.* **71**(19), 2770–2772 (1997).
- [80] V. Lehmann and U. Grüning, *Thin Solid Films* **297**, 13–17 (1997).
- [81] H. Föll, S. Langa, J. Carstensen, M. Christophersen, and I. M. Tiginyanu, *Adv. Mater.* **15**, 183–198 (2003).
- [82] H. Masuda and M. Satoh, *Jpn. J. Appl. Phys.* **35**, L126–L129 (1996).
- [83] Anodisc Membranes, Whatman Inc., Product Catalog, 2003.
- [84] D. Crouse, Y.-H. Lo, A. E. Miller, and M. Crouse, *Appl. Phys. Lett.* **76**, 49–51 (2000).
- [85] Y. Li, R. Holland, and P. R. Wilshaw, *J. Vac. Sci. Technol. B* **18**, 994–996 (2000).
- [86] J.-H. Wu, L. Pu, J.-P. Zou, Y.-F. Mei, J.-M. Zhu, and X.-M. Bao, *Chin. Phys. Lett.* **17**, 451–453 (2000).
- [87] J. Choi, G. Sauer, P. Göring, K. Nielsch, R. B. Wehrspohn, and U. Gösele, *J. Mater. Chem.* **13**, 1100–1103 (2003).
- [88] M. S. Sander and L.-S. Tan, *Adv. Funct. Mater.* **13**, 393–397 (2003).
- [89] S. Shingubara, O. Okino, Y. Sayama, H. Sakaue, and T. Takahagi, *Solid State Elect.* **43**, 1143–1146 (1999).
- [90] H. Masuda, K. Yasui, Y. Sakamoto, M. Nakao, T. Tamamura, and K. Nishio, *Jpn. J. Appl. Phys.* **40**, L1267–L1269 (2001).
- [91] A. Cai, H. Zhang, H. Hua, and Z. Zhang, *Nanotechnology* **13**, 627–630 (2002).
- [92] W. C. Hu, D. W. Gong, Z. Chen, L. M. Yuan, K. Saito, C. A. Grimes, and P. Kichambare, *Appl. Phys. Lett.* **79**, 3083–3085 (2001).
- [93] T. Iwasaki, T. Motoi, and T. Den, *Appl. Phys. Lett.* **75**, 2044–2046 (1999).

- [94] S.-H. Jeong, H.-Y. Hwang, K.-H. Lee, and Y. Jeong, *Appl. Phys. Lett.* **78**, 2052–2054 (2001).
- [95] V. V. Konovalov, G. Zangari, and R. M. Metzger, *Chem. Mater.* **11**, 1949–1951 (1999).
- [96] M. T. Wu, I. C. Leu, and M. H. Hon, *J. Vac. Sci. Technol. B* **20**, 776–782 (2002).
- [97] O. Jessensky, F. Müller, and U. Gösele, *Appl. Phys. Lett.* **72**, 1173–1175 (1998).
- [98] H. Masuda, M. Watanabe, K. Yasui, D. Tryk, T. Rao, and A. Fujishima, *Adv. Mater.* **12**, 444–447 (2000).
- [99] H. Masuda, K. Yasui, and K. Nishio, *Adv. Mater.* **12**, 1031–1033 (2000).
- [100] D. Almawlawi, K. A. Bosnick, A. Osika, and M. Moskovits, *Adv. Mater.* **12**, 1252–1257 (2000).
- [101] J. Liang, H. Chik, A. Yin, and J. Xu, *J. Appl. Phys.* **91**, 2544–2546 (2002).
- [102] X. Mei, D. Kim, H. E. Ruda, and Q. X. Guo, *Appl. Phys. Lett.* **81**, 361–363 (2002).
- [103] X. Mei, M. Blumin, M. Sun, D. Kim, Z. H. Wu, H. E. Ruda, and Q. X. Guo, *Appl. Phys. Lett.* **82**, 967–969 (2003).
- [104] Y. Kanamori, K. Hane, H. Sai, and H. Yugami, *Appl. Phys. Lett.* **78**, 142–143 (2001).
- [105] Z. L. Xiao, C. Y. Han, U. Welp, H. H. Wang, V. K. Vlasko-Vlasov, W. K. Kwok, D. J. Miller, J. M. Hiller, R. E. Cook, G. A. Willing, and G. W. Crabtree, *Appl. Phys. Lett.* **81**, 2869–2871 (2002).
- [106] S. Z. Chu, K. Wada, S. Inoue, and S. Todoroki, *J. Electrochem. Soc.* **149**, B321–B327 (2002).

- [107] S. Z. Chu, K. Wada, S. Inoue, S. Todoroki, Y. K. Takahashi, and K. Hono, *Chem. Mater.* **14**, 4595–4602 (2002).
- [108] P. G. Miney, P. E. Colavita, M. V. Schiza, R. J. Priore, F. G. Haibach, and M. L. Myrick, *Electrochem. Solid State Lett.* **6**, B42–B45 (2003).
- [109] N. I. Tatarenko and A. M. Mozalev, *Solid-State Electronics* **45**, 1009–1016 (2001).
- [110] Y. Yang, H. Chen, Y. Mei, J. Chen, X. Wu, and X. Bao, *Solid State Comm.* **123**, 279–282 (2002).
- [111] N. A. Melosh, A. Boukai, F. Diana, B. Gerardot, A. Badolato, P. M. Petroff, and J. R. Heath, *Science* **5616**, 112–115 (2003).
- [112] Y. Huang, X. Duan, Y. Cui, L. J. Lauhon, K.-H. Kim, and C. M. Lieber, *Science* **294**, 1313–1317 (2001).
- [113] M. S. Dresselhaus, Y.-M. Lin, O. Rabin, M. R. Black, and G. Dresselhaus, in *Springer Handbook of Nanotechnology*, chapter 4, pp. 99–145, edited by B. Bhushan, Springer-Verlag, Heidelberg, Germany, 2004.
- [114] P. P. Mardilovich, A. N. Govyadinov, N. I. Mazurenko, and R. Paterson, *J. Membrane Sci.* **98**, 143–155 (1995).
- [115] O. Rabin, P. R. Herz, Y.-M. Lin, A. I. Akinwande, S. B. Cronin, and M. S. Dresselhaus, *Adv. Funct. Mater.* **13**, 631–638 (2003).
- [116] O. Rabin, P. R. Herz, Y.-M. Lin, A. I. Akinwande, and M. S. Dresselhaus. *Thick porous anodic alumina films and nanowire arrays grown on a solid substrate*, U.S. Provisional Patent, Application 60/333,403 (2001).
- [117] M. A. Ryan and J.-P. Fleurial, *Interface* **11**, 30–33 (2002).
- [118] Y.-M. Lin, M. S. Dresselhaus, and J. Y. Ying, in *Advances in Chemical Engineering*, edited by K. Ricci, pp. 167–198, Academic Press, York, PA, 2001.

- [119] K. K. Lew and J. M. Redwing, *J. Crystal Growth* **254**, 14–22 (2003).
- [120] A. P. Li, F. Müller, A. Birner, K. Nielsch, and U. Gösele, *Adv. Mater.* **11**, 483–487 (1999).
- [121] D. Gong, V. Yadavalli, M. Paulose, M. Pishko, and C. A. Grimes, *Biomed. Microdev.* **5**, 75–80 (2003).
- [122] S. R. Nicewarner-Peña, R. G. Freeman, B. D. Reiss, L. He, D. J. Peña, I. D. Walton, R. Cromer, C. D. Keating, and M. J. Natan, *Science* **294**, 137–141 (2001).
- [123] J. Yan, G. V. R. Rao, M. Barela, D. A. Brevnov, Y. Jiang, H. Xu, G. P. López, and P. B. Atanassov, *Adv. Mater.* **15**, 2015–2018 (2003).
- [124] O. W. Sacks, *Uncle Tungsten: Memories of a Chemical Boyhood*, Alfred A. Knopf, New York, 2001.
- [125] H. Masuda, M. Ohya, H. Asoh, M. Nakao, M. Nohtomi, and T. Tamamura, *Jpn. J. Appl. Phys.* **38**, L1403–L1405 (1999).
- [126] H. Masuda, H. Asoh, M. Watanbe, K. Nishio, M. Nakao, and T. Tamamura, *Adv. Mater.* **13**, 189–192 (2001).
- [127] X. Sun, Z. Zhang, and M. S. Dresselhaus, *Appl. Phys. Lett.* **74**, 4005–4007 (1999).
- [128] T. E. Huber, M. J. Graf, C. A. Foss, Jr., and P. Constant, *J. Mater. Res.* **15**, 1816–1821 (2000).
- [129] K. Liu, C. L. Chien, P. C. Searson, and K. Yu-Zhang, *Appl. Phys. Lett.* **73**, 1436–1438 (1998).
- [130] Y.-M. Lin, S. B. Cronin, J. Y. Ying, M. S. Dresselhaus, and J. P. Heremans, *Appl. Phys. Lett.* **76**, 3944–3946 (2000).

- [131] T. E. Huber, K. Celestine, and M. J. Graf, Phys. Rev. B **67**, 245317(1–11) (2003).
- [132] L. Piraux, S. Dubois, J. L. Duvail, A. Radulescu, S. Demoustier-Champagne, E. Ferain, and R. Legras, J. Mater. Res. **14**, 3042–3050 (1999).
- [133] Y. Gao, H. Niu, C. Zeng, and Q. Chen, Chem. Phys. Lett. **367**, 141–144 (2003).
- [134] M. Martín-González, A. L. Prieto, M. S. Knox, R. Gronsky, T. Sands, and A. M. Stacy, Chem. Mater. **15**, 1676–1681 (2003).
- [135] A. L. Prieto, M. Martín-González, J. Keyani, R. Gronsky, T. Sands, and A. M. Stacy, J. Am. Chem. Soc. **125**, 2388–2389 (2003).
- [136] P. P. Mardilovich, A. N. Govyadinov, N. I. Mukhurov, A. M. Rzhetskii, and R. Paterson, J. Membrane Sci. **98**, 131–142 (1995).
- [137] P. P. Mardilovich, A. N. Govyadinov, N. I. Mukhurov, and R. Paterson, J. Membrane Sci. **98**, 143–155 (1995).
- [138] A. Brenner, *Electrodeposition of alloys. Principles and practice*, vol. II, Academic Press, New York–London, 1963.
- [139] M. Harbaugh and F. C. Mathers, Trans. Electrochem. Soc. **64**, 293–298 (1933).
- [140] L. Languren-Davidson, F. Lu, G. N. Salaita, and A. T. Hubbard, Langmuir **4**, 224–232 (1988).
- [141] F. Besse, C. Boulanger, and J. M. Lecuire, J. Appl. Electrochem. **30**, 385–392 (2000).
- [142] *Binary alloy phase diagrams*, edited by T. B. Massalski, 2nd ed., ASM International, Materials Park, OH, 1990.
- [143] J. Heremans, C. M. Thrush, Y.-M. Lin, S. B. Cronin, and M. S. Dresselhaus, Phys. Rev. B **63**, 085406(1–8) (2001).

- [144] T. E. Huber, O. Onakoya, and M. H. Ervin, *J. Appl. Phys.* **92**, 1337–1343 (2002).
- [145] V. M. Kozlov, V. Agrigento, G. Mussati, and L. P. Bicelli, *J. Alloys Compd.* **288**, 255–261 (1999).
- [146] E. Roy, P. Fricoteaux, and K. Yu-Zhang, *J. Nanosci. Nanotech.* **1**, 323–329 (2001).
- [147] A. J. Yin, J. Li, W. Jian, A. J. Bennett, and J. M. Xu, *Appl. Phys. Lett.* **79**, 1039–1041 (2001).
- [148] A. L. Prieto, M. S. Sander, M. S. Martín-González, R. Gronsky, T. Sands, and A. M. Stacy, *J. Am. Chem. Soc.* **123**, 7160–7161 (2001).
- [149] K. Nielsch, F. Müller, A.-P. Li, and U. Gösele, *Adv. Mater.* **12**, 582–586 (2000).
- [150] T. G. Shibleva, V. V. Povetkin, and M. S. Zakharov, *J. Appl. Chem. USSR* **59**, 626–628 (1986).
- [151] X. F. Wang, L. D. Zhang, J. Zhang, H. Z. Shi, X. S. Peng, M. J. Zheng, J. Fang, J. L. Chen, and B. J. Gao, *J. Phys. D: Appl. Phys.* **34**, 418–421 (2001).
- [152] C. G. Jin, G. W. Jiang, W. F. Liu, W. L. Cai, L. Z. Yao, Z. Yao, and X. G. Li, *J. Mater. Chem.* **13**, 1743 – 1746 (2003).
- [153] L. Li, Y. Zhang, G. Li, and L. Zhang, *Chem. Phys. Lett.* **378**, 244–249 (2003).
- [154] Y. Zhang, G. Li, Y. Wu, B. Zhang, W. Song, and L. Zhang, *Adv. Mater.* **14**, 1227–1230 (2003).
- [155] S. B. Cronin, Y.-M. Lin, O. Rabin, M. R. Black, G. Dresselhaus, M. S. Dresselhaus, and P. L. Gai, *Microscopy and Microanalysis* **8**, 58–63 (2002).
- [156] S. H. Choi, K. L. Wang, M. S. Leung, G. W. Stupian, N. Presser, B. A. Morgan, R. E. Robertson, M. Abraham, E. E. King, , M. B. Tueling, S. W. Chung, J. R.

- Heath, S. L. Cho, and J. B. Ketterson, *J. Vac. Sci. Technol. A* **18**, 1326–1328 (2000).
- [157] Z. Zhang, X. Sun, M. S. Dresselhaus, J. Y. Ying, and J. Heremans, *Phys. Rev. B* **61**, 4850–4861 (2000).
- [158] K. Hong, F. Y. Yang, K. Liu, D. H. Reich, P. C. Searson, and C. L. Chien, *J. Appl. Phys.* **85**, 6184–6186 (1999).
- [159] R. Hartman, *Phys. Rev.* **181**, 1070–1086 (1969).
- [160] Y.-T. Cheng, A. M. Weiner, C. A. Wong, M. P. Balogh, and M. J. Lukitsch, *Appl. Phys. Lett.* **81**, 3248–3250 (2002).
- [161] J.-E. Wegrowe, S. E. Gilbert, D. Kelly, B. Doudin, and J.-Ph. Ansermet, *IEEE Trans. Magn.* **34**, 903–905 (1998).
- [162] G. Bergmann, *Phys. Rep.* **107**, 1–58 (1984).
- [163] D. E. Beutler and N. Giordano, *Phys. Rev. B* **38**, 8–19 (1988).
- [164] M. Farhoud, M. Hwang, H. I. Smith, M. L. Schattenburg, J. M. Bae, K. Youcef-Toumi, and C. A. Ross, *IEEE Trans. Magn.* **34**, 1087–1089 (1998).
- [165] M. Farhoud, J. Ferrera, A. J. Lochtefeld, T. E. Murphy, M. L. Schattenburg, J. Carter, C. A. Ross, and H. I. Smith, *J. Vac. Sci. Tech. B* **17**, 3182–3185 (1999).
- [166] T. Kawaguti and Y. Fujimori, *J. Phys. Soc. Jpn.* **51**, 703–704 (1982).
- [167] F. Komori, S.-I. Kobayashi, and W. Sasaki, *J. Phys. Soc. Jpn.* **52**, 368–371 (1983).
- [168] T. Kawaguti and Y. Fujimori, *J. Phys. Soc. Jpn.* **52**, 722–725 (1983).
- [169] H. White and D. S. McLachlan, *J. Phys. Condens. Matter* **1**, 6665–6677 (1989).

- [170] J. Heremans, C. M. Thrush, Z. Zhang, X. Sun, M. S. Dresselhaus, J. Y. Ying, and D. T. Morelli, *Phys. Rev. B Rapid* **58**, R10091–R10095 (1998).
- [171] P. H. Woerlee, G. C. Verkade, and A. G. M. Jansen, *J. Phys. C: Solid State Phys.* **16**, 3011–3024 (1983).
- [172] N. W. Ashcroft and N. D. Mermin, *Solid State Physics*, chapter 17, Holt, Rinehart and Winston, New York, 1976.
- [173] A. Schmid, *Z. Phys.* **271**, 251–256 (1974).
- [174] N. W. Ashcroft and N. D. Mermin, *Solid State Physics*, chapter 26, Holt, Rinehart and Winston, New York, 1976.
- [175] H. Fukuyama, *J. Phys. Soc. Jpn.* **51**, 1105–1110 (1982).
- [176] Y. Yafet, in *Solid State Physics: Advances in Research and Applications*, edited by F. Seitz and D. Turnbull, pp. 1–98, Academic Press, New York, 1963.
- [177] R. Meservey and P. M. Tedlow, *Phys. Rev. Lett.* **41**, 805–808 (1978).
- [178] P. Santhanam, S. Wind, and D. E. Prober, *Phys. Rev. B* (1987).

Curriculum vitae

ODED RABIN

Home Address: P.O. Box 10850, Carmiel 21781, Israel

Date of Birth: June 24, 1974

EDUCATION

- 1998 – Present **Massachusetts Institute of Technology** Cambridge, MA
Ph.D. candidate – Department of Chemistry.
Thesis Title: “*Bismuth Nanowire and Antidot Array Studies Motivated by Thermoelectricity*”.
- 1996 – 1998 **Weizmann Institute of Science** Rehovot, ISRAEL
M.Sc. degree – Department of Chemistry.
Thesis Title: “*Metal-Mediated Preparation, Stabilization and Controlled Release of Simple Para-Quinone Methides*”.
- 1993 – 1996 **The Technion - Israeli Institute of Technology** Haifa, ISRAEL
B.A. degree – Department of Chemistry.
Selected for the “Excellence Program”. Graduated **Summa cum Laude**.

RESEARCH

- 1999 – Present **Massachusetts Institute of Technology** Cambridge, MA
Research Assistant – Solid State Physics. Supervisor: Prof. Mildred S. Dresselhaus, Dept. of Physics and Dept. of Electrical Engineering and Computer Science.
Investigated the electrochemical template synthesis of nanowires. Developed a general process for the fabrication of arrays of nanowires on silicon wafers, for nanowire-based optical, electrical and sensing devices (patent application submitted). Modeled the thermoelectric properties of bismuth-antimony nanowires. Prepared bismuth thin-film ‘antidot’ arrays, discovered and modeled localization effects.
- 1997 – 1998 **Weizmann Institute of Science** Rehovot, ISRAEL
Research Assistant – Organic Chemistry. Supervisor: Prof. David Milstein, Department of Organic Chemistry.
Synthesized and characterized stable complexes of bio-relevant highly-reactive para-quinone methides and developed ways for their controlled release in solutions.
- 1996 **The Technion - Israel Institute of Technology** Haifa, ISRAEL
Undergraduate Research – Computational Chemistry. Supervisor: Prof. Ytzhak Apeloig, Department of Chemistry.
Carried out Ab-Initio calculations to determine the thermodynamic parameters of nucleophilic addition reactions of substituted silenes. Formulated general rules for the stabilization of these reactive compounds.
- 1995 **University of Twente** Enschede, NETHERLANDS
Summer Intern – Solid State NMR. Supervisor: Dr. John P. V. Van Duinhoven.
Investigated the structure and dynamics of cross-linked polymer chains by solid-state nuclear magnetic resonance techniques.

- AWARDS** ♦ “Excellence Program” Fellowship during undergraduate studies.
/ HONORS Head: Prof. Nimrod Moiseyev. <http://www.technion.ac.il/excellence>
- ♦ “Zeevi Fund” Fellowship for research in chemistry.
 - ♦ President’s Honors, the Technion (1994, 1995, 1996).
 - ♦ Highest GPA – Class of ’96, the Technion.
 - ♦ Best Poster Award, Thermoelectrics Symposium, Materials Research Society Conference, Boston, 2001.
 - ♦ Electrochemical Society Membership Award, 2003.
 - ♦ Cambridge Science Foundation Travel Grant, 2003.
 - ♦ Best Student Poster Award, Electrochemical Society Meeting, Orlando, 2003.

SELECTED PUBLICATIONS

JOURNAL PAPERS AND CONFERENCE PROCEEDINGS:

1. Metal-Mediated Preparation, Stabilization and Controlled Release of a Biologically Relevant Simple Para-Quinone Methide: BHT-QM. O. Rabin, A. Vigalok, D. Milstein, *J. Am. Chem. Soc.*, **120**, 7119-7120, (1998).
2. A Novel Approach Towards Intermolecular Stabilization of Para-Quinone Methides. First Complexation of the Elusive, Simplest Quinone Methide, 4-methylene-2,5-cyclohexadien-1-one. O. Rabin, A. Vigalok, D. Milstein, *Chem.-Eur. J.*, **6**, 454-462, (2000).
3. Thermoelectric Figure of Merit of Bi/Pb_{1-x}Eu_xTe Superlattices. T. Koga, O. Rabin, M.S. Dresselhaus, *Phys. Rev. B* **62**, 16703-16706, (2000).
4. Intersubband Transitions in Bismuth Nanowires. M. R. Black, M. Padi, S. Cronin, Y. Lin, O. Rabin, T. McClure, G. Dresselhaus, P. L. Hagelstein, M. S. Dresselhaus, *Appl. Phys. Lett.*, **77**, 4142-4144, (2000).
5. Quantum Wells and Quantum Wires for Potential Thermoelectric Applications. M.S. Dresselhaus et al., *Semiconductors and Semimetals: Recent Trends in Thermoelectric Materials Research III, "Low dimensional thermoelectricity"*, editor: T. M. Tritt, Academic Press, vol. **71**, pp. 1-121, 2001.
6. Anomalous High Thermoelectric Figure of Merit in Bi_{1-x}Sb_x Nanowires by Carrier Pocket Alignment. O. Rabin, Y.M. Lin, M.S. Dresselhaus, *Appl. Phys. Lett.*, **79**, 81-83, (2001).
7. Transport Properties of Bi_{1-x}Sb_x Alloy Nanowires Synthesized by Pressure Injection. Y.M. Lin, S.B. Cronin, O. Rabin, M.S. Dresselhaus, *Appl. Phys. Lett.*, **79**, 677-679, (2001).
8. Thermoelectric Nanowires by Electrochemical Deposition. O. Rabin, Y.M. Lin, S.B. Cronin, M.S. Dresselhaus, in *Thermoelectric Materials 2001 - Research and Applications: MRS Symp. Proc., Boston*, vol. **691**, G8.20, edited by G.S. Nolas et al., MRS Press, Pittsburgh, PA, 2002.
9. Addition of Nucleophiles to Silenes. A Theoretical Study of the Effect of Substituents on Their Kinetic Stability. M. Bendikov, S.R. Quadt, O. Rabin, Y. Apeloig, *Organometallics*, **21**, 3930-3939 (2002).
10. Making Electrical Contacts to Nanowires with a Thick Oxide Coating. S.B. Cronin, Y.-M. Lin, O. Rabin, M.R. Black, J.Y. Ying, M.S. Dresselhaus, P.L. Gai, J.-P. Minet, J.-P. Issi, *Nanotechnology*, **13**, 1-6 (2002).
11. Formation of Thick Porous Anodic Alumina Films and Nanowire Arrays on Silicon Wafers and Glass. O. Rabin, P. R. Herz, Y.-M. Lin, S.B. Cronin, A. I. Akinwande, M. S. Dresselhaus, *Adv. Funct. Mater.*, **13**, 631-638 (2003).
12. Nanowires. M.S. Dresselhaus, Y.-M. Lin, O. Rabin, M.R. Black, G. Dresselhaus, in *Springer Handbook of Nanotechnology*, editor: Bharat Bhushan, Springer-Verlag, Heidelberg, Germany, 2004.
13. Anomalous Magnetoresistance Behavior of Bismuth Antidot Arrays. O. Rabin, M. S. Dresselhaus, in *Continuous Nanophase and Nanostructured Materials, MRS Symp. Proc., Boston*, vol. **788**, L12.1, edited by S. Komarneni, J.C. Parker, J. Watkins, MRS Press, Pittsburgh, PA, 2004 (in press).

PATENT APPLICATIONS:

1. Thick Porous Anodic Alumina Films and Nanowire Arrays Grown on a Solid Substrate. O. Rabin, P.R. Herz, S.B. Cronin, Y.M. Lin, A.I. Akinwande, M.S. Dresselhaus, *U.S. Provisional Patent Application* 60/333,403 (2001).

INVITED TALKS:

1. Nanotechnology for Engineers: Nanowire Synthesis. IEEE Boston Section Workshop (Bedford, MA), 2003.